APPLIED COMPUTATIONAL ELECTROMAGNETICS SOCIETY JOURNAL

Special Issue on Metamaterials and Metadevices for Integrated Sensing, Imaging, and Communication

Guest Editors:

Yongjin Zhou, Shanghai University, China
Qingfeng Zhang, Southern University of Science and Technology, China
Kai-Da Xu, Xi'an Jiaotong University, China
Xuanru Zhang, Southeast University, China
Lei Zhao, China University of Mining and Technology, China

August 2024
Vol. 39 No. 8
ISSN 1054-4887

The ACES Journal is abstracted in INSPEC, in Engineering Index, DTIC, Science Citation Index Expanded, the Research Alert, and to Current Contents/Engineering, Computing & Technology.

The illustrations on the front cover have been obtained from the ARC research group at the Department of Electrical Engineering, Colorado School of Mines

Published, sold and distributed by: River Publishers, Alsbjergvej 10, 9260 Gistrup, Denmark

AUGUST 2024 REVIEWERS

Nunzia Fontana
Srividhya G.
Nada Habeeb
Yaqdhan Mahmood Hussain
Matteo Bruno Lodi
Vinoth M.
Wenyan Nie
Masoud Sarabi
Giovanni Maria Sardi
Sayidmarie
Anagha Soman
Somchat Sonasang
Kai-Da Xu
Tao Yuan
Xiaoyan Zhang
Xuanru Zhang
Lei Zhao
Yong Zhou

THE APPLIED COMPUTATIONAL ELECTROMAGNETICS SOCIETY JOURNAL

Vol. 39 No. 8 August 2024

TABLE OF CONTENTS

Special Issue Preface

Metamaterials and Metadevices for Integrated Sensing, Imaging, and Communication

Guest Editors

Prof. Yongjin Zhou, Shanghai University, China

Prof. Qingfeng Zhang, Southern University of Science and Technology, China

Prof. Kai-Da Xu, Xi'an Jiaotong University, China

Prof. Xuanru Zhang, Southeast University, China

Prof. Lei Zhao, China University of Mining and Technology, China

Welcome to the special issue of the Journal of the Applied Computational Electromagnetics Society (ACES). The papers included here are related to metamaterials and metadevices for integrated sensing, imaging, and communication for 5G/6G applications.

This special issue discusses the methods and principles to integrate these functions in one system.

A Miniaturized Pattern-reconfigurable Antenna for Broadband VHF and UHF Communications

Haifan Li[1], Tingshuang Zheng[1], Yong Mao[2], and Yongjin Zhou[1,3]

[1]Shanghai Collaborative Innovation Center of Intelligent Sensing Chip Technology
Key Laboratory of Specialty Fiber Optics and Optical Access Networks, Shanghai University,
Shanghai, 200444, China
leonlhf@shu.edu.cn, zts2023hf@163.com

[2]Wuhan Marine Communication Institute
Wuhan 430205, China
19989629966m@sina.cn

[3]Shaanxi Key Laboratory of Artificially-Structured Functional Materials and Devices
Air Force Engineering University, Xi'an 710051, China
yjzhou@shu.edu.cn

Abstract – In this paper, a miniaturized and broadband patter-reconfigurable antenna working at very high frequency (VHF) and ultra-high frequency (UHF) band is proposed. A dipole antenna element with a compact size, stable horizontal gain, a wide bandwidth, and an omnidirectional pattern is introduced firstly, which operates from 116 MHz to 505 MHz with a relative bandwidth of 108.55% and a size of $0.11\lambda_L \times 0.33\lambda_L$. An antenna array is constructed by combining four elements in a rotationally symmetrical manner. When one element is excited and other ports are terminated by matched loads, switchable directional beams are achieved. A 10:1 scaled model of the proposed antenna is fabricated and tested. Measured results show that the antenna element operates from 1.48 GHz to 4.86 GHz (a relative bandwidth of 106.62%) with a gain above -2 dBi. The proposed antenna array can achieve directional beams with a high front to back ratio (FBR) with gain value of 3-4 dBi within 2-4 GHz.

Index Terms – Broadband antennas, dipole antennas, pattern-reconfigurable antennas, VHF/UHF antennas.

I. INTRODUCTION

In modern tactical secure communication systems, spread spectrum and frequency hopping technology is frequently employed to enhance the anti-interference and confidentiality of aircraft and ship communication [1]. Numerous very high frequency (VHF) and ultra-high frequency (UHF) broadband omnidirectional antenna have been proposed over the decades [2–5]. To increase the bandwidth of VHF/UHF antenna, a biconical structure and thick dipole is utilized in [2], a dual-parasitic sleeve structure is applied to improve the impedance further. This design provides a working band that covers a range from 120 to 550 MHz (128%). A dual-sleeve wideband monopole antenna with loaded plasma cylinders is proposed for shipborne systems in VHF range in [3]. It achieves the VSWR ≤ 2 bandwidth of more than 107%. However, it is worth noticing that the prototypes of these antennas tend to be large in size and challenging to manufacture. Reference [4] designs a super broadband dipole antenna with a passive matching network. By loading lumped elements on the antenna body and using the genetic algorithm optimization, it can operate over 30-1200 MHz with VSWR < 3 and broadside gain $>$ -10 dBi. However, the gain is too low to meet the requirements of practical applications.

On the other hand, pattern reconfigurable antenna and multibeam antennas are highly desired in military applications to enhance the capability of wireless communication systems. These technologies contribute to increase spectral efficiency, extend communication range, and improve security and anti-interference. In [6], a wideband multibeam circular array antenna for VHF/UHF directional networks applications is designed by introducing directional antenna element. The problem is that the finite ground plane causes a titled-up radiation pattern from the azimuth plane. Electrically steerable passive array radiators (ESPAR) are used to achieve a directional and steerable radiation pattern on the antenna horizontal plane [7–9]. Nevertheless, these antenna dimensions are characterized by large and complex dimensions and the controlling circuits loaded on the parasitic elements affect the quality of antenna radiation patterns.

Submitted On: October 31, 2023
Accepted On: October 15, 2024

https://doi.org/10.13052/2024.ACES.J.390801

Active frequency selective surfaces (AFSSs) attract significant attention in pattern reconfigurable antenna design [10–12]. These antennas can manipulate radiation direction and beamwidth by changing the PIN diodes or varactors on the AFSS. However, due to the limitation bandwidth of the FSS units, the pattern reconfigurable antennas based on AFSS could only dynamically switch the beams in one or a few operating bands, typically resulting in a larger volume.

This article presents a miniaturized and broadband pattern-reconfigurable VHF/UHF antenna that features four directional beams with high front to back ratio (FBR) in the horizontal plane. Employing a circular array configuration eliminates the need for placing directors or reflectors around the antenna at a distance of $\lambda/4$. This approach results in a more compact size and broader operating bandwidth. A 10:1 scaled model prototype is fabricated and tested to validate our simulation results. This article is organized as follows. In section II, the antenna element design and performance analysis are discussed in detail. In section III, an antenna array with directional beams is studied and the simulated and measured results are shown. Section IV is the conclusion of the entire paper.

II. ANTENNA ELEMENT DESIGN AND PERFORMANCE ANALYSIS

A. Geometry of dipole antenna element

The configuration of the dipole antenna element is depicted in Fig. 1. It is printed on a FR4 substrate with a relative dielectric constant of 4.4, a loss tangent of 0.02 and a dimension of $L \times W \times h$. The antenna is fed at the bottom edge through a 50 Ω SMA connector. The microstrip feeding structure comprises microstrip lines of different widths and a sector open-ended branch, which functions as a broadband unbalance-to-balance transition [13]. The microstrip line directly connected to the inner conductor of the SMA has a width of W_{f1} and a length of L_{f1}. After feeding through a trapezoidal patch with a length of L_{f2}, W_{f1} is transformed into a width of W_{f2}, and then it is connected to a sector open-ended branch with a radius of R and an angle of θ.

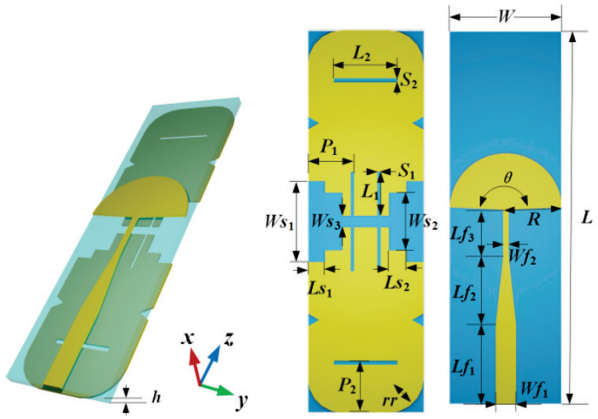

(a) (b) (c)

Fig. 1. Configuration of the dipole antenna element: (a) 3D view, (b) top view, and (c) bottom view.

The upper trimmed rectangle patches serve as radiating elements. The rectangle patch with an area of $L \times W$ is divided into two parts by three stepped slots that traverse it. Each part features two vertical slots ($L_1 \times S_1$) located next to the stepped slots and a horizontal slot ($L_2 \times S_2$), which improves the impedance matching of the antenna. Other specific dimensions have been marked in Fig. 1 in detail.

With trimmed rectangle patches and microstrip feeding structure, the antenna element is significantly reduced, which has an electric size of $0.11\lambda_L \times 0.33\lambda_L$ (λ_L corresponding to the lowest frequency), and the bandwidth is expanded. Detailed dimension parameters of the VHF/UHF antenna element can be found in Table 1.

Table 1: Dimension parameters of the VHF/UHF dipole antenna element (unit: mm)

Parameter	Value	Parameter	Value
L	660	W_{s1}	160
W	220	L_{s1}	30
W_{f1}	3.76	W_{s2}	90
L_{f1}	132	L_{s2}	3
W_{f2}	1	W_{s3}	12
L_{f2}	120	L_1	97
L_{f3}	80	S_1	5.5
R	110	L_2	80
θ	175	S_2	4
P_1	85	rr	90
P_2	100	h	2

B. Antenna element performance and analysis

The proposed antenna element was simulated and optimized in CST STUDIO SUITE 2019 software. The antenna is fed by an ideal wave-port in the simulation. The fabricated VHF/UHF dipole antenna is shown in Fig. 2 (a). The simulated and measured $|S_{11}|$ are illustrated in Fig. 2 (b). Simulated reflection coefficient curve shows that it operates from 149.73 MHz to 505.15 MHz ($|S_{11}| <$ -6 dB, 108.55%). The measured bandwidth covers from 116 MHz to 505 MHz ($|S_{11}| <$ -6 dB, 125.28%). The difference between the simulated and measured results is mainly due to the practical coaxial connector. In addition, the difference of the dielectric constant in simulation and fabrication will also cause a slight frequency shift. From Fig. 2 (b), it can be seen that the modified

simulation results (blue line) agree better with the measured ones, where the coaxial connector was modeled in simulation and the relative dielectric constant of the substrate was changed to 4.8.

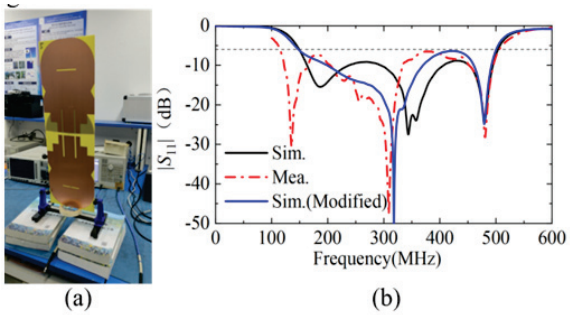

Fig. 2. The fabricated VHF/UHF dipole antenna: (a) 3-D view and (b) simulated and measured $|S_{11}|$.

The basic working principle of the broadband antenna is to excite multiple resonant modes which are close to each other. To demonstrate the basic working principle of the antenna, surface current distributions at different resonant frequencies are presented in Fig. 3. It can be seen that current distribution primarily concentrates on the edge of the patches at 187 MHz and the effective current path is the longest, which determines the lowest resonance. At 358 MHz, current distribution concentrates on the four slots, while it concentrates on the two slots at 480 MHz. It can be seen that as the operating frequency increases, the effective current path becomes shorter.

Due to the limitation of the anechoic chamber, where the minimum frequency is 1 GHz, a 10:1 scaled

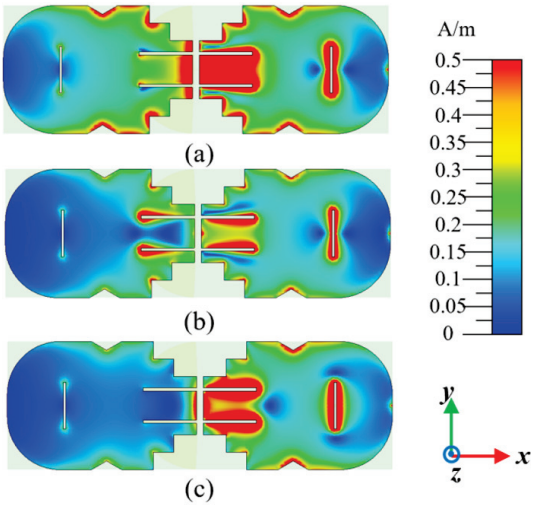

Fig. 3. Surface current distributions of the VHF/UHF antenna at (a) 187 MHz, (b) 358 MHz, and (c) 480 MHz.

model was fabricated and tested, as shown in Fig. 4 (a). The 10:1 scaled model exhibits a slight variation in structure with the VHF/UHF antenna, primarily due to limitations imposed by the dielectric substrate and the cost. Simulated and measured return loss and gain of the 10:1 scaled antenna element were conducted in an anechoic chamber as plotted in Figs. 4 (a) and (b).

The simulated bandwidth covers from 1.51 GHz to 5.08 GHz ($|S_{11}| < -6$ dB, 108.43%), as shown by the black solid line Sim.I. The measured bandwidth

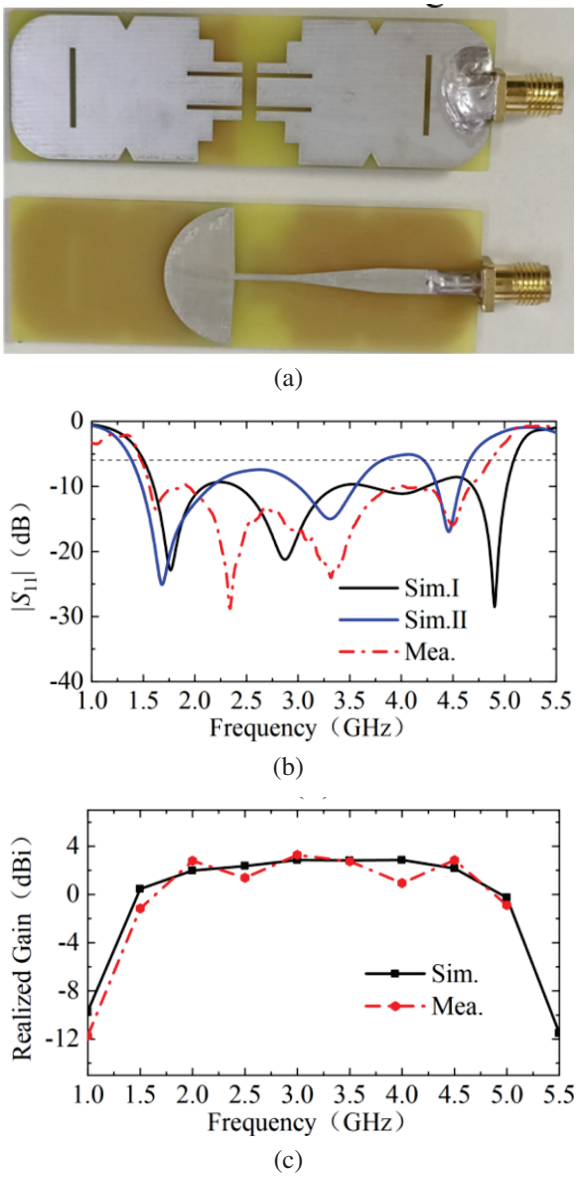

Fig. 4. Fabricated 10:1 scaled antenna element and its experiment results: (a) top view and bottom view, (b) simulated and measured $|S_{11}|$, and (c) simulated and measured gain.

(red dashed line) covers from 1.48 GHz to 4.86 GHz (106.62%). The measured bandwidth is in good agreement with the simulated one, except those resonant frequencies shift towards lower frequencies. We changed the dielectric constant of FR4 from 4.4 to 4.8, and the new simulation result is denoted as Sim.II in Fig. 4 (b). It can be seen that the resonant frequencies of Sim.II agree better with the measured resonant frequencies. In addition, coaxial connectors and soldering may influence the resonance frequency shift.

Realized radiation patterns in the E-plane and H-plane ($\theta = 90°$ plane) at 1.5, 2.5, 3.5, and 4.5 GHz are depicted in Fig. 5. It is evident that the out-of-roundness becomes worse with the increasing of working frequency, although the antenna's omnidirectional characteristics in the broadband spectrum remain observable. The asymmetry of the E-plane can be attributed to the influence of the substrate and feeding structure.

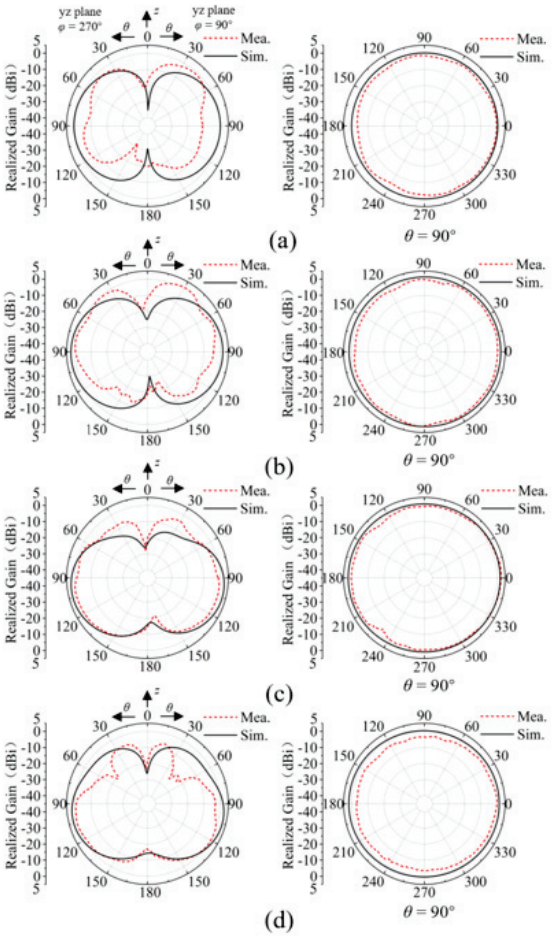

Fig. 5. Measured and simulated radiation patterns of the proposed 10:1 scaled model dipole antenna element: (a) 1.5 GHz, (b) 2.5 GHz, (c) 3.5 GHz, and (d) 4.5 GHz.

III. ANTENNA ARRAY AND EXPERIMENTAL VALIDATION

A. Antenna array structure and principle

Based on the proposed dipole antenna element, an antenna array is constructed, where four elements are arranged in a circular array configuration with a radius $r = 25$ mm, as shown in Fig. 6 (a). Circular array antennas have found extensive applications in systems such as radio direction finding, radar navigation, and underground detection [14–17]. Their advantages lie in the ability to generate both omnidirectional patterns and directional patterns with the main lobe pointing towards the normal direction of the array. The antenna structure of a uniform circular array makes its azimuth scanning angle higher than that of a linear array or rectangle array.

The overall antenna array fits in a volume of 53.2 $\times$ 53.2 $\times$ 66 mm^3. When Ant.I is excited and the other three antennas are terminated with 50 Ω matched loads, a directional pattern is realized, as plotted in Fig. 6 (b).

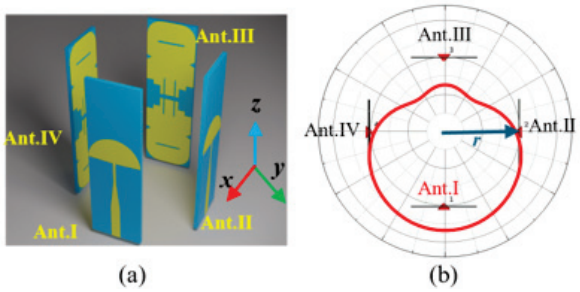

Fig. 6. Geometry of the proposed antenna array and reconfigurations for directional pattern ($r = 50$ mm): (a) 3-D view and (b) directional pattern when Ant.I is fed.

When the other three antennas are excited in the same way, three directional beams can be achieved. These four directional beams are at an interval of 90° in the H-plane ($\theta = 90°$ plane). Since the bandwidth of the antenna element is wide, pattern reconfigurability can also be realized over a wide frequency range The impact of the mutual coupling is investigated in the next section.

B. Results and discussion

The experimental setup of the proposed antenna array is shown in Fig. 7. Simulated and measured S parameters are plotted in Fig. 8. The isolation between the elements is better than 12.5 dB, and the $|S_{11}|$ is less than -6 dB over the frequency range 1.66-4.78 GHz. In a practical testing environment, S_{21} and S_{41} are nearly

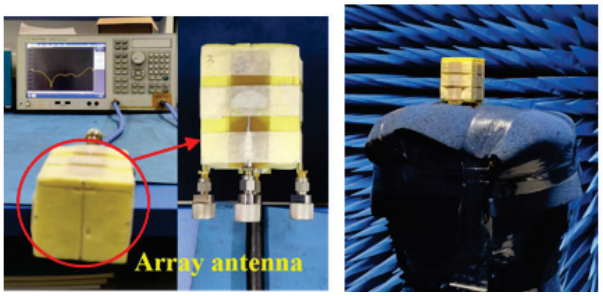

(a) (b)

Fig. 7. Photograph of the fabricated 10:1 scaled antenna array and its experimental scenario: (a) measurement of *S* parameters and (b) measurement of the radiation patterns.

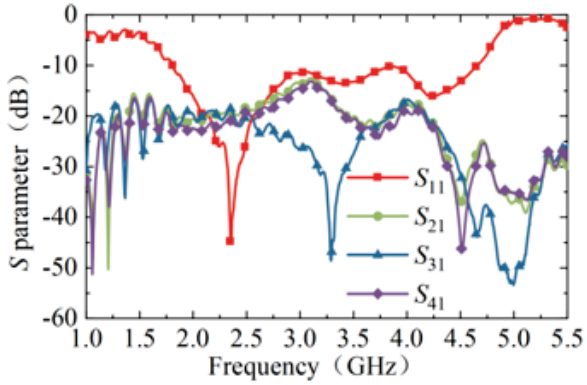

Fig. 8. Measured *S* parameter of the antenna array.

identical due to structure symmetry. When using the same operation to feed the other three ports separately, three directional beams are also obtained.

Radiation characteristics of the antenna array were evaluated in an anechoic chamber similarly. The radiation patterns at different frequencies (2, 3, and 4 GHz), when one element is fed and other ports are terminated by matched loads, are shown in Fig. 9. The maximum horizontal gain in 2 GHz, 3 GHz, and 4 GHz are 2.5 dBi, 4.9 dBi, and 3.1 dBi, corresponding to the FBR with 12.4 dB, 9.8 dB, and 13.1 dB, respectively. All results show directional beams in the azimuth plane with relatively high FBR.

The small deviation between the simulated measured results may be caused by the difference between the simplified wave-port model in simulation and the actual dimensions of coaxial cables and matching loads. In addition, the small size of the antenna results in a relatively low gain in lower frequency measurement. The welding and fine features near the feed ports also introduce adverse effects.

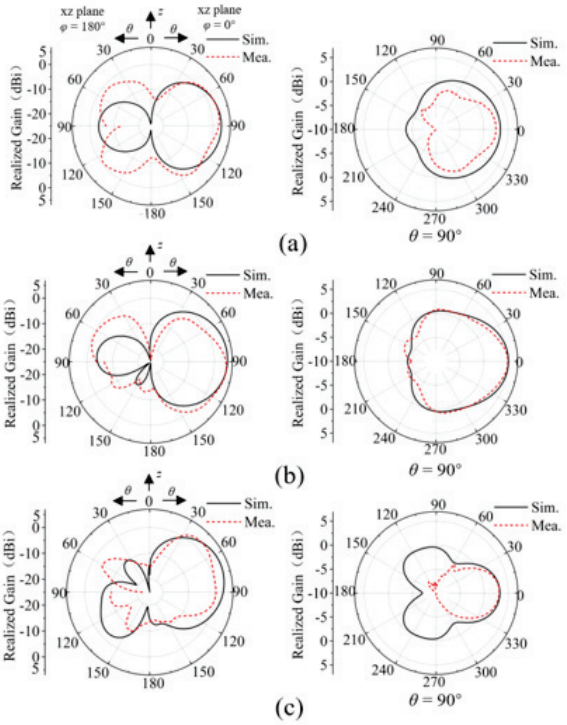

Fig. 9. Simulated and measured radiation patterns of the proposed 10:1 scaled model antenna array: (a) 2 GHz, (b) 3 GHz, and (c) 4 GHz.

IV. CONCLUSION

This paper proposed a miniaturized and broadband pattern-reconfigurable VHF/UHF antenna which features four directional beams with high FBR in the horizontal plane. A dipole VHF/UHF antenna element characterized by its compact size, stable horizontal gain, wide bandwidth (116-505 MHz, a relative bandwidth of 108.55%), and omnidirectional pattern is designed firstly. Then, a 10:1 scaled model is fabricated and tested. Measurement results show that the impedance bandwidth of antenna element covers from 1.48 to 4.86 GHz (a relative bandwidth of 106.62%) with omnidirectional characteristics. An antenna array with directional beams is designed and tested afterwards. The overall 10:1 scaled antenna array measures $53.2 \times 53.2 \times 66$ mm^3 ($0.27\lambda_L \times 0.27\lambda_L \times 0.33\lambda_L$). Measured results reveal directional beams can be achieved in the azimuth plane with a relatively high FBR within 2-4 GHz. More flexible beams can be generated by exciting more elements or changing the feeding phase of each port in the future works.

ACKNOWLEDGMENT

This work is supported by the National Natural Science Foundation of China under Grant No. 61971469, the Science and Technology Commission Shanghai

Municipality under Grant No. 18ZR1413500, the Open Project Program of the State Key Laboratory of Millimeter Waves under Grant No. K202109 and Fundamental Research Funds of Shaanxi Key Laboratory of Artificially-Structured Functional Materials and Devices (AFMD-KFJJ-21105).

REFERENCES

[1] S. R. Kingston, H. Ellis, M. U. Saleh, E. J. Benoit, A. Edun, C. M. Furse, M. A. Scarpulla, and J. B. Harley, "Spread spectrum time domain reflectometry and steepest descent inversion spread spectrum time domain reflectometry and steepest descent inversion," *Applied Computational Electromagnetics Society (ACES) Journal*. vol. 36, no. 2, pp. 190-198, 2021.

[2] Y. Xia, Y. Li, and W. Xue, "A low profile miniaturization low frequency wideband antenna using passive lumped elements loading," *Applied Computational Electromagnetics Society (ACES) Journal*, vol. 35, no. 1, pp. 31-37, 2020.

[3] C. Wang, B. Yuan, J. Mao, and W. Shi, "Dual-sleeve wideband monopole antenna for shipborne systems in VHF band," *Electron. Lett.*, vol. 54, no. 19, pp. 1102-1104, 2018.

[4] M. Bod, M. Ahmadi-Boroujeni, and K. Mohammadpour-Aghdam, "Design of a low-cost broadband loaded dipole antenna for VHF/UHF frequency range," *IET Microw. Antennas Propag.*, vol. 13, no. 12, pp. 1983-1988, 2019.

[5] C. Wang, B. Yuan, W. Shi, and J. Mao, "Low-profile broadband plasma antenna for naval communications in VHF and UHF bands," *IEEE Trans. Antennas Propag.*, vol. 68, no. 6, pp. 4271-4282, 2020.

[6] M. Mirmozafari, R. Ma, F. T. Dagefu, and N. Behdad, "A compact wideband multi-beam antenna for VHF/UHF directional networking applications," *IEEE Trans. Antennas Propag.*, vol. 70, no. 11, pp. 10113-10122, 2022.

[7] L. Batel, A. Clemente, and C. Delaveaud, "High-gain wideband and superdirective electronically-beam-switchable antenna for smart communication objects," in *2022 16th European Conference on Antennas and Propagation (EuCAP)*, pp. 1-5, 2022.

[8] L. Batel, A. Clemente, and C. Delaveaud, "Superdirective and compact electronically-beam-switchable antenna for smart communication objects," in *2019 13th European Conference on Antennas and Propagation (EuCAP)*, pp. 1-4, 2019.

[9] L. Xing, J. Zhu, Q. Xu, D. Yan, and Y. Zhao, "A circular beam-steering antenna with parasitic water reflectors," *IEEE Antennas and Wirel. Propag. Lett.*, vol. 18, no. 10, pp. 2140-2144, 2019.

[10] J. Hou, Z. Chen, Z. Wang, D. Huang, and T. A. Denidni, "Beam-sweeping antenna with beamwidth reconfigurable response," *International Journal of RF and Microwave Computer-Aided Engineering*, vol. 31, no. 12, pp. 1-9, 2021.

[11] J. Li, Q. Zeng, R. Liu, and T. A. Denidni, "A compact dual-band beam-sweeping antenna based on active frequency selective surfaces," *IEEE Trans. Antennas Propag.*, vol. 65, no. 4, pp. 1542-1549, 2017.

[12] B. Liang, B. Sanz-Izquierdo, E. A. Parker, and J. C. Batchelor, "Cylindrical slot FSS configuration for beam-switching applications," *IEEE Trans. Antennas Propag.*, vol. 63, no. 1, pp. 166-173, 2015.

[13] J. P. Zhang, Y. S. Xu, and W. D. Wang, "Ultra-wideband microstrip-fed planar elliptical dipole antenna," *Electron. Lett.*, vol. 42, no. 3, pp. 144-145, 2006.

[14] H. Liu, Y. Liu, W. Zhang, and S. Gao, "An ultra-wideband horizontally polarized omnidirectional circular connected Vivaldi antenna array," *IEEE Trans. Antennas Propagat.*, vol. 65, no. 8, pp. 4351-4356, 2017.

[15] T. Li, F. S. Zhang, F. Zhang, Y. L. Yao, and L. Jiang, "Wideband and high-gain uniform circular array with calibration element for smart antenna application," *IEEE Antennas Wirel. Propag. Lett.*, vol. 15, pp. 230-233, 2016.

[16] P. Ioannides and C. A. Balanis, "Uniform circular and rectangular arrays for adaptive beamforming applications," *IEEE Antennas and Wirel. Propag. Lett.*, vol. 4, pp. 351-354, 2005.

[17] C. A. Balanis, *Antenna Theory: Analysis and Design*, 4th ed. New York: Wiley, 2016.

Haifan Li was born in Zhengzhou, Henan, China, in 2000. He is currently pursuing the master's degree of Electromagnetic Field and Microwave Technology in Shanghai University, Shanghai 200444, China. His current research is focused on pattern reconfigurable antenna and time-varying metasurface.

Tingshuang Zheng was born in Henan, China, in 2000. She is currently pursuing the master's degree of Electromagnetic Field and Microwave Technology in Shanghai University, Shanghai 200444, China. Her current research is focused on pattern reconfigurable antenna and antenna RCS reduction and metamaterials.

Yong Mao was born in Zigong, Sichuan, China, in 1981. His current research interests focus on marine antenna. He received the B.S. degree in communication engineering University of Electronic Science and Technology of China, Chengdu, China, in 2004, and M.S. degree in telecommunication engineering Huazhong University of Science and Technology, Wuhan, China, in 2009, respectively. From 2004, he was a research fellow with Wuhan Marine Communication Institute, Wuhan 430205, China. He has authored and coauthored over 20 papers in peer-reviewed journals and conference proceedings. He is Member of Hubei Provincial Institute of Communications, and Member of Chinese Institute of Electronics.

Yongjin Zhou received the B.S. degree in communication engineering from Shandong University, Jinan, China, in 2006, and Ph.D. degree in electromagnetic field and microwave technology from Southeast University, Nanjing, China, in 2011, respectively. From 2009 to 2010, he was a visiting scholar of University of Houston. From 2011 to 2012, he was a software engineer with EEBU of Marvell Technology (Shanghai) Ltd. From 2012 to 2015, he was an Assistant Professor with School of Communication & Information Engineering, Shanghai University, Shanghai, China. From 2015, he was an Associate Professor with School of Communication & Information Engineering, Shanghai University, Shanghai, China. From 2020, he was a Professor with School of Communication & Information Engineering, Shanghai University, Shanghai, China. His current research interests include plasmonic metamaterials, millimeter wave and THz functional devices, wireless energy transmission, computational electromagnetism. He has served as *Applied Computational Electromagnetics Society (ACES) Journal* guest editor and is serving as a Youth Editorial Board Member *Journal of Electronics & Information Technology*. He is serving as a Reviewer for over 20 peer-reviewed journals, such as *Nature Electronics, Photonic Research, Optics Letter, Optics Express, Appl. Phys. Express, IEEE Access, IEEE MTT, IEEE MWCL*, etc. He has served as a session chair for several International Symposiums.

An Ultra-wideband Metamaterial Absorber with Angular Stability

Ruofeng Xu[1], Xingyu Ma[1], Xianglin Kong[1], Shengjun Zhang[2], Jiaqi Liu[2], and Lei Zhao[1*]

[1]School of Information and Control Engineering
China University of Mining and Technology, Xuzhou 221116, China
xuruofeng@cumt.edu.cn, xymamax@163.com, xlkong@cumt.edu.cn, *leizhao@cumt.edu.cn

[2]Laboratory of Experimental Physics and Computational Mathematics
Beijing, 100000 China
zhangsj98@sina.com, ljq006@vip.sina.com

***Abstract* –** In this paper, an ultra-wideband (UWB) microwave absorber with robust angular stability is proposed. Each unit of the structure consists of three-layer stacked resistive films to effectively broaden the absorption bandwidth. A metallic via is inserted in the center of the structure, which effectively guides the TM polarization oblique incident wave power to propagate vertically and be absorbed by the resistive films, thus enhancing the angular stability of TM polarization. Within the frequency range of 3.2 GHz to 35.5 GHz, the absorptivity surpasses 90% and the fractional bandwidth reaches 167%. Within an incident angle range of 0° to 60°, the absorptivity of TE polarization remains at about 80%, and the TM polarization can be maintained at over 90%. The absorption mechanism was analyzed by surface power loss and surface current distribution. A sample was fabricated, and the measured results are consistent with the simulated ones. The absorber displays good angular stability and broad bandwidth, making it ideal for electromagnetic stealth applications.

***Index Terms* –** Angular stability, metamaterial, absorber, polarizations, ultrawideband.

I. INTRODUCTION

Electromagnetic metamaterial (MM) is an artificial electromagnetic structure with unique physical properties not found in natural materials [1–4]. In the field of wave absorption, from the microwave to visible wavelengths, a range of electromagnetic metamaterial absorbers (MMA) have been proposed by researchers [5–9]. Compared to conventional absorbers, MMA offers several advantages, including thinner thickness, excellent absorption performance, and lightweight properties [10, 11]. Initially, scientists designed high-absorption MMA based on the resonant characteristics of metallic structures, but this type of absorber often has a narrow absorption bandwidth [12, 13]. Deng et al. [14] have successfully expanded the absorption bandwidth by incorporating chip resistors into the unit structure, resulting in a relative bandwidth of up to 115%. Similarly, Xiong et al. [15] have introduced multi-layer resonant structures to achieve over 90% absorption within 8.37-21 GHz. However, as the incident angle increases, the absorptivity gradually deteriorates. To address this challenge, Yu et al. [16] have proposed a broadband and angularly stable absorber employing spoof surface plasmon polariton (SSPP), demonstrating a superior absorptivity for both TE and TM polarization within a range of 60° incident angle. Nonetheless, the absorption bandwidth gradually shifts to high frequency with increasing angles for TM polarization oblique incidence. Lin et al. [17] have presented a three-dimensional metamaterial absorber (MA) that consists of a spatially lossy transmission line (SLTL) and a resistively loaded high-impedance surface (HIS). The MA has oblique incidence angle stability of over 50°. Zhang et al. [18] have demonstrated a switchable metamaterial absorber with both ultra-wideband and narrowband states and good angular stability in the terahertz region. However, the absorption effect of TM polarization deteriorates as the incident angle increases. To broaden the potential applications, further enhancement of the absorber's angular stability is necessary. However, due to the differing responses to the two polarizations, improving the angular stability for both polarizations remains a significant challenge.

In this paper, a proposed three-layer ultra-wideband absorber exhibits excellent angular stability. The absorber utilizes a three-layer resistive film structure that can broaden the bandwidth, and the TM-polarized oblique incidence power can be efficiently conducted to the resistive film layer for loss through the metallic vias in the center of the unit, which effectively improves the bandwidth shift at TM-polarized oblique incidence. The absorption mechanism of the proposed absorber is

Submitted On: October 26, 2023
Accepted On: September 1, 2024

https://doi.org/10.13052/2024.ACES.J.390802

further analyzed in terms of surface current distribution and power loss. The proposed absorber has the following advantages: 1) The absorber has an ultra-wide absorption bandwidth; 2) the absorber can maintain a good absorptivity in the range of 0° to 60° oblique incidence angle; and 3) the absorber is endowed with a simple yet compact structure, which renders it effortless to fabricate.

II. DESIGN OF THE ABSORBER

The structure proposed in this paper, as depicted in Figs. 1 (a) and (b), comprise three-layer resistive films with different sheet resistance. (R_{S1} = R_{S2} = 400 Ω, R_{S3} = 150 Ω). The resistive films are printed on a polyethylene terephthalate (PET) substrate with a permittivity of 3.7. Each layer of resistive films is supported by polymethacrylimide (PMI) foam of different thicknesses with a permittivity of 1.05. The bottom layer is a metallic plate. A metallic via runs through the center of the absorber and contact with the metallic ground.

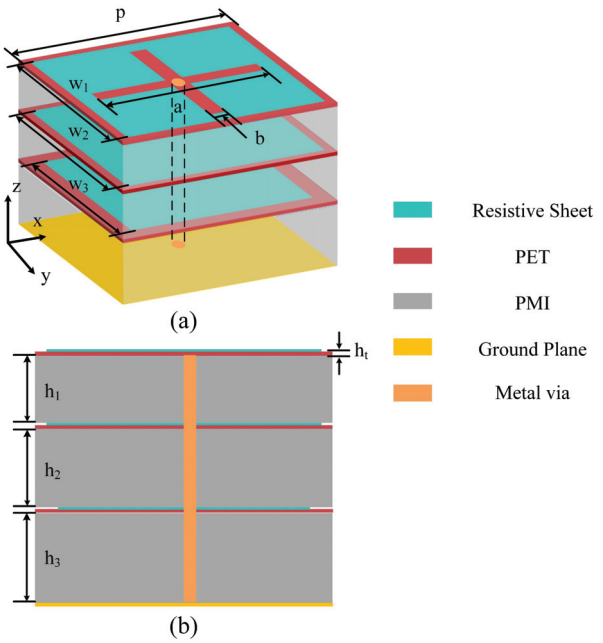

Fig. 1. (a) The structure of the proposed absorber (unit cell dimension: p = 13 mm, w_1 = w_2 = 12 mm, w_3 = 11 mm, a = 10 mm, b = 1 mm, h_1 = h_2 = 3 mm, h_3 = 4 mm, h_t = 0.175 mm); (b) side view of the unit cell.

A. Equivalent circuit analysis of the absorber without vias

The proposed absorber's equivalent circuit model is depicted in Fig. 2 (a). The resistive films can be equivalent to RLC series circuits, The capacitance C is due to

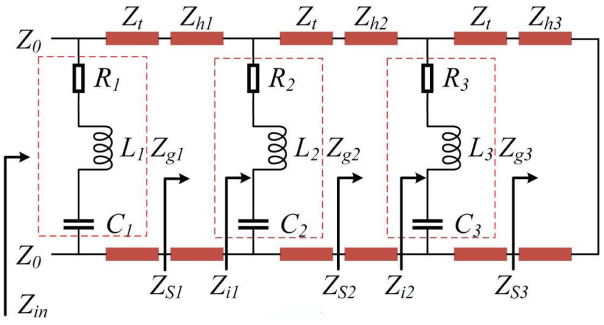

(a)

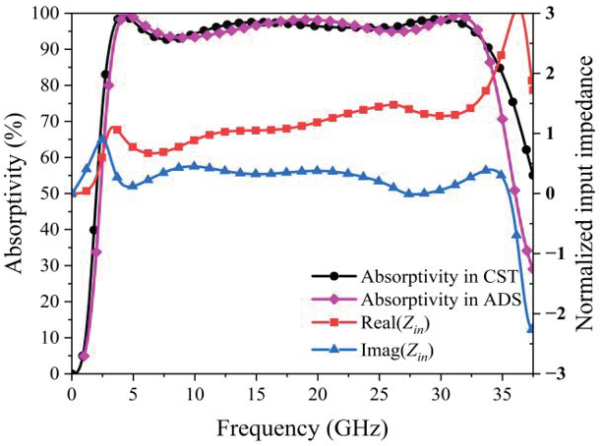

(b)

Fig. 2. (a) Equivalent circuit model diagram; (b) absorptivity of CST microwave studio, ADS, and normalized input impedance of absorber.

the edge length of the accumulated charge of the resistive films, and the inductance L is due to the area of the resistive films, where $R \approx R_s \cdot p^2/A_0^2$ and $L = \mu_0\mu_r w/\pi \cdot ln((p-w)/(w \cdot h_r\ /\ \pi)^{1/2})$ and $C = \varepsilon_0\varepsilon_r(w \cdot h_r)/(p-w)$ is the gap capacitance of the periodic patch. R_s is the sheet resistance of the resistive films, h_r is the thickness of the resistive films, and A_0 is the area of the resistive films [19, 20]. The dielectric substrate is equivalent to a transmission line. According to transmission line theory and reference [21, 22], the absorber's input impedance can be described as follows:

$$Z_{in} = Z_{g,1} \parallel Z_t \frac{Z_{S,1} + jZ_t \tan(\frac{2\pi f}{c}\sqrt{\varepsilon_{rp}}h_t)}{Z_t + jZ_{S,1}\tan(\frac{2\pi f}{c}\sqrt{\varepsilon_{rp}}h_t)}, \quad (1)$$

$$Z_{S,n} = Z_{h,n}\frac{Z_{S,n}+jZ_{i,n}\tan(\frac{2\pi f}{c}\sqrt{\varepsilon_{rf}}h_n)}{Z_{h,n}+jZ_{i,n}\tan(\frac{2\pi f}{c}\sqrt{\varepsilon_{rf}}h_n)}, \quad n = 1,2 \quad (2)$$

$$Z_{i,n} = Z_{g,n+1} \parallel Z_{ht}\frac{Z_{S,n+1}+jZ_{ht}\tan(\frac{2\pi f}{c}\sqrt{\varepsilon_{rp}}h_t)}{Z_{ht}+jZ_{S,n+1}\tan(\frac{2\pi f}{c}\sqrt{\varepsilon_{rp}}h_t)}, \quad n = 1,2 \quad (3)$$

$$Z_{s3} = j\frac{Z_0}{\sqrt{\varepsilon_{rf}}}\tan\left(\frac{2\pi f}{c}\sqrt{\varepsilon_f}h_3\right), \quad (4)$$

$$Z_{g,n} = R_n + j\omega L_n - \frac{1}{\omega C_n}, n = 1,2,3, \quad (5)$$

where ε_{rp} and ε_{rf} are the relative permittivity of PET and PMI foam substrates. Z_0 is free space impedance. The equivalent circuit model is established in the Advanced Design System (ADS), and Fig. 2 (b) presents a comparison of the simulation results obtained from ADS and CST Microwave Studio. In the frequency range of 3.2-35 GHz, the absorptivity surpasses 90% at vertical incidence. According to the normalized impedance curve in Fig. 2 (b), it is observed that the real part of the normalized input impedance is approximately 1, and the imaginary part is nearly 0. Hence, the input impedance of the absorber matches well with the impedance of the free space, leading to the achievement of broadband absorption by the absorber.

B. Performance of oblique incidence

As demonstrated by Fig. 3 (a), the absorptivity persists at approximately 90% for the TE polarization angle of incidence ranging from 0° to 45°. As the incident angle rises to 60°, the absorption declines to about 80%.

Figure 3 (b) shows that under TM polarization oblique incidence, the absorptivity remains essentially unchanged as the incident angle increases. However, the absorption bandwidth shifts to higher frequencies. When the incidence angle is 60°, the displacement is 8 GHz as against vertical incidence. To examine the actual performance of the absorber and the effect of the angle of incidence on the absorption performance, we fabricated a 299×299 mm sample with 23×23 cells, and the resistive film was printed on a PET substrate using screen-printing technique, with each layer separated by PMI foam (Fig. 4 (b)). The sample was measured in a microwave anechoic chamber in which two sets of horn antennas (2-18 GHz, 120×80 mm) were connected to two ports of a vector network analyzer (VNA) as transmitter and receiver. Respectively, the two sets of horn antennas were placed on a semi-circular track with a radius of 2 mcentered on the sample (Fig. 4 (a)). The antennas were moved on the semicircle to change the angle between the antennas and the sample during the measurement to achieve simulated oblique incidence. To ensure accurate measurement results for subsequent samples, we first measured the reflection coefficient of a metal plate of the same size as the sample. Owing to the restrictions imposed by our experimental conditions, we then measured the sample's absorptivity at an oblique incidence angle of 0-45° in the frequency range of 2-18 GHz. The measured absorbance of the samples in this range was consistent with the simulation results. The disparity between the measurement and simulation results is predominantly ascribed to errors in sample preparation and the measurement environment.

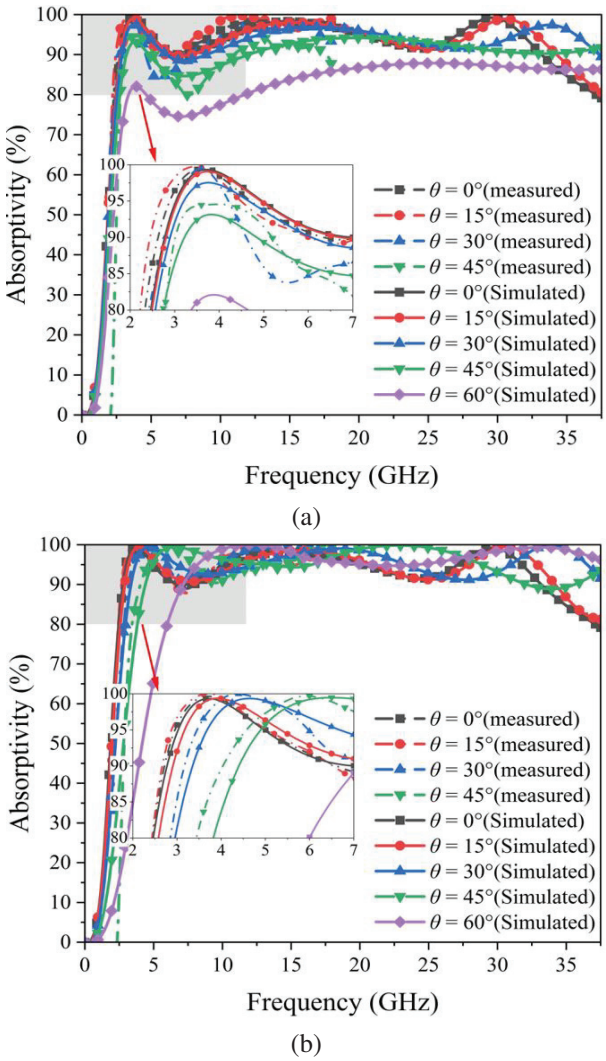

Fig. 3. Absorptivity at different polarizations at oblique incidence without vias: (a) Simulation of TE polarization; (b) simulation of TM polarization.

When TM polarization is incident obliquely, the absorption bandwidth shift occurs. This is due to the change in the equivalent impedance of the substrate as the angle of incidence increases, which causes the input impedance of the absorber to change, resulting in a mismatch with the free-space impedance.

To address this issue, a metallic via is inserted in the center of the absorber unit structure. Then the substrate layer can be considered as a multi-conductor transmission line [23]. From the perspective of the incident point, the input impedance of each layer is the parallel combination of the resistive film and substrate's impedance. The input impedance of the absorber is a parallel combination of the impedances of the individual layers, so we will analyze a single layer as an example.

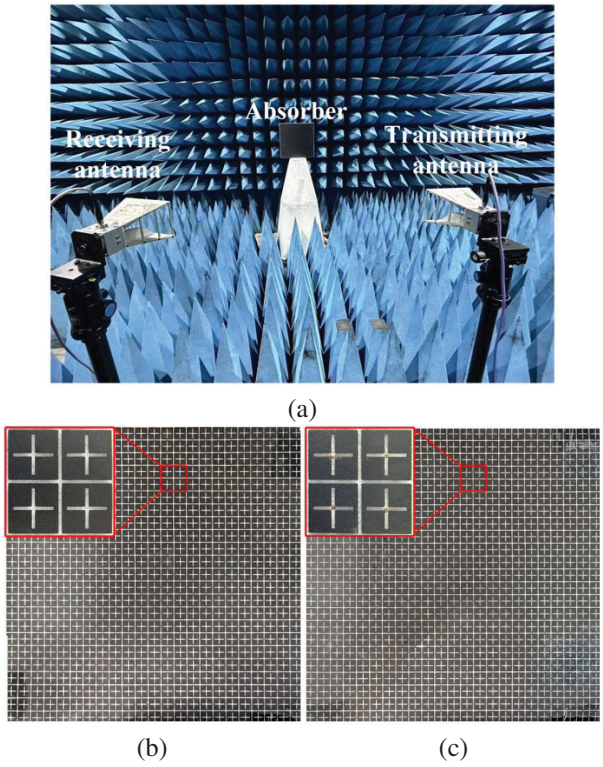

Fig. 4. (a) Measurement environment of the proposed absorber; (b) top views of the proposed absorber without vias (299×299 mm sample with 23×23 cells); (c) top views of the proposed absorber with vias (299×299 mm sample with 23×23 cells).

There are two eigenwave modes of TM-polarized incident waves in the substrates [24]. One of the eigenmodes is the TM mode propagating in the medium, which attenuates dramatically and has a negligible effect [25]. The other type of eigenmode is the TEM wave that propagates in the multi-conductor line. Its propagation factor can be decomposed into two components: One is vertical to the resistive film and the other is parallel to it. The vertical component is equal to the wavenumber propagating in the substrate, while the parallel component is the tangential component of the incident wavenumber. And because the diameter of the metallic vias is very small, the electrical polarization on the cross-section of the conductor is also very small. Additionally, due to the principle of electromagnetic wave duality, the magnetic field on the conductor remains relatively constant, so the wave impedance is basically the same as the case of no vias.

Therefore, at any incident angle, the equivalent impedance of the substrate Z_S^{TM}, as seen from the polarized incident wave of TM, is the same as that of the TEM transmission line. The length of the TEM transmission line is equal to the thickness of the absorber. This implies that Z_S^{TM} remains independent of the incident angle:

$$Z_S^{TM} = j\omega\mu \frac{\tan kh}{k} \approx j\omega\mu h. \tag{6}$$

When TM polarization oblique incidence, the input impedance of the absorber is Z_{in}^{TM}:

$$Z_{in}^{TM} = \frac{Z_g^{TM} Z_s^{TM}}{Z_g^{TM} + Z_s^{TM}}. \tag{7}$$

Because the impedance of resistive films Z_g does not depend on the angle of incidence but on the characteristics of the resistive film itself, the input impedance of the absorber is not affected by the incident angle, regardless of the angle of incidence. Moreover, the resonant frequency also remains constant. Additionally, as the electric field component of the TE polarization is vertical to the metallic vias, no induced current is generated on the metallic vias. Therefore, the metallic vias do not affect the TE polarization oblique incidence.

For TE-polarised oblique incidence, the wave impedances under the two polarisations behave differently ($Z_0^{TM} = Z_0/cos\theta, Z_0^{TE} = Z_0 cos\theta$, where θ is incident angle). This results in a different impedance match between the absorber and the free space under the two polarisations at the same incidence angle. For TE-incidence waves, the impedance match worsens throughout the absorbing band as the angle increases.

III. PERFORMANCE OF THE ABSORBER WITH VIAS

Figure 5 (a) illustrates that under TE polarization oblique incidence, the absorptivity remains above 90% up to an angle of 45°. At 60° incident angle, the absorptivity decreases to approximately 80%. The absorption effect of TE polarization oblique incidence remains essentially unchanged, indicating that vias have no effect on TE polarization. It can be seen from Fig. 5 (b) that the absorber remains angularly stable, exhibiting no shift in the absorption band at TM polarization oblique incident angle of up to 60° while retaining approximately 90% absorptivity. Figure 4 (c) displays a sample (299×299 mm with 23×23 cells) of the absorber for measurement purposes, and the comparison of simulated and measured results, shown in Figs. 5 (a) and (b), exhibit satisfactory agreement.

To gain a more intuitive understanding of the role of metallic vias, the power loss and surface current at 4 GHz were monitored before and after the improvement of the absorber at 60° oblique incidence. As shown in Figs. 6 (a)-(d), upon the incorporation of metallic vias, the TM polarization causes significant losses on the second and third resistive films that have direct contact with the metallic vias. On the other hand, the performance of TE polarization oblique incidence stays unaltered. Additionally, as revealed in Figs. 6 (e) and (f), the TM polarization oblique incidence prompts greater

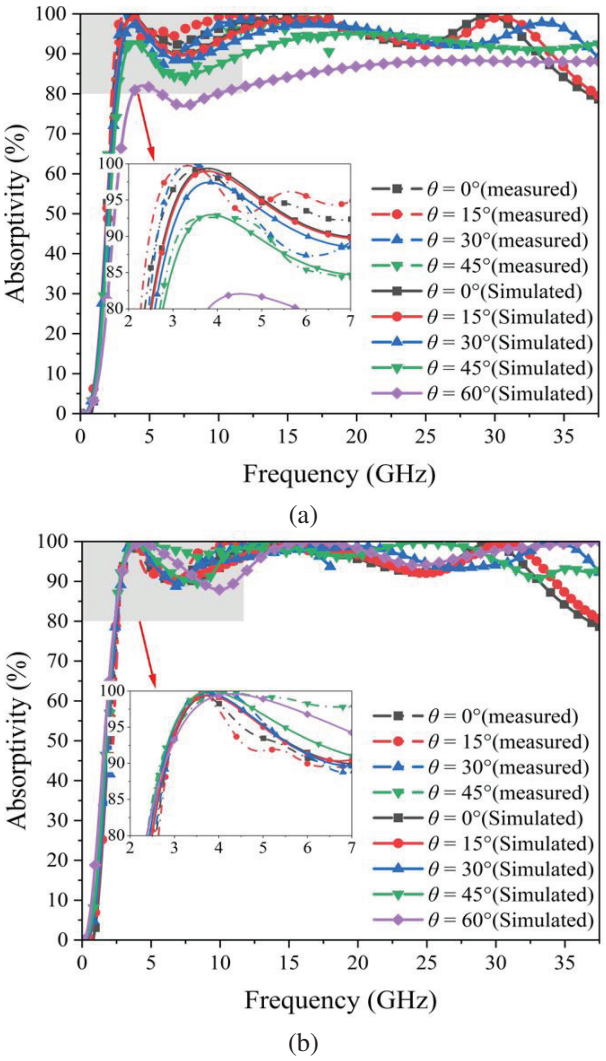

Fig. 5. Absorptivity at different polarizations at oblique incidence with vias: (a) Simulation of TE polarization; (b) simulation of TM polarization.

induced current on the vias, relative to the TE polarization oblique incidence. In cases of oblique incidence, the TM polarization wave can be guided through the vias, and loss on the resistive films, resulting in a reduction in the impact of the angle of incidence.

Table 1 presents a comparative analysis of the proposed absorber with those developed in recent years, in terms of relative bandwidth, thickness, and absorptivity at oblique incidence. It reveals that the proposed absorber has a wider fractional bandwidth, thinner thickness, and more stable oblique incidence performance than other absorbers.

FBW=2 $\times$ $(f_{max} - f_{min})/(f_{max} + f_{min}) \times 100\%$, where f_{max} is the highest frequency, f_{min} is the lowest frequency.

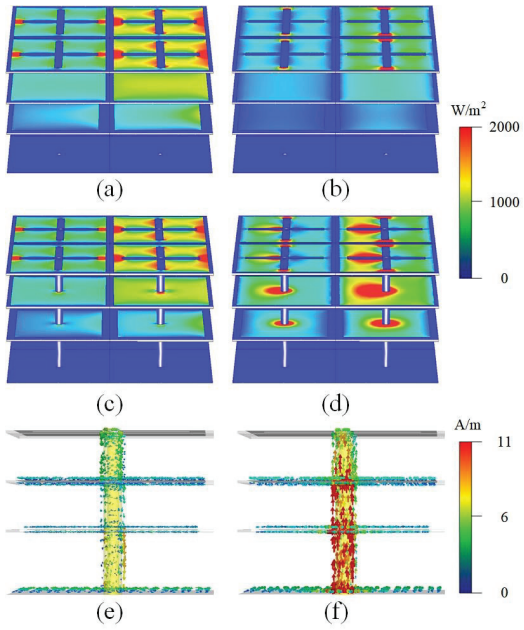

Fig. 6. Surface power loss diagram at 4 GHz at 60° oblique incidence with and without vias. (a) TE polarization without vias, (b) TM polarization without vias. (c) TE polarization with vias. (d) TM polarization with vias. Surface current at 4GHz at 60° oblique incidence with vias. (e) TE polarization. (f) TM polarization.

Table 1: Comparison of the proposed absorber with other broadband absorbers

Ref	FBW	Thickness	Absorption for Oblique Incidences	
			TE	TM
[6]	(4.73-39.04GHz) 156%	9.5mm $0.17\lambda_0$	80% at 45°	90% at 45°
[9]	(3.87-14.84GHz) 117%	6.2mm $0.19\lambda_0$	80% at 45°	90% at 50°
[26]	(3.65-13.93GHz) 117%	8mm $0.10\lambda_0$	80% at 50°	80% at 60°
[27]	(2.98-16.62GHz) 139%	9.1mm $0.13\lambda_0$	80% at 45°	90% at 45°
[28]	(2.05-8.3GHz) 120%	11mm $0.19\lambda_0$	80% at 45°	80% at 45°
This Work	(3.2-35.5GHz) 167%	10.5mm $0.09\lambda_0$	80% at 60°	90% at 60°

IV. CONCLUSION

In summary, this paper presents a design of an ultra-wideband absorber that utilizes a three-layer resistive film structure. The absorber achieves over 90% absorptivity in the range of 3.2-35.5GHz, across the C, X, Ku, K, and Ka frequency bands, with a fractional bandwidth of 167%. Additionally, the absorbers exhibit good absorption for both TE and TM polarized waves in the 0-60° incident angle range. Further analysis was conducted on the impact of metallic vias using surface currents and surface power losses. Furthermore, the measurement results align well with the simulation results, demonstrating the effectiveness of the design scheme proposed in this paper. The proposed absorber has good angular stability and absorption bandwidth and shows a potential idea for stealth applications.

ACKNOWLEDGMENT

This work is supported by the National Natural Science Foundation of China under Grant No. 51507176 and No. 62201575.

REFERENCES

[1] V. G. Veselago, "The electrodynamics of substances with simultaneously negative values of ε and μ," *Sov. Phys. Usp*, vol. 10, pp. 509-514, Jan. 1968.

[2] D. R. Smith, W. J. Padilla, D. C. Vier, S. C. Nemat-Nasser, and S. Schultz, "Composite medium with simultaneously negative permeability and permittivity," *Phys. Rev. Lett.*, vol. 84, no. 18, pp. 4184-4187, May 2000.

[3] D. R. Smith, D. C. Vier, T. Koschny, and C. M. Soukoulis, "Electromagnetic parameter retrieval from inhomogeneous metamaterials," *Phys. Rev. E,* vol. 71, no. 3, Art. no. 036617, 2005.

[4] D. R. Smith, S. Schultz, P. Markoš, and C. M. Soukoulis, "Determination of effective permittivity and permeability of metamaterials from reflection and transmission coefficients," *Phys. Rev. B, Condens. Matter,* vol. 65, no. 19, Art. no. 195104, Apr. 2002.

[5] C. Liang, X. Kong, F. Wang, R. Xu, Y. Fu, X. Pang, S. Zhang, X. Shen, and L. Zhao, "A broadband perfect metamaterial absorber with angle-insensitive characteristics," *J. Electromagn. Wave Appl*., vol. 37, no. 3, pp. 401-410, Mar. 2023.

[6] P. Chen, X. Kong, J. Han, W. Wang, K. Han, H. Ma, L. Zhao, and X. Shen, "Wide-angle ultra-broadband metamaterial absorber with polarization insensitive characteristics," *Chinese Phys. Lett.*, vol. 38, no. 2, p. 27801, Jan. 2021.

[7] R. Araneo and S. Celozzi, "Optimal design of electromagnetic absorbers," *Applied Computational Electromagnetic Society (ACES) Journal*, vol. 29, no. 4, pp. 316-327, Apr. 2014.

[8] P. Zhou, Q. Huang, L. Ji, and X. Shi, "Design of a thin broadband metamaterial absorber based on resistance frequency selective surface," *Applied Computational Electromagnetic Society (ACES) Journal,* vol. 34, no. 10, pp. 1494-1499, Oct. 2019.

[9] Lim and S. Lim, "Ultrawideband electromagnetic absorber using sandwiched broadband metasurfaces," *IEEE Antennas Wireless Propag. Lett.*, vol. 18, pp. 1887-1891, 2019.

[10] X. Lu, J. Chen, Y. Huang, Z. Wu, and A. Zhang, "Design of ultra-wideband and transparent absorber based on resistive films," *Applied Computational Electromagnetic Society (ACES) Journal*, vol. 34, no. 05, pp. 765-770, May 2019.

[11] D. Wang, K. Xu, S. Luo, Y. Cui, L. Zhang, and J. Cui, "A high Q-factor dual-band terahertz metamaterial absorber and its sensing characteristics," *Nanoscale.,* vol. 15, no. 7, pp. 3398-3407, Feb. 2023.

[12] M. B. Ghandehari, N. Feiz, and M. Alipoor, "Circuit model analysis of a polarization and wide angle independent hexagonal shaped metamaterial absorber," *Applied Computational Electromagnetic Society (ACES) Journal*, vol. 30, no. 8, pp. 909-914, Aug. 2015.

[13] F. Dincer, M. Karaaslan, E. Unal, O. Akgol, and C. Sabah, "Multi-band metamaterial absorber: design, experiment and physical interpretation," *Applied Computational Electromagnetic Society (ACES) Journal*, vol. 29, no. 3, pp. 197-202, Mar. 2014.

[14] T. Deng, Z. W. Li, and Z. N. Chen, "Ultrathin broadband absorber using frequency-selective surface and frequency-dispersive magnetic materials," *IEEE Trans. Antennas Propag.*, vol. 65, no. 11, pp. 5886-5894, Nov. 2017.

[15] H. Xiong, J. S. Hong, C.-M. Luo, and L. L. Zhong, "An ultrathin and broadband metamaterial absorber using multi-layer structures," *J. Appl. Phys.*, vol. 114, no. 6, Art. no. 064109, Aug. 2013.

[16] J. Yu, W. Jiang, and S. Gong, "Wideband angular stable absorber based on spoof surface plasmon polariton for RCS reduction," *IEEE Antennas Wireless Propag. Lett.*, vol. 19, no. 7, pp. 1058-1062, July 2020.

[17] Z. C. Lin, Y. Zhang, L. Li, Y. T. Zhao, J. Chen, and K. D. Xu, "Extremely wideband metamaterial absorber using spatial lossy transmission lines and resistively loaded high impedance surface," *IEEE Trans. Microwave Theory Tech.*, vol. 71, no. 8, pp. 3323-3332, Aug. 2023.

[18] B. Zhang and K.-D. Xu, "Dynamically switchable terahertz absorber based on a hybrid metamaterial with vanadium dioxide and graphene," *J. Opt. Soc. Amer. B Opt. Phys.*, vol. 38, no. 11, pp. 3425, Nov. 2021.

[19] F. Costa, A. Monorchio, and G. Manara, "Analysis and design of ultrathin electromagnetic absorbers comprising resistively loaded high impedance surfaces," *IEEE Trans. Antennas Propag.*, vol. 58, no. 5, pp. 1551-1558, May 2010.

[20] F. Costa, A. Monorchio, and G. Manara, "An equivalent circuit model of frequency selective surfaces embedded within dielectric layers," *Proc. IEEE Antennas Propag. Soc. Int. Symp.*, pp. 1-4, 2009.

[21] Q. Zhou, X. W. Yin, F. Ye, R. Mo, Z. M. Tang, L. F. Cheng, and L. T. Zhang, "Optically transparent and flexible broadband microwave metamaterial absorber with sandwich structure," *Appl. Phys. A*, vol. 125, no. 2, Art. no. 131, 2019.

[22] L. Sun, H. Cheng, Y. Zhou, and J. Wang, "Broadband metamaterial absorber based on coupling resistive frequency selective surface," *Opt. Exp.*, vol. 20, no. 4, pp. 4675-4680, Feb. 2012.

[23] R. E. Diaz, J. T. Aberle, and W. E. McKinzie, "TM mode analysis of a Sievenpiper high-impedance reactive surface," *in Proc. IEEE Antennas Propag. Symp.*, pp. 327-330, 2000.

[24] C. R. Simovski, S. A. Tretyakov, and P. de Maagt, "Artificial high impedance-surfaces: Analytical theory for oblique incidence," *Proc. Antennas Propag. Soc. Int. Symp.*, vol. 4, pp. 434-437, 2003.

[25] S. I. Maslovski, S. A. Tretyakov, and P. A. Belov, "Wire media with negative effective permittivity: A quasistatic model," *Microw. Opt. Technol. Lett.*, vol. 35, no. 1, pp. 47-51, Oct. 2002.

[26] J. F. Chen, Z. Y. Hu, G. D. Wang, X. T. Huang, S. M. Wang, X. W. Hu, and M. H. Liu, "High-impedance surface-based broadband absorbers with interference theory," *IEEE Trans. Antennas Propag.*, vol. 63, no. 10, pp. 4367-4374, Oct. 2015.

[27] J. F. Wei, Y. He, S.W. Bie, S. Wu, Z. P. Lei, W. Deng, Y. T. Liu, Y. L. Zhang, C. L. Li, J. Q. Ai, and J. J. Jiang, "Flexible design and realization of wideband microwave absorber with double-layered resistor loaded FSS," *J. Phys. D, Appl. Phys.*, vol. 52, no. 18, Art. no. 185101, May 2019.

[28] Y. Chang and Yung L. Chow, "Broadband microwave absorber based on end-loading folded-dipole array," *Applied Computational Electromagnetic Society (ACES) Journal,* vol. 34, no. 9, pp. 1327-1333, Sep. 2019.

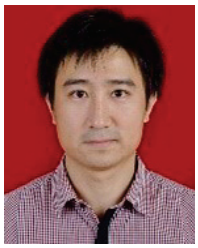

Ruofeng Xu received the B.Sc. (2004) degree from Suzhou University in electronics and science and technology and the M.Sc. (2006) and Ph.D. (2010) degrees in electronic engineering from the University of Kent, UK. He was the visiting scholar (2018) for one year in Rutgers University, USA. Now he has been a lecturer in School of Information and Control Engineering, China University of Mining and Technology. His main research directions are microwave technology and application.

Xingyu Ma has been a masters student at the School of Information and Control Engineering, China University of Mining and Technology. His main researches are on microwave absorbers, frequency select surfaces, etc.

Xianglin Kong has a doctoral degree in Information and Control Engineering at China University of Mining and Technology. His main research interests include metamaterial absorbers and encoded metasurfaces.

Shengjun Zhang has been a researcher at Laboratory of Experimental Physics and Computational Mathematics. His main research directions are on electromagnetic waves technologies, etc.

Jiaqi Liu has been a researcher at Laboratory of Experimental Physics and Computational Mathematics. His main research directions are on electromagnetic waves technologies, etc.

Lei Zhao has been a professor and doctoral supervisor in School of Information and Control Engineering, China University of Mining and Technology. He has been a senior member of IEEE, member of the Antenna Branch of the China Electronics Society, and chairman of IEEE AP-S Chapter Xuzhou. His main researches are on RF microwave devices, new electromagnetic materials, vortex wave communication, computational electromagnetics, etc.

Ultra-wideband Planar Magic-T using Interlayer Coupling 3 dB Directional Coupler and Branch-loaded Phase Shifter

Yanzhen Shi[1], Dapeng Chu[1], and Yongjin Zhou[1,2,3]

[1]Shanghai Collaborative Innovation Center of Intelligent Sensing Chip Technology
School of Communication and Information Engineering, Shanghai University, Shanghai 200444, China
yanzhen_shi@163.com, chudapeng1997@163.com

[2]State Key Laboratory of Millimeter Waves, School of Information Science and Engineering
Southeast University, Nanjing 210096, China

[3]Shaanxi Key Laboratory of Artificially-Structured Functional Materials and Devices
Air Force Engineering University, Xi'an 710051, China
yjzhou@shu.edu.cn

Abstract – In this paper, we propose an ultra-wideband magic-T operating in the frequency band from 1.2 to 4 GHz with a relative bandwidth of 108%, which is based on an interlayer coupling 3 dB directional coupler and a branch-loaded 90° phase shifter. Compared to traditional magic-T structures, it can operate within an ultra-wideband range and has the advantages of a simple structure and easy processing. Simulation and experimental results demonstrate excellent amplitude and phase stability. When the input is at the sum port, the phase error at each output port is less than 2.8°. For the difference port input, the phase error at each output port is less than 7.6°. Furthermore, the overall amplitude imbalance is less than 2.1 dB, the transmission coefficient is below −7.4 dB, and the isolation is greater than 11 dB. It can be used in ultra-wideband phased array systems to generate sum-and-difference beams for direction finding.

Index Terms – Coupler, magic-T, phase shifter; ultra-wideband.

I. INTRODUCTION

In recent years, military systems have been operating in a very wide frequency range with bandwidth requirements extending from L-band to Ka-band. Magic-T networks are widely used in phased-array radar systems as sum-and-difference networks to generate sum-and-difference signals for target direction detection, enabling radar target detection tasks. As one of the core components of radar, the magic-T network is facing higher demands. It needs to have the widest possible operating bandwidth to enable the radar to detect targets over a broad frequency range. The demand for ultra-wideband magic-T network systems (the relative bandwidth is larger than 100%) is becoming increasingly urgent.

In recent years, extensive research has been conducted on the magic-T network. However, the conventional magic-T has a narrow bandwidth, such as the coplanar magic-T based on substrate integrated waveguide (SIW) in [1], which has a bandwidth of 5.8%. References [2–4] have worked on increasing the bandwidth of SIW-based magic-T networks, achieving bandwidths ranging from 23.2% to 78.7%. A new ridge-shaped SIW is proposed in [4] to achieve 78.7% (6.4-14.7 GHz) relative bandwidth by a stepped band line optimized by genetic algorithm (GA). Despite the high performance of waveguide SIW-based magic-T, its structure is complex, more difficult to process, and more costly. To enhance the operational bandwidth, certain studies have suggested magic-T networks based on microstrip or slot lines. For example, a new broadband magic-T based on slot line T-junctions and microstrip line-slot line conversion is proposed in [5] with a bandwidth of 40%. In addition, a broadband planar magic-T using microstrip line-slot line conversion with a relative bandwidth of 70% is presented in [6]. However, these methods still cannot satisfy the ultra-wideband requirements of the system. Conventional 3 dB couplers based on microstrip or slotted lines combined with 90° phase shifters can also provide magic-T functionality [7–10]. Reference [8] achieves a magic-T with a relative bandwidth of 40%. Reference [9] achieves a relative bandwidth of 89% (5-13 GHz) by narrow-edge coupling and wide-edge coupling. Most of the above studies have focused on X-band and C-band; there are relatively few studies on magic-T covering L-band.

Submitted On: October 31, 2023
Accepted On: June 26, 2024

https://doi.org/10.13052/2024.ACES.J.390803

In view of the wide application of L/S-band in communication and satellite, we propose an ultra-wideband magic-T network that covers the L/S bands. The network is based on a 3 dB coupler and a 90° phase shifter, operating in the 1.2-4 GHz range, with a relative bandwidth of up to 108%. The transmission coefficient is less than −7.4 dB, and the phase imbalance is less than 2.8°, with an amplitude imbalance of less than 2.1 dB.

II. MAGIC-T DESIGN

The ultra-wideband magic-T consists of a cascade of a 3 dB directional coupler and a 90° phase shifter, which can be applied as a sum-and-difference network in phased-array systems, and its network topology is shown in Fig. 1.

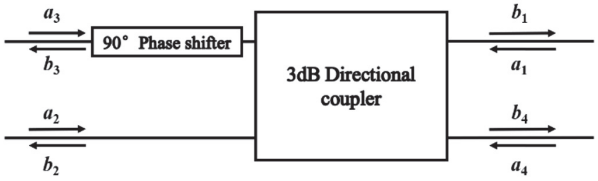

Fig. 1. Schematic diagram of the proposed magic-T.

Assume that a_i represents the normalized voltage of the incident wave and b_i represents the normalized voltage of the incident wave. For the orthogonal hybrid network, the phase of the coupled output port 3 lags behind that of the straight-through port 2 by 90° when the electromagnetic wave is input from port 1, so the scattering matrix S of the 3 dB directional coupler is:

$$S=\frac{1}{\sqrt{2}}\begin{bmatrix}0 & j & 1 & 0\\ j & 0 & 0 & 1\\ 1 & 0 & 0 & j\\ 0 & 1 & j & 0\end{bmatrix}. \tag{1}$$

The coupled output port 3 in turn passes through a 90° phase shifter, so the normalized value of the reflected wave voltage of the cascade network can be expressed as:

$$\begin{bmatrix}b_1\\ b_2\\ b_3\\ b_4\end{bmatrix}=\frac{1}{\sqrt{2}}\begin{bmatrix}0 & j & 1 & 0\\ j & 0 & 0 & 1\\ 1 & 0 & 0 & j\\ 0 & 1 & j & 0\end{bmatrix}\begin{bmatrix}0\\ a_2\\ a_3e^{j\frac{\pi}{2}}\\ 0\end{bmatrix}=\frac{1}{\sqrt{2}}\begin{bmatrix}j(a_2+a_3)\\ 0\\ 0\\ a_2-a_3\end{bmatrix}. \tag{2}$$

From the above equation, we have:

$$\begin{aligned}b_2&=b_3=0\\ b_1&=\frac{1}{\sqrt{2}}(a_2+a_3)e^{j\frac{\pi}{2}}.\\ b_4&=\frac{1}{\sqrt{2}}(a_2-a_3)\end{aligned} \tag{3}$$

The above theoretical analysis shows that port 1 of this cascade network can be used as the sum port of the sum-difference network, and port 4 can be used as the difference port.

A. Interlayer coupling ultra-broadband directional coupler

The form of the 3 dB directional coupler in the proposed magic-T network uses a coupled-line directional coupler with its coupled port and straight-through port output signal power being equal, and a phase difference of 90°. For the planar coupled line directional coupler, even if the spacing between the coupled lines is close to the practical processing precision limit, it is still challenging to achieve the 3 dB coupling requirement. Scholars have also tried various methods to increase the electromagnetic coupling between planar microstrip lines, but these techniques have significantly increased the processing difficulty. To achieve an easily manufacturable and strongly coupled directional coupler based on planar microstrip lines, a multilayer microstrip structure based on interlayer coupling [11] was proposed, and Figs. 2 (a) and (b) show the top and side views of this structure, respectively. The structure includes two layers of dielectric substrate with a common metal ground in the middle layer. The microstrip transmission lines are located on the surfaces of the two layers of the dielectric substrate and coupled broadside through the coupling holes in the hollow part of the metal ground, and the size of the coupling microstrip lines and coupling holes determines the degree of coupling. By reasonably adjusting the size of the coupling area, the structure can achieve a coupling degree of 3 dB or more.

Fig. 2. Multi-layer coupling line structure: (a) top view and (b) side view.

The relationship between odd mode and even mode impedances and slot width, as well as microstrip line width, can be obtained as follows [11, 14]:

$$Z_{0e}=\frac{60\pi}{\sqrt{\varepsilon_r}}\frac{K\left(\sqrt{\frac{\sinh^2(\pi w_s/4h)}{\sinh^2(\pi w_s/4h)+\cosh^2(\pi w_1/4h)}}\right)}{K'\left(\sqrt{\frac{\sinh^2(\pi w_s/4h)}{\sinh^2(\pi w_s/4h)+\cosh^2(\pi w_1/4h)}}\right)} \tag{4}$$

$$Z_{0o}=\frac{60\pi}{\sqrt{\varepsilon_r}}\frac{K'\left(\tanh\left(\frac{\pi w_1}{4h}\right)\right)}{K\left(\tanh\left(\frac{\pi w_1}{4h}\right)\right)}$$

where $K(k)$ represents the complete elliptic integral of the first kind, $K'(k)=K\left(\sqrt{1-k^2}\right)$, Z_{0o} and Z_{0e} represent the odd mode impedance and even mode impedance, respectively, h is the thickness of the dielectric layer, w_1

is the width of the coupled microstrip lines on the top and bottom layers, and w_s is the width of the slot on the middle ground layer.

Since the length of the coupled microstrip line is $\lambda/4$ (where λ is the wavelength corresponding to the center frequency), the single-section coupled-line coupler is limited in bandwidth [12], while the magic-T network in this design needs to meet the ultra-wideband requirements. To further expand the bandwidth and improve the phase balance, in this work, a three-section $\lambda/4$ length coupled-line coupler is designed using a multi-layer microstrip structure based on interlayer coupling. The structure consists of a weakly coupled section, a strongly coupled section, and another weakly coupled section, in that order. The schematic diagram of the three-section coupled-line coupler is shown in Fig. 3. The designed coupler is symmetrical, with the first and third sections of the coupled line having the same coupling coefficients, representing the weakly coupled parts, while the second section serves as the strongly coupled part.

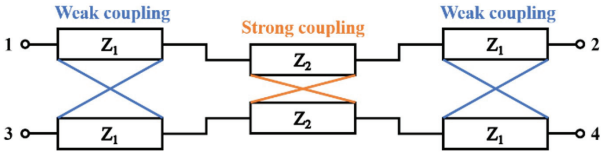

Fig. 3. Prototype three-stage coupler.

By analyzing the even and odd modes of the coupled-line coupler and referring to R. Mongia's design table [13], the characteristic impedances for each section of the 3 dB three-section coupled-line coupler can be obtained. The odd mode and even mode characteristic impedance of the first and third sections are $Z_{0o1} = Z_{0o3} = 42.00\ \Omega$, $Z_{0e1} = Z_{0e3} = 59.52\ \Omega$, the odd mode and even mode characteristic impedance of the second section are $Z_{0o2} = 14.97\ \Omega$, $Z_{0e2} = 167.02\ \Omega$, respectively. Using equations (5) and (6), we can calculate the coupling coefficients for each section. The coupling coefficients for the first and third sections of the coupled-line coupler are $C_1 = C_3 = 0.1726$, resulting in coupling degrees of $k_1 = k_3 = -15.3$ dB. Additionally, the second section exhibits a coupling coefficient of $C_2 = 0.8355$ and a coupling degree of $k_2 = -1.6$ dB:

$$C = \frac{Z_{0e} - Z_{0o}}{Z_{0e} + Z_{0o}}, \tag{5}$$

$$k = 20lgC. \tag{6}$$

Once the substrate thickness and dielectric constant are determined, and given the odd mode and even mode characteristic impedances and coupling degrees for each section, the approximate dimensions of the coupling microstrip lines and coupling holes can be calculated using equation (4).

Figures 4 and 5 show the 3D schematic and top view of the three-section coupled-line coupler, respectively. The structure consists of three layers of metal and two layers of dielectric substrate, with the dielectric substrates all having a thickness of 1 mm made of FR4 material, having a relative dielectric constant of 4.4 and a loss tangent of 0.025. The microstrip transmission lines are located in the top and bottom layers of the structure. The metal ground is located in the middle layer with apertures for coupling holes. The overall structure is symmetrically distributed along the center of the metal ground plane, which is low cost and easy to process. When the signal is input, the output signal power at the coupled port and the straight-through port is equal and the phase difference is 90°. The coupling strength of each $\lambda/4$ coupling line section is marked in Fig. 5, with the first and third sections representing weak coupling, and the intermediate second section indicating strong coupling. The microstrip lines in the weak coupling section are slotted to avoid the narrow microstrip lines from affecting the subsequent circuit design.

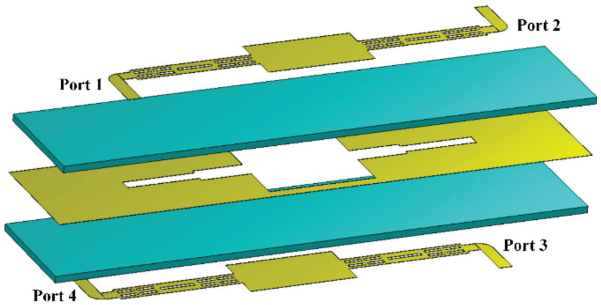

Fig. 4. 3D schematic of the three-section coupled-line coupler.

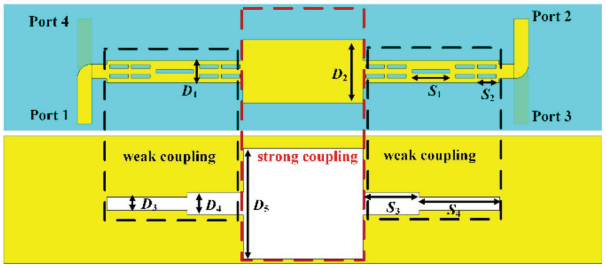

Fig. 5. Top view of the three-section coupled-line coupler.

The optimal structural dimensions obtained by modeling and optimizing each parameter of the coupler in the electromagnetic simulation software CST are shown in Table 1.

The simulation results of the optimized coupler in CST are shown in Fig. 6. From the simulation results,

Table 1: The optimized values of the coupler (unit=mm)

Parameter	Value	Parameter	Value
D_1	2.98	D_5	14.80
D_2	8.46	S_1	2.50
D_3	1.78	S_2	5.00
D_4	2.98	S_3	7.50

it can be observed that within the operating frequency range of 1.2-4 GHz, the reflection coefficient of each port is less than −12 dB. The isolation refers to the extent to which the signal at one port influences other ports during propagation. For a four-port network, isolation can be calculated using the following formula: Isolation (dB)= $-S_{ij}$ (dB). Here, i and j denote two different ports of the network, and S_{ij} represents the corresponding element in the S-parameter matrix. The isolation between ports 2 and 3, as well as between ports 1 and 4, defined as −S41 or −S23, exceeds 15 dB. The transmission coefficient of the straight-through port and the coupled port is approximately −3 dB, and the phase difference is around 90°. The amplitude imbalance is less than 1.3 dB and the phase imbalance is less than 1.8°. The coupler has good performance in all aspects and basically meets the index requirements of ultra-broadband magic-T network.

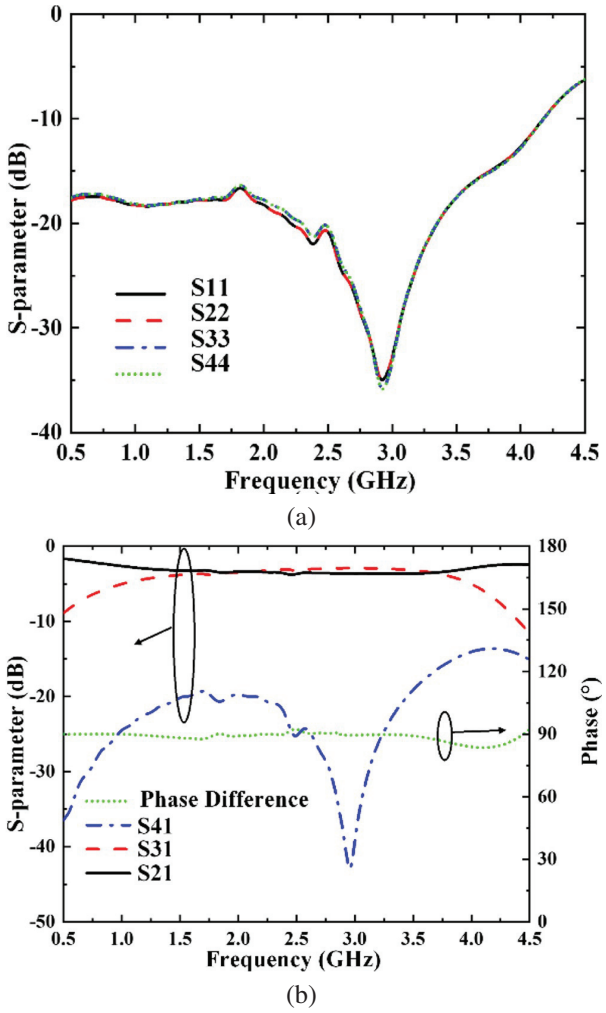

Fig. 6. Simulation results of the couple: (a) reflection coefficient and (b) phase difference between coupled port and straight-through port, transmission coefficient and isolation.

B. Branch loading type ultra-wideband phase shifter

The 90° phase shifter required in the magic-T network should also meet the ultra-wideband requirements, and the operating band of this phase shifter should be consistent with that of the 3 dB directional coupler and be structurally easy to cascade with the coupler. Compared with other types of phase shifters, the branch-loaded phase shifter can adjust the phase slope of the insertion phase shift by changing the impedance of the loaded branch [15], allowing it to achieve a constant phase shift value within a specific frequency band. This phase shifter can be realized using a single-layer microstrip structure, which simplifies the manufacturing process while ensuring stable performance. As a result, it is an excellent choice for constructing magic-T networks. The traditional branch-loaded phase shifter has a relatively narrow operating band, making it difficult to achieve a bandwidth of over three times the center frequency. To meet the bandwidth requirements of ultra-wideband magic-T networks, it's necessary to extend the bandwidth of branch-loaded phase shifters. One approach for achieving this is by using multimode resonators, which can expand the phase shifter's bandwidth to over three times the center frequency while maintaining a relatively simple structure.

According to the method in [16], considering both the amplitude and phase shift responses of the phase shifter, the characteristic impedances of the multimode resonator and the loaded branch can be determined once the reflection coefficient and phase shift deviation are established. Figure 7 shows the circuit schematic of a multimode resonator-based branch-loaded ultra-wideband phase shifter. The phase shifter consists of two branches, and the phase-shifting branch is composed of a multimode resonator with characteristic impedances Z_a and Z_b and two parallel short-circuiting branches with characteristic impedances Z_s. The length of each segment of the multimode resonator and the length of the shorting branch are both $\lambda/2$ (where λ is the wavelength corresponding to the center frequency). The reference branch is a uniform transmission line with a characteristic impedance of Z_0 and a length of l, determined by the phase difference between the two branches. When the phase shift value is 90°, the length is 2λ. According

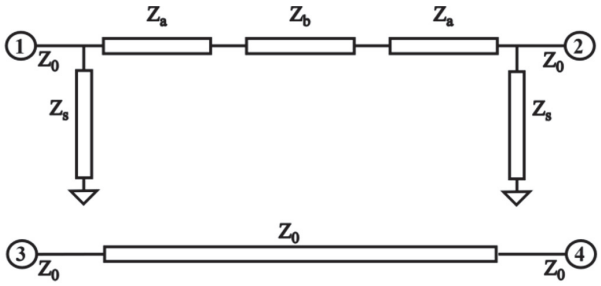

Fig. 7. The circuit schematic diagram of a multimode resonator-based dendritic loading type ultra-wideband phase shifter.

to microwave network theory, the S-parameters of the phase-shifted branch can be obtained by the transmission (ABCD) matrix, as follows:

$$S_{21}=\frac{2}{2A+B+C} \text{ and } \angle S_{21}=-\arctan\left[\frac{B+C}{j2A}\right].$$

The phase difference between the two branches, i.e. the phase shift value, can be expressed as:

$$\Delta\Phi(f)=\angle S_{21}(f)-\angle S_{43}(f).$$

Given a reflection coefficient of -20 dB, a phase shift deviation of $\pm5°$, and a port impedance of $Z_0 = 50\ \Omega$, the characteristic impedances of the multimode resonator in the 90° phase shifter are $Z_a = 62.38\ \Omega$ and $Z_b = 86.05\ \Omega$, while the characteristic impedance of the loaded branch is $Z_s = 72.96\ \Omega$. The phase shifter uses FR4 dielectric substrates with a thickness of 1 mm, similar to the coupler. It employs a single-layer microstrip structure for ease of cascading, with a center frequency of 2.6 GHz. The simulation model established in CST is shown in Fig. 8, and the specific structure dimensions obtained by fine-tuning the theoretical values are shown in Table 2.

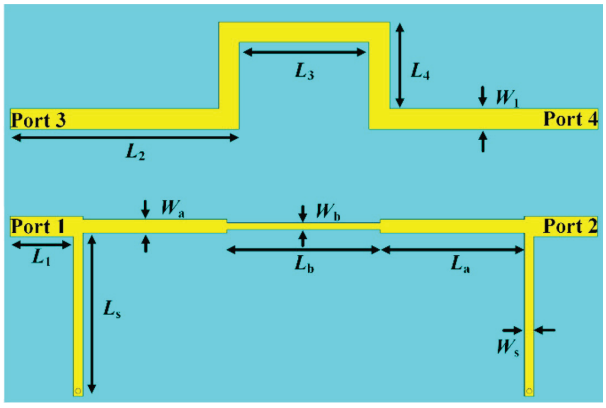

Fig. 8. Simulation model of branch-loaded ultra-wideband phase shifter.

Table 2: The optimized values of the phase shifter (unit=mm)

Parameter	Value
L_1	2.97
L_2	8.46
L_3	1.77
L_4	2.97
L_a	13.69
L_b	14.53
L_s	15.50
W_1	1.94
W_a	1.27
W_b	0.63
W_s	0.92

The simulation results, as shown in Fig. 9, demonstrate that the designed 90° phase shifter can achieve a phase shift value of 90°±5° in the operating band of 1.2-4 GHz with a reflection coefficient lower than -15.2 dB and the transmission coefficient better than -0.9 dB. With a simple structure and stable performance, it can be used to construct the ultra-wideband magic-T network.

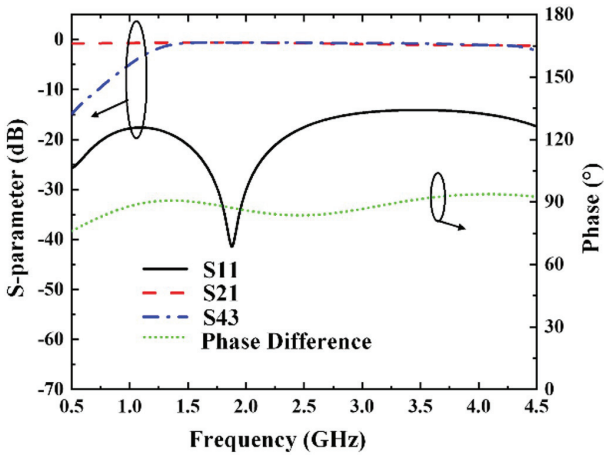

Fig. 9. Simulation results of branch-loaded ultra-wideband phase shifter.

III. EXPERIMENTS AND ANALYSIS OF ULTRA-WIDEBAND MAGIC-T NETWORKS

By cascading the 3 dB directional coupler with a 90° phase shifter, the base magic-T network structure can be obtained. To be applicable in a 4×1 phased-array system, this paper further cascades two two-to-one Wilkinson power dividers onto the basic structure. This results in the ultra-wideband sum-and-difference network that is suitable for phased array systems. The overall structure diagram is shown in Fig. 10. The designed magic-T

network includes three layers of metal and two layers of 1 mm-thick FR4 dielectric substrate. Port 1 serves as the sum port, and port 6 is the difference port. Short metal strips on each side of the feed ports are connected to the middle ground layer through metal vias, allowing for the connection of the outer conductor to ground when using SMA connectors. The structure is reciprocal in that signals can be input from ports 1 and 6 and output from ports 2, 3, 4, and 5. Conversely, signals can be input from ports 2, 3, 4, and 5 and output from ports 1 and 6.

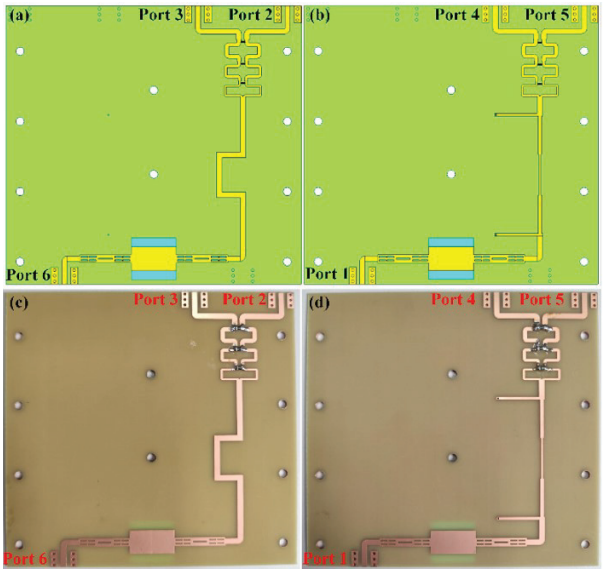

Fig. 10. Model structure and fabricated prototype of the magic-T network.

In the actual processing, there are two ways to choose. The first way is to use a multilayer board process, adding a semi-cured sheet between two layers of dielectric substrate, laminated and pressed together. The second way is to process two layers of dielectric substrate separately and then use nylon screws to fix them together. Considering the high cost of the multilayer process and the fact that the semi-cured sheet in the middle of the dielectric can have a subtle effect on the phase shift performance, this design uses the second way of layered processing and screw fixing. By reasonably adjusting the position of the screw holes, they are distributed on both sides and in the middle of the structure, so that there is fundamentally no effect on the performance of the magic-T network. The processed ultra-wideband magic-T network is shown in Fig. 10.

An Agilent E5071C vector network analyzer was used to perform the test on the ultra-wideband magic-T network. The input and output ports to be tested in the magic-T network were connected to the two ports of the vector network, and the remaining ports were connected to the matched load. The overall simulation and experimental results are shown in Figs. 11 and 12.

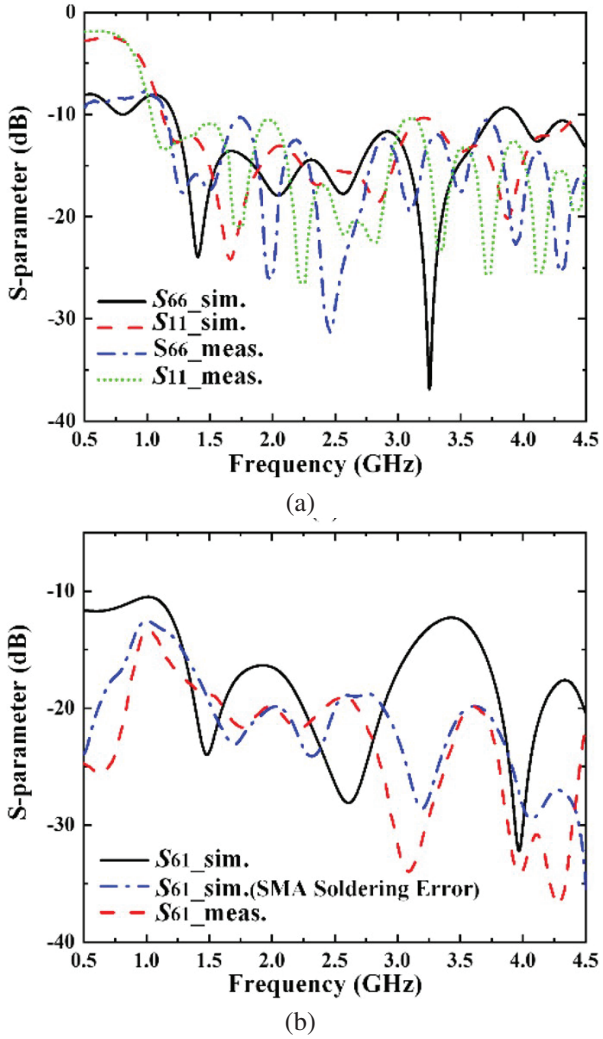

Fig. 11. Simulated and measured reflection coefficients and isolation of the proposed magic-T network.

According to the simulation and experimental results shown in Figs. 11 and 12, it is evident that within the operating frequency range of 1.2 to 4 GHz, the reflection coefficients of the sum-and-difference ports are both below −11 dB, and the isolation, which is defined as the negative of S61, is greater than 12 dB. The transmission coefficient ranges from −7.4 dB to −10.6 dB, and the amplitude imbalance between different output ports is less than 2.1 dB. In terms of the phase of the transmitted signal, the phase error of each output port is less than 2.8° for sum port 1 input and less than 7.6° for difference port 6 input. The slight difference of isolation between the experimental results and the simulation

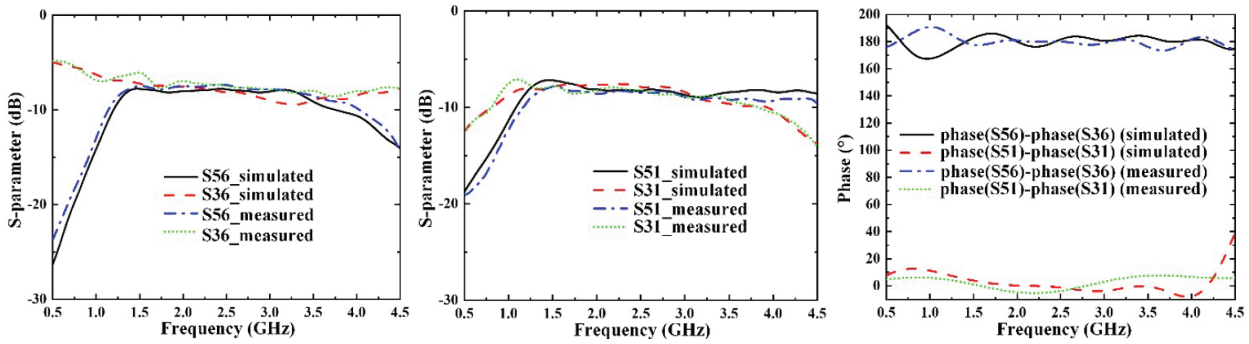

(a) (b) (c)

Fig. 12. Simulation and experimental results. (a) Transmission coefficient at the difference port 6 input, (b) transmission coefficient at the sum port 1 input, and (c) phase difference of the difference port 6 and sum port 1.

Table 3: Comparison with related research work

Ref.	Freq. (GHz)	Impedance Bandwidth (%)	Phase Imbalance (°)	Amplitude Imbalance (dB)	Return Loss (dB)	Isolation (dB)
[10]	2.42-2.48	2.45	<10	<0.5	>15.0	>25
[7]	2.5-8	105	<24	<1.0	>10.5	>13
[8]	8-12	40	<6	<1.0	>15.5	>18
[9]	5-13	89	<3	<0.5	>17.7	>20
Proposed	1.2-4	108	<7.6	<2.1	>11.0	>12

results is mainly attributed to welding errors in the SMA connectors. As shown in Fig. 11, the simulated result, taking into account the parasitic inductance and capacitance resulting from SMA connector soldering errors, is in better agreement with the experimental result.

Although the designed ultra-wideband magic-T network does not completely cover the 1-4 GHz operating band of the phased array system, it has achieved a relative bandwidth of 108% with good amplitude and phase stability, and can be used for direction finding in ultra-wideband systems by generating sum-and-difference beams. The comparison with other relevant research works is shown in Table 3.

IV. CONCLUSION

In this paper, an ultra-wideband sum-difference network based on an interlayer coupled 3 dB directional coupler and a branch-loaded 90° phase shifter is proposed, which operates in the frequency band from 1.2 to 4 GHz with a relative bandwidth of 108%. The experimental results show that the amplitude-phase stability is good. When the input is at the sum port, the phase error at each output port is less than 2.8°. For the difference port input, the phase error at each output port is less than 7.6°, and the overall amplitude imbalance is less than 2.1 dB. Compared with the traditional sum-difference network, this magic-T network has the advantages of a simple structure and ease of fabrication while providing ultra-wideband performance. It can be used in ultra-wideband phased array systems to generate sum-and-difference beams.

ACKNOWLEDGMENT

This work is supported by the National Natural Science Foundation of China under Grant No. 61971469, the Science and Technology Commission Shanghai Municipality under Grant No. 18ZR1413500, the Open Project Program of the State Key Laboratory of Millimeter Waves under Grant No. K202109 and Fundamental Research Funds of Shaanxi Key Laboratory of Artificially-Structured Functional Materials and Devices (AFMD-KFJJ-21105).

REFERENCES

[1] M. Mansouree and A. Yahaghi, "Planar magic-tee using substrate integrated waveguide based on mode-conversion technique," *IEEE Microw. Wireless Compon. Lett.*, vol. 26, pp. 307-309, 2016.

[2] F. He, K. Wu, X. P. Chen, L. Han, and W. Hong, "A planar magic-T structure using substrate integrated circuits concept," in *2010 IEEE MTT-S International Microwave Symposium*, pp. 720-723, 2010.

[3] A. Farahbakhsh, "Ka-band coplanar magic-T based on gap waveguide technology," *IEEE Microw. Wirel. Compon. Lett.*, vol. 30, pp. 853-856, 2020.

[4] J. Wang and T. Ling, "A novel ultra-wideband design of ridged SIW magic-T," *Prog. Electromagn. Res. Lett.*, vol. 82, pp. 113-120, 2019.
[5] D. Kong, T. Zheng, and F. Hou, "A novel broadband magic-T based on slotline T-junction and microstrip-slotline transition," in *IET International Radar Conference 2013*, pp. 0481-0481, 2013.
[6] K. U-yen, E. J. Wollack, J. Papapolymerou, and J. Laskar, "A broadband planar magic-T using microstrip-slotline transitions," *IEEE Trans. Microw. Theory Tech.*, vol. 56, pp. 172-177, 2008.
[7] Y. Wang, G. Hua, and J. Du, "Design of ultra-wideband magic-T using microstrip/slot coupler and phase shifter," in *2015 Asia-Pacific Microwave Conference (APMC)*, pp. 1-3, 2015.
[8] Y. Wu, F. Hou, and D. Kong, "Design of broadband planar magic-T using 3-dB branch-line coupler and phase shifter," in *Proceedings of 2014 3rd Asia-Pacific Conference on Antennas and Propagation*, pp. 81-83, 2014.
[9] Y. Chang, M. Yang, J. Fang, Z. Zhao, H. Yan, and Y. Dai, "Design of a novel ultra-wideband planar magic-T," in *2018 International Conference on Microwave and Millimeter Wave Technology (ICMMT)*, pp. 1-4, 2018.
[10] Y. Tai, Y. Ren, K. Jiang, and J. M. Zhou, "A novel electrically controlled sum and difference network based on reflective phase shifter," in *2019 IEEE 3rd Information Technology, Networking, Electronic and Automation Control Conference (ITNEC)*, pp. 2411-2415, 2019.
[11] A. M. Abbosh and M. E. Bialkowski, "Design of compact directional couplers for UWB applications," *IEEE Trans. Microw. Theory Techn.*, vol. 55, pp. 189-194, 2007.
[12] D. M. Pozar, *Microwave Engineering,* 3rd ed. New York: John Wiley & Sons, 2005.
[13] R. K. Mongia, *RF and Microwave Coupled-Line Circuits,* 2nd ed. London: Artech House, 2006.
[14] M. F. Wong, V. F. Hanna, O. Picon, and H. Baudrand, "Analysis and design of slot-coupled directional couplers between double-sided substrate microstrip lines," *IEEE Trans. Microw. Theory Techn.*, vol. 39, pp. 2123-2129, 1991.
[15] Y. P. Lyu, "Wideband phase shifters on multimode resonator with improved functionalities" [in Chinese], Ph.D. thesis, Nanjing University of Posts and Telecommunications, 2020.
[16] Y. P. Lyu, L. Zhu, and C. H. Cheng, "Single-layer broadband phase shifter using multimode resonator and shunt $\lambda/4$ stubs," *IEEE Trans. Compon. Packag. Manuf. Technol.*, vol. 7, pp. 1119-1125, 2017.

Yanzhen Shi received bachelor's degree in communication engineering from Shanghai Normal University, Shanghai, China, in 2021. She is currently pursuing the master's degree in communication and information system at Shanghai University. Her research interests include phased array antenna, direction of arrival estimation and radar detection.

Dapeng Chu was born in Qufu, Shandong, China, in 1997. He received the master's degree of communication and information system in Shanghai University, Shanghai 200444, China, in 2023. His research interests include phased array antenna, beaming scanning antenna and metamaterials.

Yongjin Zhou received the B.S. degree in communication engineering from Shandong University, Jinan, China, in 2006, and Ph.D. degree in electromagnetic field and microwave technology from Southeast University, Nanjing, China, in 2011, respectively. From 2009 to 2010, he was a visiting scholar of University of Houston. From 2011 to 2012, he was a software engineer with EEBU of Marvell Technology (Shanghai) Ltd. From 2012 to 2015, he was an Assistant Professor with School of Communication & Information Engineering, Shanghai University, Shanghai, China. From 2015, he was an Associate Professor with School of Communication & Information Engineering, Shanghai University, Shanghai, China. From 2020, he was a Professor with School of Communication & Information Engineering, Shanghai University, Shanghai, China. His current research interests include plasmonic metamaterials, millimeter wave and THz functional devices, wireless energy transmission, computational electromagnetism. He has served as ACES Journal guest editor and is serving as a Youth Editorial Board Member Journal of Electronics & Information Technology. He is serving as a Reviewer for over 20 peer-reviewed journals, such as *Nature Electronics, Photonic Research, Optics Letter, Optics Express, Appl. Phys. Express, IEEE Access, IEEE MTT,* and *IEEE MWCL*. He has served as a session chair for several international symposiums.

High Precision Multiple Parameter Measurement Sensor Based on Constitutive Parameters Near-Zero Media

Qiao Yu Li[1], Yu Wei Mao[1], and Yong Jin Zhou[1,2]

[1]Shanghai Collaborative Innovation Center of Intelligent Sensing Chip Technology
Laboratory of Specialty Fiber Optics and Optical Access Networks, Shanghai University, Shanghai 200444, China
20802117@shu.edu.cn, maoyuwei@shu.edu.cn

[2]State Key Laboratory of Millimeter Waves
School of Information Science and Engineering, Southeast University, Nanjing 210096, China
yjzhou@shu.edu.cn

Abstract **–** A high-precision multiple parameter measurement sensor based on constitutive parameters near-zero (CPNZ) media has been proposed, which can effectively and accurately predict changes in temperature and relative humidity simultaneously and independently. The dual-channel microwave sensor is composed of a double doping CPNZ substrate integrated waveguide (SIW) cavity, which has the capability to predict different parameters independently. A multi-input and multi-output model is constructed to improve the measurement accuracy by training back propagation (BP) neural network. The relative error of the predicted temperature is smaller than 1.3%, with mean square error (MSE) of ± 0.15. The relative error of the predicted relative humidity is smaller than 8.74%, with MSE of ± 0.1. The multiple parameter sensor based on CPNZ materials offers a promising platform for multiple parameter sensing research, providing essential technical support and infrastructure for the development of fields like the Internet of Things, intelligent manufacturing, and smart cities.

Index Terms **–** BP neural network, constitutive parameters near-zero media, high precision, microwave sensor, multiple parameter measurement.

I. INTRODUCTION

Sensors have found wide application across various industries [1–3], healthcare [4–5], automobiles [6–7], aerospace [8–9], and other fields. Traditional sensors suffer from a limitation as they can only measure specific physical quantities, such as temperature [10–11], humidity [12–14], or pressure [15–16]. In scenarios where multiple parameters need measurement, employing multiple sensors in conjunction becomes necessary [17–18]. This not only compromises measurement accuracy but also significantly increases system complexity and measurement costs, leading to an underutilization of sensor functionalities and benefits. Multiple parameter sensors offer a solution by simultaneously measuring multiple different physical quantities, leading to accurate, comprehensive, and cost-effective measurements. They reduce testing costs and time, facilitating automated data collection and analysis. Furthermore, the advancement of multiple parameter sensors has provided essential technical support and infrastructure for the development of fields like the Internet of Things, intelligent manufacturing, and smart cities.

One approach to achieve multiple parameter sensing involves using multiple resonators [19]. These sensors exhibit high accuracy. However, the system is complex and large. Another approach is to use multiple physical quantities (i.e. resonant frequency shift, quality factor) of a single resonator to detect multiple parameters simultaneously [20]. However, non-negligible coupling between the multiple parameters results in limited measurement accuracy and measurement range [19–20]. Therefore, conducting further research on multiple parameter sensors that offer high precision, independent and real-time measurement, integration, and low costs is of significant importance.

Microwave measurement technology has gained prominence in the field of complex permittivity measurement due to its advantages, such as high integration, measurement accuracy, and real-time performance [21]. One example of this is the use of a resonant sensor based on the improved complementary split ring resonator (CSRR) to simultaneously measure changes in complex dielectric constant and complex permeability [22]. To ensure reliable results in scientific research and production, achieving the necessary measurement accuracy is essential in various microwave measurement technologies. Metamaterials, which are artificial electromagnetic structures composed of subwavelength

Submitted On: October 31, 2023
Accepted On: September 2, 2024

https://doi.org/10.13052/2024.ACES.J.390804

resonators, exhibit novel electromagnetic characteristics and find applications in sensing, antennas, stealth technology, and other fields [23–25]. Constitutive parameters near-zero medium, including relative permittivity near-zero and relative permeability near-zero media, has unique electromagnetic control characteristics and is utilized in material characterization, sensors and other fields [26–29]. Such media has been used in high sensitivity sensors, with its field enhancement property. For instance, a double-layer relative permeability near-zero media sensor composed of microstrip lines and metal strips with metal through-holes has been employed for testing magnetic dielectric materials. Although this sensor exhibits minimal measurement error, it suffers from positioning errors that significantly impact measurement of the relative dielectric constant of the sample [29]. Additionally, the substrate-integrated (SI) photon doping method enables the realization of near-zero medium in printed circuit design, providing potential applications in material characterization and sensing [30]. Metamaterials also provide a broad platform for studying relative permittivity near-zero media [31]. For example, a multi-tunnel relative permittivity near-zero media based substrate integrated waveguide (SIW) cavity coupled with a conical microstrip line forms a dual tunnel sensor that demonstrates more than 95% accuracy in measuring dielectric constants of radome, flat substrate, and building materials [31]. Previous sensors are based on relative permittivity near-zero or relative permeability near-zero media. Constitutive parameters near-zero (CPNZ) medium is a special medium with an equivalent relative permeability of zero for the entire structure, which uses relative permittivity near-zero material as the host medium and non-magnetic medium as doping. Since sensors based on CPNZ materials possess superior sensing characteristics, exploring and developing multiple parameter sensors based on CPNZ materials hold promising prospects in the field of sensing technology.

In this paper, the study focused on the theoretical research of multiple parameter CPNZ media and introduced a high-precision dual-channel microwave sensor. The sensor is designed to address scenarios where multiple parameters change independently at the same time. To verify its dominant performance, an experiment is conducted, which is based on the fundamental principles that temperature changes with the relative permittivity of distilled water [26] and relative humidity changes with the relative permittivity of polyimide materials [27]. A neural network is introduced to the multiple-input multiple-output sensor to improve the accuracy of measuring environmental temperature and relative humidity. The obtained results clearly demonstrate that the multiple parameter CPNZ medium sensor effectively and accurately predicts both temperature and humidity of the environment concurrently. These findings highlight the potential of a sensor for practical applications in various fields where multiple parameters need to be measured with high precision and independence.

II. THEORY OF CPNZ MEDIA SENSOR

A. Sensor performance improvement based on CPNZ media

The field enhancement property of near-zero media is highly sensitive to small changes in the material, enabling the measurement of the complex dielectric constant of material. The measurement principle based on near-zero medium is studied below for the first time. According to the basic principle of near-zero medium [32], the relationship between the magnetic field $H_z(\vec{r})$ in the doping and the magnetic field H_z^{ENZ} in the relative permittivity near-zero medium is:

$$H_z(\vec{r}) = H_z^{ENZ}\psi^d(\vec{r}), \tag{1}$$

where $\psi^d(\vec{r})$ is the solution of the scalar Helmholtz equation, reflecting the proportional relationship between the doped internal field and the relative permittivity near-zero medium midfield. By solving the scalar Helmholtz equation [31]:

$$\psi^d(\vec{r}) = \frac{J_0(k_d r)}{J_0(k_d r_d)}, (0 \le r \le r_d). \tag{2}$$

Here J_0represents the first class of zero-order cylindrical Bessel functions and k_d is the wave number in the doped medium.

It can be seen from equation (2) that the field inside the doped medium fluctuates and reaches its strongest at the central point ($r = 0$), that is, the convergence of the magnetic field is reflected at this point [32]. Equation (2) can effectively calculate the enhancement effect of the incident field in the embedded medium in the structure. The integral of the tangential component of the external radiated electric field of the relative permittivity near-zero structure along the edge loop of the relative permittivity near-zero medium is equal to the total magnetic flux of the entire structure cross-section [32]. When the tangential electric field at the edge of the relative permittivity near-zero medium is large, it results in a significant total magnetic flux in the entire structure cross-section, leading to an effective internal magnetic field enhancement effect.

By designing the size of the doping material reasonably, the relative permeability of the original host medium is modified while ensuring the relative permittivity is close to zero. What is more important, the port impedance of the CPNZ structure based on the relative permittivity near-zero media matches the free-space impedance, ensuring that the field of the CPNZ is consistent with the external radiation field. As a result, 100% transmission can be achieved, regardless of the area of the CPNZ region, as long as the width of the incident

and exit ports of the waveguide is the same. Therefore, sensors based on CPNZ materials exhibit both excellent sensing performance and industrial applicability.

B. Multiple parameter sensor based CPNZ media

When doping is added to the relative permittivity near-zero medium, the cross-sectional area of each doping changes. The relative permittivity near-zero background is unchanged, and the equivalent relative dielectric constant is not affected. The equivalent permeability of the host is regulated by a single or multiple doping, with each doping causing a change in the permeability. The response of the relative permittivity near-zero cavity loaded with double doping is analyzed when dielectric cylinders with the same relative permittivity of ε_{rd} and radius of r_s are selected as dopants in this paper. The formula of equivalent relative permeability can be obtained as follows:

$$\mu_{r\_eff} = 1 + \sum_{\mathrm{d}=1}^{\mathrm{n}} \frac{A_d}{A}\left[\frac{2}{k_d r_s}\frac{J_1(k_d r_s)}{J_0(k_d r_s)} - 1\right], \quad (3)$$

where A_d is the cross-sectional area of the different doping medium, A is the cross-sectional area of the relative permittivity near-zero medium, $k_d = \varepsilon_{rd}(\omega/c)^2$, and c is the propagation velocity in vacuum.

According to the special solution of the first kind of Bessel function, equation (3) can be simplified to:

$$\bar{\mu}_{r\_eff} = 1 + \sum_{d=1}^{n} \frac{A_d}{A}\left[2\left(\frac{1}{4} + \frac{1}{4 - (k_d r_s)^2}\right) - 1\right]. \quad (4)$$

Here, $\overline{\mu}_{eff}$ is the approximate value of μ_{eff}. Substituting k_d into equation (4):

$$\bar{\mu}_{r\_eff} = 1 + \sum_{d=1}^{n} \frac{A_d}{A}\left[\frac{4c^2}{\omega^2 r_s^2 \varepsilon_{rd}} - \frac{1}{2}\right]. \quad (5)$$

For the multiple doping relative permittivity near-zero structure, the resonant phenomenon can be seen when $J_0(k_d r_s)=0$ [32] in equations (4) and (5), as long as each doping can meet the resonant requirements $k_d r_s = (\frac{\omega}{c})^2 \varepsilon_{rd} r_s \approx 2\sqrt{2}$ in the paper. For multi-doped relative permittivity near-zero media, the dielectric constants of doping are different, but the corresponding resonant frequencies are different when each doping meets the resonant conditions. It can be demonstrated that the resonances of the two channels are only related to parameters ε_{rd} and r_s, that is, there is no coupling between the two frequencies. A multi-parameter CPNZ sensor is designed based on the characteristics that each channel of multi-doped relative permittivity near-zero medium does not affect each other.

III. DESIGN AND SIMULATION OF CPNZ SENSOR

A. Multiple parameter CPNZ sensor

In order to verify the rationality of multi-parameter sensors based on CPNZ, a double-doped CPNZ materials structure is first designed. The dimensions of the relative permittivity near-zero cavity h=5 mm, l=80 mm are set, and its calculated theoretical cut-off frequency f_p is 5.45 GHz. The double doping CPNZ medium sensor is designed when equation (1) is equal to zero. The relative permittivity of the two doped cylinder ε_{rd} is 92 and radius r_s is set to 2.33 mm. Furthermore, the CPNZ cavity is simulated by a rectangular air waveguide operating near the cutoff frequency of the TE_{10} mode. Figure 1 (a) is the three-dimensional structural diagram of the proposed dual-doped CPNZ medium microwave sensor, which combines the rectangular air waveguide and two SIW cavities. The dielectric substrate of the sensor is F4B, its relative permittivity is 2.65, and loss tangent is 0.002. The length L of the whole structure is 213 mm, width W is 35.6 mm, and height h is 5 mm. The rectangular air waveguide is the CPNZ body and its length l is set to 80 mm and width w is 27.5 mm. The two SIW cavities are introduced as excitation for the CPNZ body to achieve normal propagation of electromagnetic waves. Figures 1 (b) and (c) show top view and side view of the CPNZ sensor. The sensor is excited by coaxial line, where the inner conductor of the coaxial line is embedded inside the SIW cavity. The excitation position is indicated by the dashed line in Figs. 1 (a) and (b).

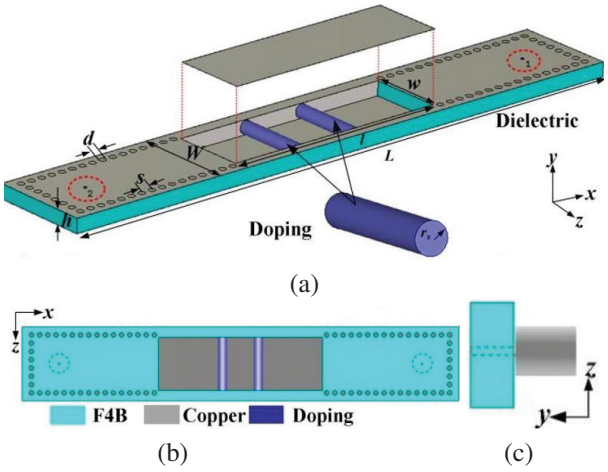

Fig. 1. (a) Structural diagram, (b) top view, and (c) side view of double-doped CPNZ media sensor.

Figure 2 (a) shows the transmission coefficients of the CPNZ structure, and it can be seen that its resonant frequency is 5.45 GHz which is coincident with the theory frequency. The electric and magnetic field distributions of the CPNZ structure at 5.45 GHz are shown in Fig. 2 (b). It can be seen that the electric field is mainly concentrated on the edge of the doped cylinder, while the magnetic field is mainly concentrated on the inside of the doped cylinder. Such field enhancement will lead to high sensitivity of the sensor to small changes in ambient dielectric change. Figure 2 (c) shows the magnetic field

phase distribution. The magnetic field phase distribution is uniform at the resonant frequency, that is, the equivalent relative permittivity and equivalent relative permeability of the doped CPNZ cavity are both zero, which is the medium characteristics of CPNZ [32].

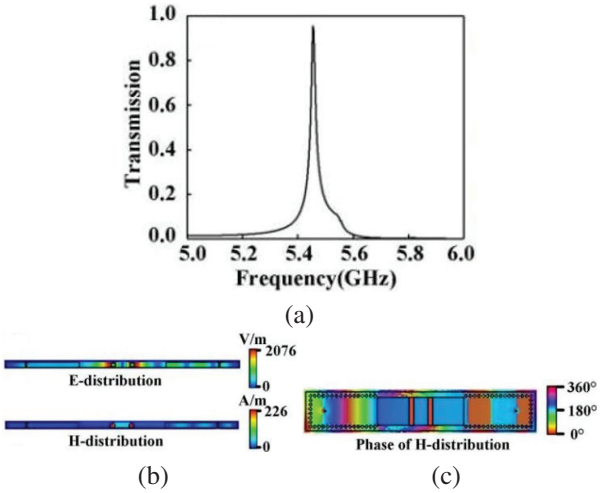

Fig. 2. Double-doped CPNZ media sensor: (a) transmission coefficients, (b) electric field distribution and magnetic field distribution at 5.45 GHz, and (c) magnetic field phase distribution at 5.45 GHz.

To achieve simultaneous measurement of multiple parameters, the double-doped sensor has been improved. Firstly, two cylinders are hollowed out and doped in the middle, and then two holes are etched on both sides of the medium substrate to facilitate the placement of the materials to be tested later. The improved dual-channel sensor structure is depicted in Fig. 3 (a). Due to processing technology limitations, a wall thickness of 0.33 mm is selected. The transmission coefficient of the dual-channel sensor without any material loaded is shown in Fig. 3 (b), where a transmission peak at 5.1 GHz is observed. The frequency change of transmission coefficient is determined by a combination of the doped area and the doped dielectric constant. After digging holes, the cross-sectional area of doping A_d becomes smaller, leading to a reduction in the equivalent permeability. In this case, the effect of area change is greater than the effect of equivalent dielectric constant, resulting in a red-shifted frequency after hollowing out the doping material. The electric field mainly concentrates on the edges of the two doped cylinders, while the magnetic field mainly concentrates on the interior of the cylinders, as shown in Fig. 3 (c). The local concentration of electric and magnetic fields is conducive to the ability of the sensor to detect multiple parameters simultaneously.

From equation (3), it is evident that when the two dopings have the same shape but different equivalent

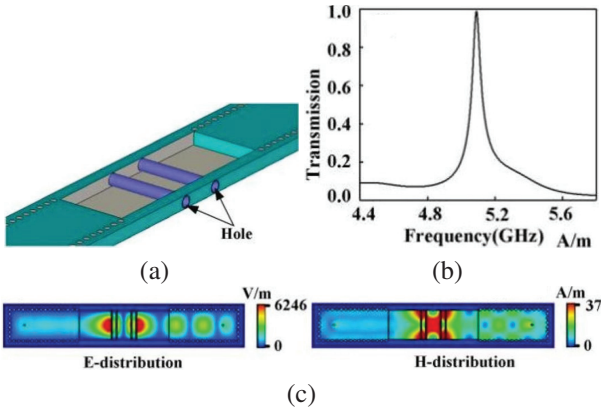

Fig. 3. (a) Structural diagram of a two-channel sensor (the upper metal is hidden), (b) transmission coefficients S_{21}, and (c) electric field distribution and magnetic field distribution at 5.1 GHz.

dielectric constants, two resonant points with distinct resonant frequencies will emerge. To verify this, two cylindrical channels were filled with polyimide material and distilled water, respectively, as illustrated in Fig. 4 (a). The transmission coefficients generate two resonant frequency points at 4.74 GHz and 5.75 GHz, as shown in Fig. 4 (b). The resonant frequency point at 4.74 GHz corresponds to the channel filled with polyimide material. Similarly, the resonant frequency point at 5.75 GHz corresponds to the channel filled with distilled water. The electric field distribution at the two resonant frequency points is presented in Fig. 4 (c). It is evident that the two channels do not influence each other significantly. At 4.74 GHz, the electric field in the channel filled with polyimide material is the strongest, whereas at 5.75 GHz, the electric field in the channel filled with distilled water is the strongest. As a result, the two resonant points remain independent of each other, which is

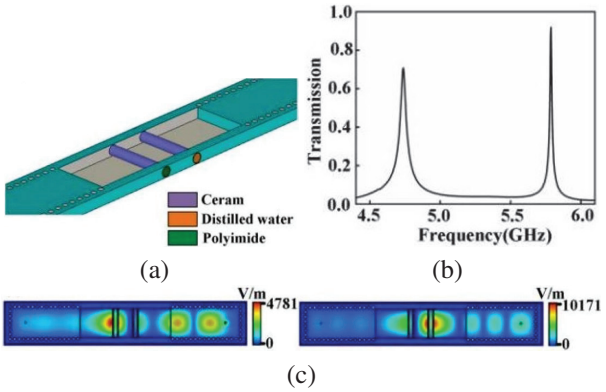

Fig. 4. (a) Dual-channel sensor loaded with polyimide material and distilled water, (b) transmission coefficients S_{21}, and (c) electric field distribution maps corresponding to 4.74 GHz and 5.75 GHz.

advantageous for accurately measuring ambient temperature and relative humidity without interference.

B. Sensor simulation data acquisition

The detection principle of the temperature and humidity sensor relies on the fact that the relative permittivity of polyimide material changes with relative humidity and the relative permittivity of distilled water changes with temperature. During normal operation of the power system, national regulations for power capacitors generally set the ambient temperature limit at 40℃. Therefore, an environment temperature of 35℃ is assumed. At this temperature, the relative permittivity of distilled water remains constant, while the relative humidity of the environment is varied. The relative permittivity of polyimide materials is systematically increased from 2 to 4.5 with a step value of 0.1 (total 26 sets). Transmission coefficients are shown in Fig. 5 (a). It can be observed that the second resonant point almost remains unchanged, while the first resonant point experiences a red-shift with increasing relative permittivity of the polyimide material. Next, an ambient relative humidity of 68% is set and the relative permittivity of the polyimide material constant is kept. The relative permittivity of distilled water is increased from 60 to 74 with a step value of 1 (total 15 sets). The corresponding transmission coefficients are shown in Fig. 5 (b). The first resonant frequency point almost remains unchanged, while the second resonant frequency point red-shifts with the increase in the relative permittivity of distilled water. From the above results, it can be seen that the dual-channel CPNZ media sensor can effectively detect changes in temperature and relative humidity, respectively, by varying the relative permittivity of the polyimide material or distilled water. This phenomenon also corresponds to the theory, that is, two channels without significant interference.

Changing the relative permittivity of polyimide and distilled water simultaneously, we obtained a total of 26×15=390 sets of transmission coefficient data by simulation. Parts of the corresponding transmission coefficients are depicted in Fig. 6. It is shown that the resonant frequency point experiences a red-shift with an increase in the relative permittivity of the polyimide material. Similarly, the second resonant frequency point also red-shifts with an increase in the relative permittivity of the distilled water. This observation confirms that the sensor is capable of simultaneously measuring temperature and relative humidity of the environment. In conclusion, the dual-channel CPNZ media sensor demonstrates its ability to accurately measure both temperature and relative humidity when subjected to changes in both parameters. The red-shift of the resonant frequency points in Fig. 6 validates the capability of the sensor for multi-parameter measurement, making it a promising solution for environmental monitoring and other applications.

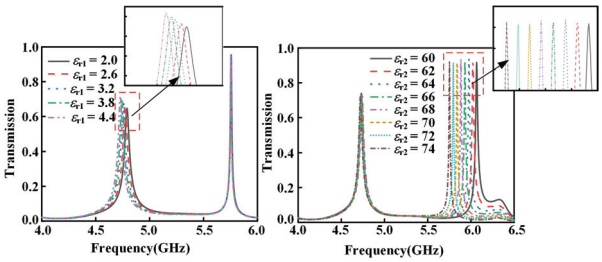

(a) (b)

Fig. 5. (a) Transmission coefficients corresponding to the relative permittivity of different polyimide materials and (b) transmission coefficients corresponding to the relative permittivity of different distilled waters.

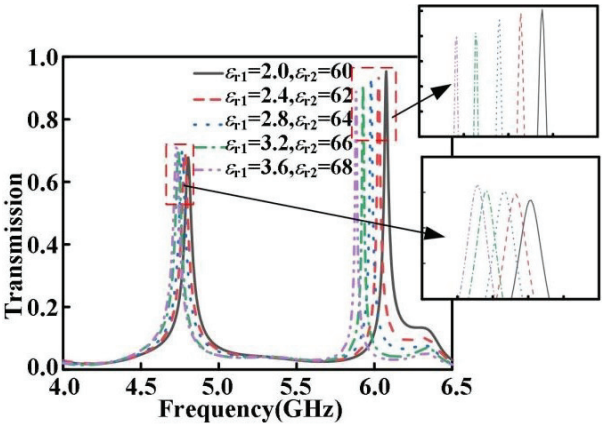

Fig. 6. Transmission coefficients corresponding to the relative permittivity of distilled water and polyimide materials.

C. Parameter inversion based on neural network

Neural networks have proven to be effective data processing tools in the microwave field due to their strong nonlinear fitting capabilities. Polyimide materials and distilled water data are obtained from the simulation of the S parameter of relative permittivity. To determine the temperature and relative humidity of the environment, an inverse problem needed to be solved. Considering the presence of multiple independent variables and dependent variables, the authors used back propagation (BP) neural networks as the data processing tool to build a multiple-input multiple-output model, thus improving the accuracy of measuring environmental temperature and relative humidity [33].

The obtained sample data were used to train the BP neural network and establish the required inversion model. The structure of the BP neural network is illustrated in Fig. 7, where the first resonant frequency f_1

and the second resonant frequency f_2 from the transmission curve serve as input data, while the output data consisted of temperature and relative humidity of the environment in which the sensor was located. By employing the BP neural network and training it with the sample data, the researchers were able to create a model that accurately predicts the environmental temperature and relative humidity based on the input resonant frequencies. The multiple-input multiple-output approach of the neural network allowed for efficient handling of the complex relationships between the input and output variables, ultimately leading to improved measurement accuracy for environmental monitoring in the microwave field.

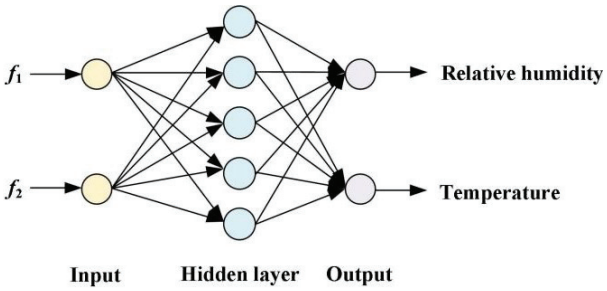

Fig. 7. Structural diagram of BP neural network.

On the basis of 390 sets of S parameters obtained by simulation of a dual-channel CPNZ media sensor, a BP neural network is used to establish the relationship between the first resonant frequency f_1, the second resonant frequency f_2, temperature and relative humidity, and inversion. The comparison between the predicted value and the expected value of the training set is shown in Fig. 8 (a). The results show that the predicted value is in great agreement with the actual value. In the figure, mean square error (MSE) represents the expected value of the squared difference between the predicted value and the actual value, and its calculation equation is:

$$MSE = \frac{1}{n}\sum_{i=1}^{n}(y_i - \hat{y}_i)^2. \tag{6}$$

The smaller the value of MSE, the better the ability of the model to fit the experimental data. Figure 8 (b) shows MSE values of different temperature and relative humidity in the training set. Results show that MSE values between the predicted value and the actual value of the BP neural network model for temperature and relative humidity are within ± 0.8. The coefficient of determination of temperature prediction model is 0.94629, and the coefficient of determination of relative humidity prediction model is 0.99711, indicating that the two prediction models have a good degree of fit.

In order to verify the accuracy of the model obtained by the BP neural network in measuring ambient temperature and relative humidity, five groups of different environmental conditions are set: relative humidity is 25% and temperature is 45℃; relative humidity is 30% and temperature is 50℃; relative humidity is 35% and temperature is 55℃; relative humidity is 40% and temperature is 60℃; and relative humidity is 45% and temperature is 65℃.

The resonant frequencies of these five groups of test data are extracted and inverted by the model. Comparison between the predicted value and the expected value and the distribution of MSE are shown in Figs. 9 (a) and (b). As can be seen from Fig. 9 (a), the predicted value is in good agreement with the expected value. It can be seen from Fig. 9 (b) that the MSE value of temperature is ± 0.15 and that of relative humidity is ± 0.1, indicating that the model obtained by using BP neural network training sample data has good measurement accuracy for ambient temperature and relative humidity.

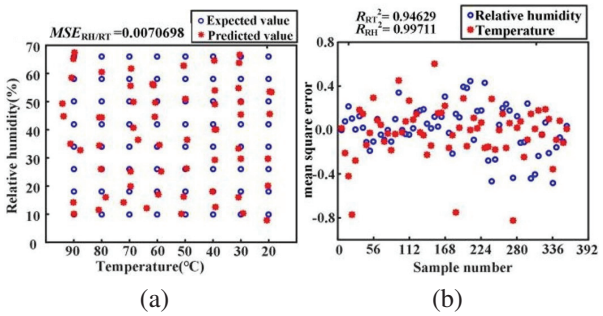

Fig. 8. (a) Comparison of predicted value and expected value of the training set and (b) MSE value of the training set.

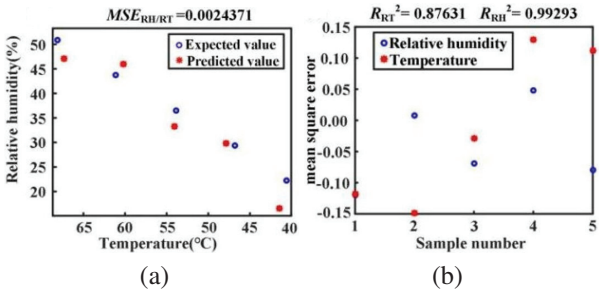

Fig. 9. (a) Comparison of predicted value and expected value of the test set and (b) MSE value of the test set.

Table 1 summarizes the performance comparison of the proposed sensor and other state-of-the-art multi-parameter measurement sensors. Multiple parameters were obtained by using two modes generated by one sensor in reference [20]. However, the two modes cannot be independently regulated.

Table 1: Performance comparison of multi-parameter measurement sensors.

Ref.	Independent	Relative Error (f_1)	Relative Error (f_2)
[20]	No	TH<4.86%	ε'<0.1% ε"<2.3%
[34]	Yes	ε'<1.5% ε"<6.67%	ε'<2.8% ε"<6.25%
[35]	Yes	μ_r<1.81%	μ_r<8%
[36]	No	ε'<10%	ε'<10%
[37]	Yes	ε'<5%	ε'<5%
[38]	Yes	T<2.33%	RH<9%
This work	Yes	T<1.3%	RH<8.74%

Thickness (TH), real part of the dielectric constant (ε'), imaginary part of the dielectric constant (ε"), relative permeability (μ_r), temperature (T), relative humidity (RH)

Sensors in references [34–38] measure different physical quantities by using multiple sensors, which leads to a large system volume and difficult integration. The operating resonant frequencies of the proposed sensor are independent of each other, and measure the temperature and relative humidity simultaneously without influencing each other. Relative errors of the predicted temperature and relative humidity are smaller than 1.3% and 8.74%, respectively.

IV. CONCLUSION

Based on theoretical analysis of double doping, this paper proposes a high precision CPNZ medium microwave sensor for multi-parameter measurement. Results show that the two-channel CPNZ media sensor does not exhibit coupling effects between the two operating frequencies. By training the BP neural network, a multi-input multi-output model is constructed to improve measurement accuracy. From the testing results of five groups of different environmental conditions, relative errors of the predicted temperature and relative humidity are smaller than 1.3% and 8.74%, respectively, indicating the sensor's high measurement accuracy and its ability to monitor changes in multiple parameters simultaneously.

ACKNOWLEDGMENT

This work is supported by the National Natural Science Foundation of China under Grant No. 61971469 and Fundamental Research Funds of Shaanxi Key Laboratory of Artificially-Structured Functional Materials and Devices (AFMD-KFJJ-21105).

REFERENCES

[1] J. Riegel, H. Neumann, and H. M. Wiedenmann, "Exhaust gas sensors for automotive emission control," *Solid State Ionics*, vol. 152, pp. 783-800, Mar. 2002.

[2] Y. Liu, Y. Yang, X. P. Lv, and L. F. Wang, "A self-learning sensor fault detection framework for industry monitoring IoT," *Math. Probl. Eng.*, vol. 2013, pp. 1-8, Jan. 2013.

[3] M. Y. Aalsalem, W. Z. Khan, W. Gharibi, M. K. Khan, and Q. Arshad, "Wireless sensor networks in oil and gas industry: Recent advances, taxonomy, requirements, and open challenges," *J. Netw. Compu. Appl.*, vol. 113, pp. 87-97, July 2018.

[4] K. Yeshwant and R. Ghaffari, "A biodegradable wireless blood-flow sensor," *Nat. Biomed. Eng*., vol. 3, no. 1, pp. 7-8, Jan. 2019.

[5] C. M. Boutry, L. Beker, Y. Kaizawa, C. Vassos, H. Tran, A. C. Hinckley, R. Pfattner, S. Niu, J. Li, J. Claverie, Z. Wang, J. Chang, P. M. Fox, and Z. Bao, "Biodegradable and flexible arterial-pulse sensor for the wireless monitoring of blood flow," *Nat. Biomed. Eng*., vol. 3, pp. 47-57, Jan. 2019.

[6] C. Weber, "Photoacoustic CO_2-sensor for automotive applications," *Procedia Engineering*, vol. 168, pp. 3-6, Sep. 2016.

[7] R. Moolat, Manoj Mani, A. P. Viswanathan, and Mohanan Pezholil, "Compact microwave sensor for monitoring aging of oil and fuel adulteration," vol. 32, no. 5, p. e23095, Jan. 2022.

[8] C. Lopatin, "Aerospace applications of optical fiber mechanical sensors," *Opto-Mechanical Fiber Optic Sensors*, pp. 237-262, Feb. 2018.

[9] X. Lv, J. Jiang, H. Wang, Q. Gao, S. Zhao, N. Li, J. Yang, S. Wang, W. Bao, and R. Chen, "Sensitivity-compensated micro-pressure flexible sensor for aerospace vehicle," *Sensors*, vol. 19, no. 1, pp. 72, Jan. 2019.

[10] A. N. S. Javanshir, "Optical temperature sensor with micro ring resonator and graphene to reach high sensitivity," *Optik*, vol. 180, pp. 442-446, Feb. 2019.

[11] F. Zhang, Y. Zang, D. Huang, C. A. Di, and D. Zhu, "Flexible and self-powered T-pressure dual-parameter sensors using microstructure-frame-supported organic thermoelectric materials," *Nat. Commun.*, vol. 6, p. 8356, Sep. 2015.

[12] J. Wu, Z. Wu, H. Xu, Q. Wu, C. Liu, B. Yang, X. Gui, X. Xie, K. Tao, Y. Shen, J. Miaod, and L. K. Norford, "An intrinsically stretchable humidity sensor based on anti-drying, self-healing and transparent organohydrogels," *Mater. Horiz.*, vol. 7, no. 7, p. 1919, July 2020.

[13] T. Li, L. Li, H. Sun, Y. Xu, X. Wang, H. Luo, Z. Liu, and T. Zhang, "Humidity sensors: Porous ionic membrane based flexible humidity sensor and its multifunctional applications," *Adv. Sci.*, vol. 4, no. 5, p. 1600404, May 2017.

[14] S. Xiao, J. Nie, R. Tan, X. Duan, J. Ma, Q. Li, and T. Wang, "Fast-response ionogel humidity sensor for real-time monitoring of breathing rate," *Mater. Chem. Front.*, vol. 3, no. 3, pp. 484-491, Mar. 2019.

[15] S. Gong, W. Schwalb, Y. Wang, Y. Chen, Y. Tang, J. Si, B. Shirinzadeh, and W. Cheng, "A wearable and highly sensitive pressure sensor with ultrathin gold nanowires," *Nat. Commun.*, vol. 5, p. 3132, Feb. 2014.

[16] S. C. B. Mannsfeld, B. C.-K. Tee, R. M. Stoltenberg, C. V. H.-H. Chen, S. Barman, B. V. O. Muir, A. N. Sokolov, C. Reese, and Z. Bao, "Highly sensitive flexible pressure sensors with microstructured rubber dielectric layers," *Nat. Mater.*, vol. 9, no. 10, pp. 859-864, Sep. 2010.

[17] E. Amin, M. Karmakar, and B. Jensen, "Fully printable chipless RFID multi-parameter sensor," *Sens. Actuat. A-Phys.*, *A. Physical*, vol. 248, pp. 223-232, Sep. 2016.

[18] L. Dong, L. F. Wang, and Q. A. Huang, "Implementation of multiparameter monitoring by an LC-type passive wireless sensor through specific winding stacked inductors," *IEEE Internet of Things J.*, vol. 2, no. 2, pp. 168-174, Apr. 2015.

[19] Z. Abbasi, P. Shariaty, M. Nosrati, Z. Hashisho, and M. Daneshmand, "Dual-band microwave circuits for selective binary gas sensing system," *IEEE T. Microw. Theory*, vol. 67, no. 10, pp. 4206-4219, Oct. 2019.

[20] L. Ali, C. Wang, F. Y. Meng, K. Adhikari, Y. Wei, J. Li, Z. Song, and M. Zhao, "Design and optimization of interdigitated microwave sensor for multidimensional sensitive characterization of solid materials," *IEEE Sens. J.*, vol. 21, no. 20, pp. 22814-22822, Oct. 2021.

[21] Y. Zhao, X. Zhao, Q. Zuo, Y. Guo, H. Huang, H. Zhang, T. Wang, N. Wen, H. Chen, T. Cong, J. Muhammad, X. Yang, X. Wang, Z. Fan, and L. Pan, "Structural engineering of hierarchical aerogels comprised of multi-dimensional gradient carbon nanoarchitectures for highly efficient microwave absorption," *Nano-Micro Lett.*, vol. 13, no. 1, p. 144, Dec. 2021.

[22] M. Saadat-Safa, V. Nayyeri, M. Khanjarian, M. Soleimani, and O. M. Ramahi, "A CSRR-based sensor for full characterization of magneto-dielectric materials," *IEEE T. Microw. Theory*, vol. 67, no. 2, pp. 806-814, Feb. 2019.

[23] N. Javanbakht, G. Xiao, and R. E. Amaya, "Portable microwave sensor based on frequency-selective surface for grain moisture content monitoring," *IEEE Sensors Letters*, vol. 5, no. 11, pp. 1-4, Nov. 2021.

[24] Y. H. Cao, K. Chen, C. Ruan, and X. Zhang, "Robust and sensitive metamaterial-inspired microfluidic sensor for liquids with low dielectric constants," *Sensor Actuat. A-Phys.*, vol. 331, p. 112869, Nov. 2021.

[25] E. Rahamim, D. Rotshild, and A. Abramovich, "Performance enhancement of reconfigurable metamaterial reflector antenna by decreasing the absorption of the reflected beam," *Appl. Sci.-Basel*, vol. 11, no. 19, p. 8999, Oct. 2021.

[26] Q. Liu, Y. F. Yu, W. S. Zhao, and H. Li, "Microfluidic T sensor based on T-dependent dielectric property of liquid," *Chinese Phys. B*, vol. 29, no. 1, p. 10701, Jan. 2020.

[27] E. M. Amin and N. C. Karmakar. "Development of a low cost printable humidity sensor for chipless RFID technology," in *2012 IEEE International Conference on RFID-TA*, pp. 165-170, Nov. 2012.

[28] H. Lobato-Morales, A. Corona-Chávez, J. L. Olvera-Cervantes, R. A. Chávez-Pérez, and J. L. Medina-Monroy, "Wireless sensing of complex dielectric permittivity of liquids based on the RFID," *IEEE T. Microw. Theory*, vol. 62, no. 9, pp. 2160-2167, Sep. 2014.

[29] A. K. Jha, N. Delmonte, A. Lamecki, M. Mrozowski, and M. Bozzi, "Novel MNZ-type microwave sensor for testing magnetodielectric materials," *Sci. Rep.*, vol. 10, no. 1, p. 16985, Oct. 2020.

[30] Z. Zhou, Y. Li, H. Li, W. Sun, I. Liberal, and N. Engheta, "Substrate-integrated photonic doping for near-zero-index devices," *Nat. Commun.*, vol. 10, no. 1, p. 4132, Sep. 2019.

[31] V. Pacheco-Peña, M. Beruete, P. Rodríguez-Ulibarri, and N. Engheta, "On the performance of an ENZ-based sensor using transmission line theory and effective medium approach," *New J. Phys.*, vol. 21, p. 043056, Apr. 2019.

[32] I. Liberal, A. M. Mahmoud, Y. Li, B. Edwards, and N. Engheta, "Photonic doping of epsilon-near-zero media," *Sci.*, vol. 355, no. 6329, pp. 1058-1062, Mar. 2017.

[33] Q. Deng. "A BP neural network optimisation method based on dynamical regularization," *Journal of Control and Decision*, vol. 6, no. 2, pp. 111-121, Jan. 2018.

[34] C. Wang, X. Liu, L. Gan, and Q. Cai, "A dual-band non-destructive dielectric measurement

sensor based on complementary split-ring resonator," *Front. Phys*., vol. 9, p. 669707, Apr. 2021.
[35] K. T. Muhammed Shafi, J. Abhishek Kumar, and M. Jaleel Akhtar, "Dual band RF sensor for testing of magnetic properties of materials using meandered line SRR," *Sens. Actuat. A*, vol. 272, pp. 170-177, Apr. 2018.
[36] W. N. Liu, J. J. Zhang, and K. M. Huang, "Dual-band microwave sensor based on planar rectangular cavity loaded with pairs of improved resonator for differential sensing applications," *IEEE T. Instrument*, vol. 70, pp. 1-8, Nov. 2021.
[37] M. A. H. Ansari, A. K. Jha, and M. J. Akhtar, "Dual band microwave sensor for dielectric characterization of dispersive materials," in *Asia-Pacific Microwave Conference IEEE*, vol. 1, pp. 1-3, Dec. 2015.
[38] F. Requena, N. Barbot, D. Kaddour, and E. Perret, "Chipless RFID temperature and humidity sensing," in *2021 IEEE MTT-S International Microwave Symposium (IMS)*, pp. 545-548, June 2021.

Qiao Yu Li is currently pursuing the doctor's degree of Electromagnetic Field and Microwave Technology in Shanghai University, Shanghai 200444, China. She received the B.S. degree in Engineering from Henan normal University, Xinxiang, China, in 2016, received the master's degree in Electromagnetic Field and Microwave Technology from Shanghai University, Shanghai 200444, China, in 2019. Her current research is focused on plasmonic sensor devices.

Yu Wei Mao received the B.S. degree from Bengbu College, Bengbu, China, in 2015, obtained the master's degree in Communication and Information Engineering at Shanghai University, Shanghai 200444, China, in 2018. Her current research is focused on near-zero medium sensor technology.

Yong Jin Zhou received the B.S. degree in communication engineering from Shandong University, Jinan, China, in 2006, and Ph.D. degree in electromagnetic field and microwave technology from Southeast University, Nanjing, China, in 2011. From 2009 to 2010, he was a visiting scholar of University of Houston. From 2011 to 2012, he was a software engineer with EEBU of Marvell Technology (Shanghai) Ltd. From 2012 to 2015, he was an Assistant Professor with School of Communication & Information Engineering, Shanghai University, Shanghai, China. From 2015, he was an Associate Professor with School of Communication & Information Engineering, Shanghai University, Shanghai, China. From 2020, he was a Professor with School of Communication & Information Engineering, Shanghai University, Shanghai, China. His current research interests include plasmonic metamaterials, millimeter wave and THz functional devices, wireless energy transmission, and computational electromagnetism. He has served as *Applied Computational Electromagnetics Society (ACES) Journal* guest editor and is serving as a Youth Editorial Board Member *Journal of Electronics & Information Technology*. He is serving as a Reviewer for over 20 peer-reviewed journals, such as *Nature Electronics, Photonic Research, Optics Letter, Optics Express, Appl. Phys. Express, IEEE Access, IEEE MTT, IEEE MWCL*. He has served as a session chair for several International Symposiums.

QPSK-modulation Wireless Transmitter Based on Time-domain Coding Metasurface

Jun Wang[1,2,3], Junfeng Li[1], Xianglin Kong[1], Xiaoyi Wang[4], and Lei Zhao[1]

[1]School of Information and Control Engineering
China University of Mining and Technology, Xuzhou 221116, China
jun-wang@cumt.edu.cn, jflimax@163.com, xlkong@cumt.edu.cn, leizhao@cumt.edu.cn

[2]Science and Technology on Antenna and Microwave Laboratory
Xidian University, Xi'an 710071, China

[3]State Key Laboratory of Millimeter Waves, School of Information Science and Engineering
Southeast University, Nanjing 211189, China

[4]College of Electronic and Information Engineering
Tongji University, Shanghai 201804, China
xiaoyiwang@tongji.edu.cn

Abstract – In this paper, a wireless communication system based on time-domain digital coding metasurface with Quadrature Phase Shift Keying (QPSK) modulation is proposed. The aperture-coupled resonant rings on the metal patches of the metasurface elements create an asymmetry along the *x*-axis, resulting in a phase difference. The Field Programmable Gate Array (FPGA) is used to change the conduction and cutoff states of pin diodes, which can control the phase responses of the metasurface elements, forming four coding states. Within a certain period, the FPGA dynamically modulates the high and low levels, thus controlling the reflection characteristics of the metasurface. When the information is converted into a binary bitstream and written into the FPGA, represented by high and low levels, the baseband signal is modulated onto the carrier by the metasurface. This system replaces the functionality of mixers in traditional wireless communication systems, further simplifying the architecture of wireless communication systems. The overall system is demonstrated by an experiment with a picture transmitted and received in real time, showing promise in future low-cost wireless communication transmission systems.

Index Terms – Metasurfaces, time-domain digital coding, wireless communication.

I. INTRODUCTION

Wireless communication technology is becoming increasingly important in today's era, and people have higher requirements for communication systems' stability, transmission rate, and latency [1]. However, the increasing number of protocols and standards has led to a surge in costs and complexity in the hardware implementation process. To meet these requirements, more advanced technologies and equipment have been applied to achieve efficient wireless communication, such as large aperture antenna arrays [2], ultra-massive Multiple-in Multiple-out (MIMO) [3], large intelligent surfaces (LIS) [4], and terahertz (THz) band [5]. However, massive MIMO requires a very large number of radio frequency (RF) chains, and the design and manufacturing of high-performance RF components working in the high-frequency band are relatively complex. The potential of LIS to significantly enhance system capacity has been widely recognized. However, the large-scale deployment of these technologies faces obstacles such as high hardware costs, substantial energy consumption, and heat dissipation issues due to the use of numerous RF chains and operating frequency bands. Moreover, traditional transceiver architectures like homodyne or heterodyne, which have been successful in mobile communication systems, encounter challenges such as high costs and limited flexibility in future wireless communication systems. Therefore, the development of new transceiver architectures that offer flexibility and efficiency for future communication systems is of utmost importance.

Reconfigurable metasurfaces have been envisioned as a promising technology to address the challenges faced in transceiver design. In the past decade, new electromagnetic phenomena have been achieved by manipulating electromagnetic waves based on reconfigurable metasurface, enabling functions such as surface

Submitted On: October 16, 2023
Accepted On: June 26, 2024

https://doi.org/10.13052/2024.ACES.J.390805

impedance, polarization conversion, frequency selective surface, and orbital angular momentum [6–12]. Moreover, the utilization of embedded tunable devices like PIN diodes and varactor diodes has been proposed in the concept of time-domain digital coding metasurface [13–14]. These devices offer the ability to dynamically reconfigure metasurface functions in real time, presenting new opportunities for tailored manipulation of electromagnetic waves. By modulating the material interface, a mapping relationship can be established between the digital bits of baseband information and the phase, amplitude, or spectral profile of the metasurface unit cell. This capability holds great potential for creating a novel signal transmission framework, where digital signals can be directly encoded onto the carrier wave incident on the metasurface. This approach simplifies the system architecture of traditional transmitters. However, direct modulation of antennas, although achieving similar functionality, is limited in real-time data transmission due to its high complexity and low efficiency [15–20].

In this paper, a wireless communication system that utilizes a time-domain digital coding metasurface is proposed. This system enables Quadrature Phase Shift Keying (QPSK) modulation of baseband signals by manipulating the phase response of the metasurface during reflection at the interface. By establishing a mapping relationship between QPSK symbols and reflection coefficients, the system achieves precise control over the modulation process. This control is conveniently achieved by changing the on/off state of the PIN diode, which alters the time-varying reflection coefficients of the metamaterial surface. Experimental results conducted at 5.5 GHz validate the system's accuracy and reliability in wireless information transmission.

II. METASURFACE UNIT CELL THEORY AND DESIGN

A. Theory analysis

A conceptual description of the time-domain digital coding metasurface for wireless communication is presented in Fig. 1. When the metasurface is driven by the monochromatic wave $E_i(t)$, which is normally incident from the left side toward the reflective metasurface at the frequency $f = f_c$, the reflective wave of the metasurface can be represented as:

$$E_r(t) = \Gamma(t) \cdot E_i(t) = \Gamma(t) \cdot e^{j2\pi f_c t}, \tag{1}$$

where $E_r(t)$ and $\Gamma(t)$ stand for the reflected waveform and the transient reflection coefficient of the metasurface, respectively. Assuming that the metasurface is varying in a scale much slower than the incident wave to safely decouple the dispersion and time-varying effects

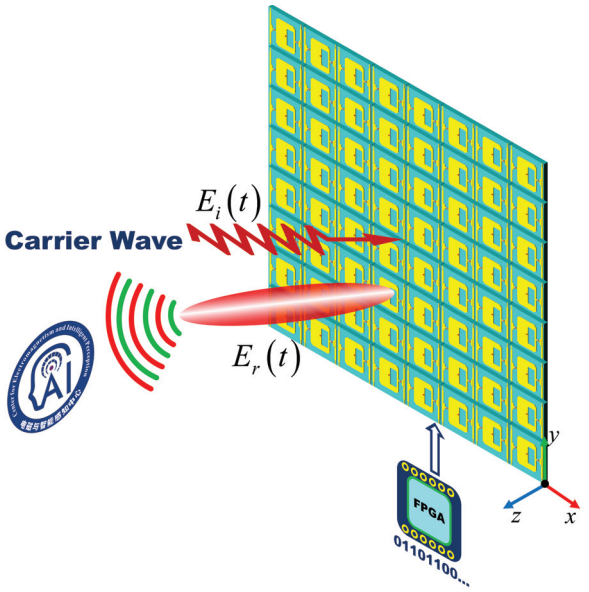

Fig. 1. Schematic diagram of wireless communication system based on reconfigurable digital coding metasurface.

of the reflective coefficient. The frequency domain of the reflective wave can be further obtained by performing Fourier transforming:

$$E_r(f) = \Gamma(f) * [\delta(f - f_c)] = \Gamma(f - f_c), \tag{2}$$

where $*$ denotes the convolution operation and $d(f)$ is the Dirac delta function. It can be seen that the reflection spectrum is highly dependent on the spectral profile of $\Gamma(f)$ from equation (2), indicating that the metasurface plays a similar role to the frequency mixer up-converting baseband signals to RF signals in the superheterodyne transceivers.

The proposed transmitter focuses on the scheme to realize the QPSK with the metasurface, using two PIN diodes to control the metasurface unit cell, achieving four encoding states. The binary data sequence of the reflection coefficient Γ_m can be represented based on different on/off states, as shown in equation (3):

$$\begin{aligned} \Gamma_0 &= \text{OFF/OFF} \Leftrightarrow' 00', \\ \Gamma_1 &= \text{ON/OFF} \Leftrightarrow' 01', \\ \Gamma_2 &= \text{OFF/ON} \Leftrightarrow' 11', \\ \Gamma_3 &= \text{ON/ON} \Leftrightarrow' 10'. \end{aligned} \tag{3}$$

By utilizing a time-domain 2-bit coding metasurface, it becomes feasible to encode each reflection coefficient Γ_m based on 2-bit binary digits.

B. Unit cell design

A 2-bit reconfigurable metasurface unit for the metasurface-based QPSK modulation is designed as

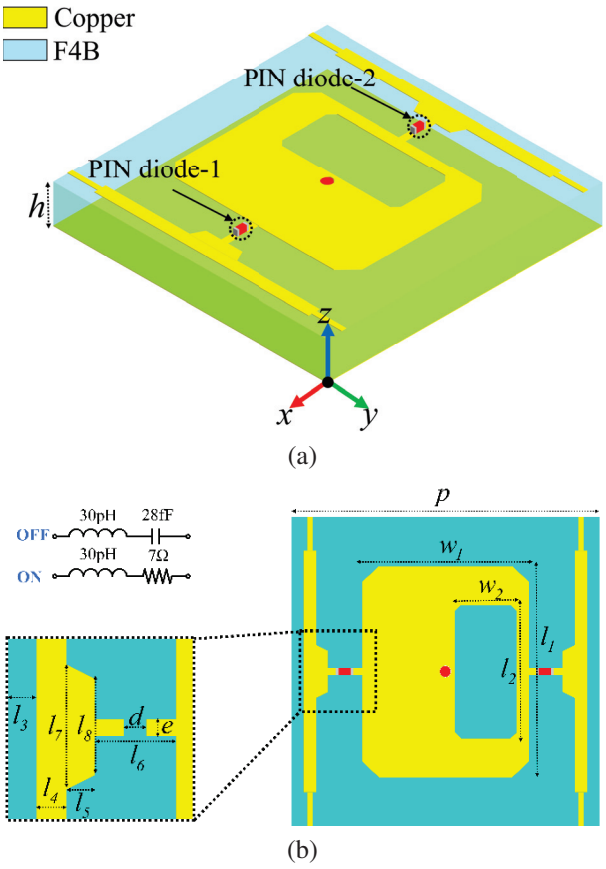

Fig. 2. (a) Structure of 2-bit metasurface unit cell and (b) top view of the metasurface unit cell with detailed parameters.

shown in Fig. 2. An aperture-coupled resonant ring is employed to create an asymmetry along the *x*-axis in the metal patches. Two PIN diodes are placed at the two sides of the patch. When the pin diodes patch switch to their ON states, a phase deviation occurs. By controlling the ON-OFF states of the pin diodes, a 90° phase is achieved in the metasurface unit response, creating four coding states for controlling the reflection characteristics of the reflective reconfigurable digital coding metasurface. These units will be used as "00", "01", "10", and "11" units for 2-bit encoding.

Figure 2 depicts the schematic diagram of the designed metasurface unit. As shown in Fig. 2 (a), the top layer of the unit consists of a square aperture resonant ring and a feeding line designed for the PIN diodes on both sides. The middle dielectric layer is made of F4B material with a dielectric constant of 2.55 and a loss tangent of 0.001. A metal via is placed in the center of the metal copper patch. By changing the voltage applied to the PIN diode loaded on the metasurface unit, different resonant states are generated when the *x*-polarized electromagnetic wave is incident on the metasurface, resulting in a change in the phase of the metasurface response. The pin diode chosen is MADP-000907-14020P by MACOM. This model of pin diode is also mentioned in [21]. The PIN diode of MADP-000907-14020P model produced by MACOM is selected for simulation and fabrication, which is conducive with a forward bias voltage, equivalent to a series lumped element with a resistance value of $R = 7\ \Omega$ and an inductance value of$L = 30$ pH, and is shut off with a reversed bias voltage, equivalent to a series lumped element with a capacitance value of $C = 28$ fF and an inductance value of$L = 30$ pH, as shown in Fig. 2 (b). The detailed structural parameters of the metasurface unit cell are listed in Table 1.

Table 1: Structure parameters of metasurface unit cell

Parameter	Length (mm)	Parameter	Length (mm)
h	2.54	14	1.2
p	27	15	1.5
wl	15	16	2.7
ll	16	17	6
w2	4	18	3
l2	9	d	0.3
l3	0.6	e	0.38

Figure 3 plots the reflection coefficients of the metasurface unit cell for *x*-polarized incident wave. As shown in Fig. 3 (a), by controlling the states of the two PIN diodes as OFF/OFF, ON/OFF, OFF/ON, and ON/ON, the resonant frequency of the unit cell increases from 5.4 GHz to 6.2 GHz while maintaining a reflection amplitude of more than 3 dB under *x*-polarized incident wave. This achieves a phase range coverage of 270° at the operating frequency of 5.5 GHz, as shown in Fig. 3 (b).

To further verify the effect of the PIN diode on the unit cell, Fig. 4 shows the surface current distribution of the unit cell in four different states of the PIN diodes at 5.5 GHz, which are labeled as states "00", "01", "10", and "11", respectively. It can be seen that when the PIN diodes are turned off, the current on the unit cell is very weak, while when the PIN diodes are turned on, the unit cell has a strong surface current, enabling the unit cell to change its resonant frequency and achieve the phase modulation. The proposed reconfigurable metasurface exhibits strong control over electromagnetic waves, making it a promising platform for dynamically manipulating the phase states.

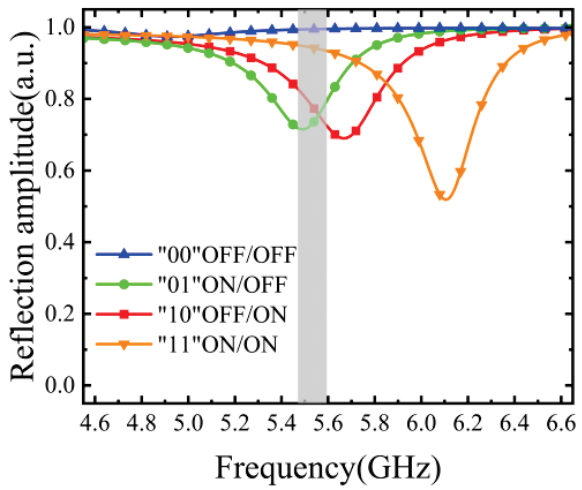

(a)

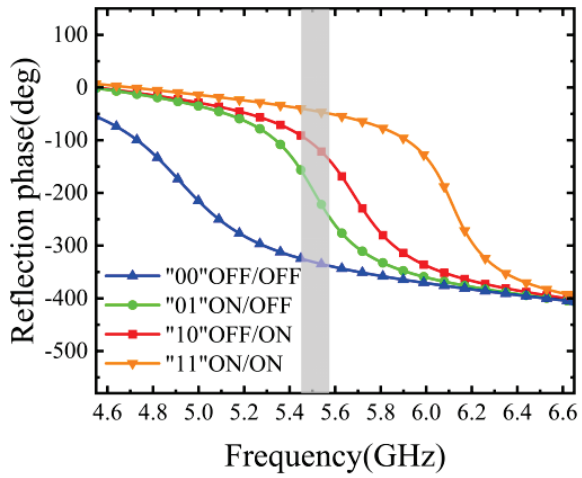

(b)

Fig. 3. Reflection coefficients of the metasurface unit cell for x-polarized incident wave: (a) amplitude response and (b) phase response.

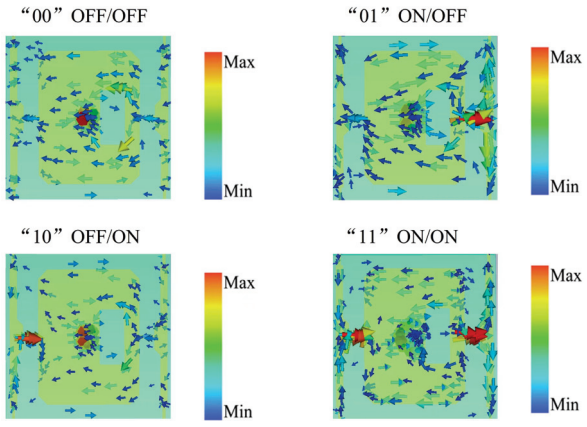

Fig. 4. Surface current distribution of the metasurface unit cell at different states.

III. EXPERIMENT OF WIRELESS COMMUNICATION SYSTEM

In order to verify the QPSK signal generated by the time-coding metasurface, a receiver using the Universal Software Radio Peripheral (USRP) is designed, which includes the following main modules, signal reception, automatic gain control, signal extraction, carrier synchronization, symbol synchronization, frame synchronization, phase offset correction, and demodulation, which are shown in Fig. 5.

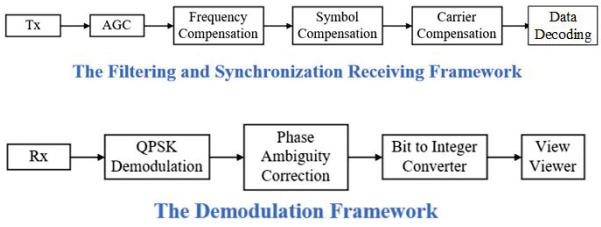

Fig. 5. QPSK receiving system model.

A metasurface-based communication system that can send and receive a picture is built. Figure 6 illustrates the entire wireless communication system, which

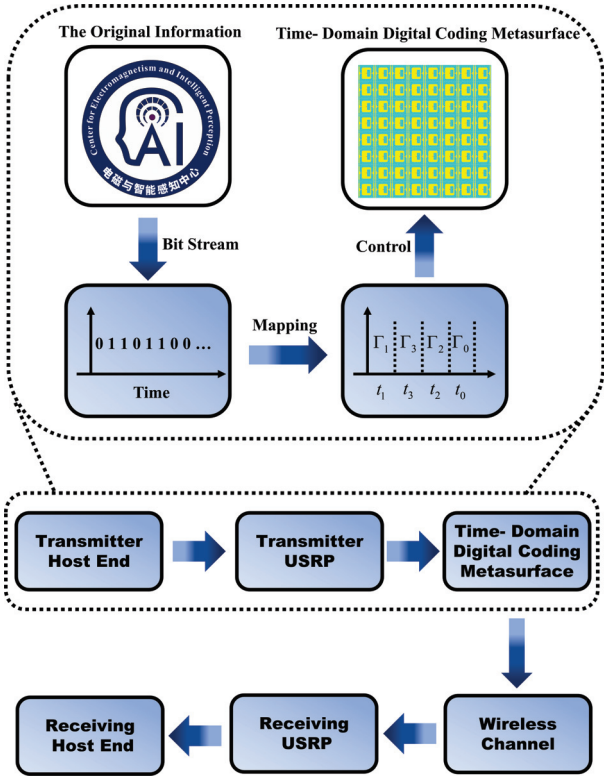

Fig. 6. Information transmission process diagram of the wireless communication system based on time-domain digital coding metasurface.

includes the transmitter consisting of the transmitter host, the transmitter-side USRP, and the time-domain digital coding metasurface and the receiver consisting of the receiver antenna, the receiver-side USRP, and the receiver host. In the transmitter, a single-tone signal is generated on the transmitter host. The picture information is firstly converted into bit stream and then mapped into QPSK modulation and finally used to control the time-domain digital coding metasurface. By adjusting the states of the PIN diodes through the modulating signal, the time-domain digital coding metasurface can modulate the carrier signal into a QPSK signal and scatter it into free space. At the receiver end, the signal is picked up by the receiving antenna and then processed by the receiving USRP and displayed on the receiver's host. In the proposed system, the time modulation period is chosen as 2.5 μs.

By extending the distance between the transmitter and receiver from 0.5 m to 1 m and increasing the data rate from 400 kbps to 800 kbps, the performance of the communication system can be evaluated under different conditions. The scatters plotted in Fig. 7 represent the constellation diagram of the received QPSK signals. As the data rate increases and the distance between the transmitter and receiver decreases, the performance of the communication improves gradually, and the scatter points of the constellation diagram converge. Additionally, the received and demodulated bitstream data at the receiver are shown in Fig. 8. To validate the proposed

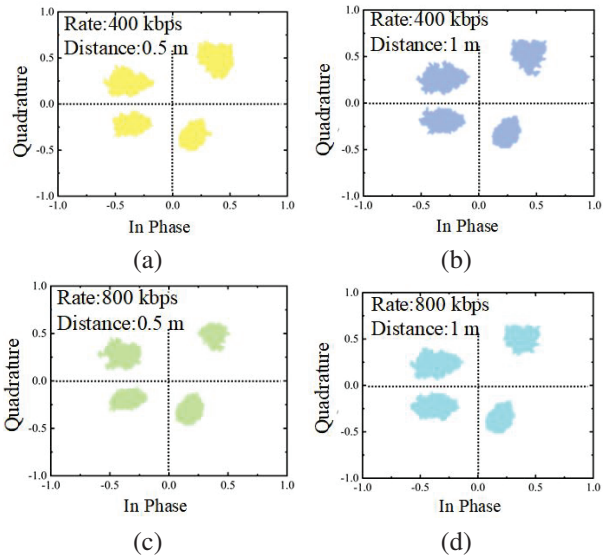

Fig. 7. Relationship between communication performance, transmission rate, and transmission distance. (a) Data rate: 400 kbps, distance: 0.5 m, (b) data rate: 400 kbps, distance: 1 m, (c) data rate: 800 kbps, distance: 0.5 m, and (d) data rate: 800 kbps, distance: 1 m.

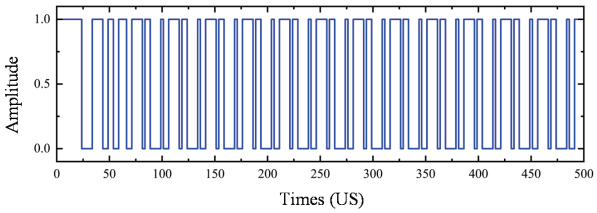

Fig. 8. Demodulated bitstream obtained.

information encoding scheme, the real-time image transmission experiments are conducted by using the time-domain digital coding metasurface wireless communication system in an indoor scenario, as shown in Fig. 9.

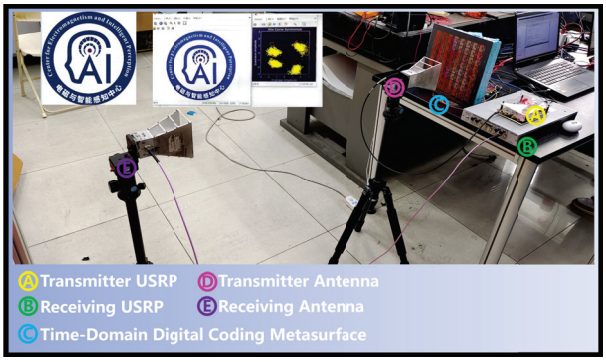

Fig. 9. Photograph of the wireless communication system based on time-domain digital coding metasurface.

The key parameters of the experiment based on time-domain digital coding metasurface are presented in Table 2. The transmitter is located on the left side of the workstation and consists of a DC power supply, Field Programmable Gate Array (FPGA), transmitter USRP, feeding antenna, and time-domain digital coding metasurface. The receiver is located on the right side of the workstation and consists of a receiving antenna, post-processing computer, and receiver USRP. The distance between the transmitter and receiver is 1 m. Experimental results show that the system performs well and may be further improved by enhancing the waveform of

Table 2: Selected key parameters of the designed wireless communication demo system based on a software-defined radio (USRP N310 & B210)

Parameter	Value
Working frequency	5.5 GHz
Modulation method	QPSK
Transmission rate	800 kbps
Frame size	960,026 samples
Bit error rate	0.01

bias voltages and optimizing the metasurface unit cell to achieve better phase responses.

IV. CONCLUSION

In this paper, an experimental verification of a QPSK wireless communication system based on time-domain digital coding metasurface is presented. The proposed system demonstrates the feasibility and effectiveness of utilizing metasurfaces for wireless communication using QPSK modulation. Compared with traditional transmitters, the phase modulation of the baseband signal is directly completed by the metasurface, which simplifies the system architecture and eliminates the need for microwave devices such as mixers. The proposed metasurface-based wireless communication system is demonstrated by a real-time image transmission experiment in an indoor environment, which may find promising applications in future low-cost wireless communication systems.

ACKNOWLEDGMENT

This work was supported in part by the National Science Foundation of China under Grant 62201575, in part by the Science and Technology on Antenna and Microwave Laboratory Foundation under Grant 6142402220310, in part by the Open Project of State Key Laboratory of Millimeter Waves under Grant K202310.

REFERENCES

[1] T. Wild, V. Braun, and H. Viswanathan, "Joint design of communication and sensing for beyond 5G and 6G systems," *IEEE Access*, vol. 9, pp. 30845-30857, Feb. 2021.

[2] E. De Carvalho, A. Ali, A. Amiri, M. Angjelichinoski, and R. W. Heath Jr., "Non-stationarities in extra-large-scale massive MIMO," *IEEE Wireless Communications*, vol. 27, no. 4, pp. 74-80, Aug. 2020.

[3] V. Jamali, A. M. Tulino, G. Fischer, R. Muller, and R. Schober, "Intelligent surface-aided transmitter architectures for millimeter-wave ultra-massive MIMO systems," *IEEE Open Journal of the Communications Society*, vol. 2, pp. 144-167, Dec. 2020.

[4] S. Hu, F. Rusek, and O. Edfors, "Beyond massive MIMO: The potential of data transmission with large intelligent surfaces," *IEEE Transactions on Signal Processing*, vol. 66, no. 10, pp. 2746-2758, May 2018.

[5] M. Alibakhshikenari, E. M. Ali, M. Soruri, M. Dalarsson, M. Naser-Moghadasi, B. S. Virdee, C. Stefanovic, A. Pietrenko-Dabrowska, S. Koziel, S. Szczepanski, and E. Limiti, "A comprehensive survey on antennas on-chip based on metamaterial, metasurface, and substrate integrated waveguide principles for millimeter-waves and terahertz integrated circuits and systems," *IEEE Access*, vol. 10, pp. 3668-3692, Jan. 2022.

[6] N. Yu, P. Genevet, M. A. Kats, F. Aieta, J.-P. Tetienne, F. Capasso, and Z. Gaburro, "Light propagation with phase discontinuities: Generalized laws of reflection and refraction," *Science*, vol. 334, no. 6054, pp. 333-337, Oct. 2011.

[7] C. Pfeiffer and A. Grbic, "Metamaterial Huygens' surfaces: Tailoring wave fronts with reflectionless sheets," *Physical Review Letters*, vol. 110, no. 19, article 197401, May 2013.

[8] F. Falcone, T. Lopetegi, M. A. G. Laso, J. D. Baena, J. Bonache, M. Beruete, R. Marqués, F. Martín, and M. Sorolla, "Babinet principle applied to the design of metasurfaces and metamaterials," *Physical Review Letters*, vol. 93, no. 19, article 197401, Nov. 2004.

[9] B. H. Fong, J. S. Colburn, J. J. Ottusch, J. L. Visher, and D. F. Sievenpiper, "Scalar and tensor holographic artificial impedance surfaces," *IEEE Transactions on Antennas and Propagation*, vol. 58, no. 10, pp. 3212-3221, Oct. 2010.

[10] Y. Kawakami, T. Hori, M. Fujimoto, R. Yamaguchi, and K. Cho, "Low-profile design of metasurface considering FSS filtering characteristics," *IEICE Transactions on Communications*, vol. 95, no. 2, pp. 477-483, Feb. 2012.

[11] E. Karimi, S. A. Schulz, I. De Leon, H. Qassim, J. Upham, and R. W. Boyd, "Generating optical orbital angular momentum at visible wavelengths using a plasmonic metasurface," *Light: Science & Applications*, vol. 3, no. 5, article e167, May 2014.

[12] F. Li, H. Chen, Q. He, Y. Zhou, L. Zhang, X. Weng, H. Lu, J. Xie, and L. Deng, "Design and implementation of metamaterial polarization converter with the reflection and transmission polarization conversion simultaneously," *Journal of Optics*, vol. 21, no. 4, article 045102, Mar. 2019.

[13] J. Y. Dai, J. Zhao, Q. Cheng, and T. J. Cui, "Independent control of harmonic amplitudes and phases via a time-domain digital coding metasurface," *Light: Science & Applications*, vol. 7, no. 1, article 90, Nov. 2018.

[14] L. Zhang, X. Q. Chen, S. Liu, Q. Zhang, J. Zhao, J. Y. Dai, G. D. Bai, X. Wan, Q. Cheng, G. Castaldi, V. Galdi, and T. J. Cui, "Space-time-coding digital metasurfaces," *Nature Communications*, vol. 9, no. 1, article 4334, Oct. 2018.

[15] S. Henthorn, K. L. Ford, and T. O'Farrell, "Bit-error-rate performance of quadrature modulation transmission using reconfigurable frequency

selective surfaces," *IEEE Antennas and Wireless Propagation Letters*, vol. 16, pp. 2038-2041, Apr. 2017.

[16] C. Liaskos, S. Nie, A. Tsioliaridou, A. Pitsillides, S. Ioannidis, and I. Akyildiz, "Realizing wireless communication through software-defined hypersurface environments," in *2018 IEEE 19th International Symposium on A World of Wireless, Mobile and Multimedia Networks (WoWMoM)*, pp. 14-15, Oct. 2018.

[17] C. Liaskos, S. Nie, A. Tsioliaridou, A. Pitsillides, S. Ioannidis, and I. Akyildiz, "A new wireless communication paradigm through software-controlled metasurfaces," *IEEE Communications Magazine*, vol. 56, no. 9, pp. 162-169, Sep. 2018.

[18] Y. Wang and A. Tennant, "Experimental time-modulated reflector array," *IEEE Transactions on Antennas and Propagation*, vol. 62, no. 12, pp. 6533-6536, Dec. 2014.

[19] X. Wang and C. Caloz, "Spread-spectrum selective camouflaging based on time-modulated metasurface," *IEEE Transactions on Antennas and Propagation*, vol. 69, no. 1, pp. 286-295, Jan. 2020.

[20] X. Wang and G. M. Yang, "Time-coding spread-spectrum reconfigurable intelligent surface for secure wireless communication: Theory and experiment," *Optics Express*, vol. 29, no. 20, pp. 32031-32041, Sep. 2021.

[21] Z. Qin, Y. F. Li, H. Wang, W. P. Wan, C. C. Li, Z. B. Zhu, Y. Cheng, S. Y. Li, H. Y. Chen, J. F. Wang, and S. B. Qu, "Polarization meta-converter for dynamic polarization states shifting with broadband characteristic," *Optics Express*, vol. 30, no. 11, pp. 20014-20025, May 2022.

Jun Wang was born in Jiangsu, China. He received the B.Eng. and M.S. degrees from Jiangsu Normal University, Xuzhou, China, in 2013 and 2017, respectively, and the Ph.D. degree in electromagnetic field and microwave technology from Southeast University, Nanjing, in 2021. From 2015 to 2016, he was with the Department of Electronic and Electrical Engineering, Nanyang Technological University of Singapore, as a Research Associate.

He joined the China University of Mining and Technology, Xuzhou, China, in 2021. He has authored or co-authored over 30 referred journal and conference papers. His current research interests include the design of RF/microwave antennas and components.

Junfeng Li was born in 1998 in Chongqing, China. He is currently pursuing a master's degree at the China University of Mining and Technology, Xuzhou, China.

His research direction is metasurface communication and software-defined radio.

Xianglin Kong (Member, IEEE) was born in Shandong, China, in 1995. He received the M.S. degree in information and communication engineering from China University of Mining and Technology (CUMT), Xuzhou, China, in 2021. He is currently pursuing the Ph.D. degree in information and communication engineering at CUMT, Xuzhou, China.

His research interests include microwave absorber, frequency selected surface, and vortex metasurface.

Xiaoyi Wang (Member, IEEE) received the B.S. degree in electronic science and technology from the University of Electronic Science and Technology of China (UESTC), Chengdu, China, in 2011, the M.S. degree in communication and information system from Fudan University, Shanghai, China, in 2014, and the Ph.D. degree in electrical engineering from Polytechnique Montréal, Montréal, QC, Canada, in 2020. He is currently a Research Professor with Tongji University, Shanghai. His research interests include all fields of theoretical, computational, and applied electromagnetics, with a strong emphasis on metamaterials and metasurfaces. Dr. Wang was a recipient of the Student Paper Competition Award of the IEEE International Symposium on Antennas and Propagation (AP-S) in 2019 and the International Union of Radio Science (URSI) Young Scientist Award in 2020.

Lei Zhao received the B.S. degree in mathematics from Jiangsu Normal University, China, in 1997, and the M.S. degree in computational mathematics and the Ph.D. degree in electromagnetic fields and microwave technology from Southeast University, Nanjing, China, in 2004 and 2007, respectively.

He joined the China University of Mining and Technology, Xuzhou, China, in 2019, where he is currently a Full Professor. From September 2009 to December 2018, he worked with Jiangsu Normal University, Xuzhou, China. From August 2007 to August 2009, he worked with the Department of Electronic Engineering, The Chinese University of Hong Kong, as a Research Associate. From February 2011 to April 2011, he worked with the Department of Electrical and Computer Engineering, National University of Singapore, as a Research Fellow. From September 2016 to September 2017, he worked with the Department of Electrical and Computer Engineering, University of Illinois at Urbana-Champaign, Champaign, IL, USA, as a Visiting Scholar. He has authored or coauthored more than 100 refereed journal and conference papers. His current research interests include spoof surface plasmon polaritons theory and its applications, RF/microwave antenna and filter design, computational electromagnetics, and electromagnetic radiation to human's body.

Dr. Zhao serves as an Associate Editor for *IEEE Access*, an Associate Editor-in-Chief for *Applied Computational Electromagnetics Society (ACES) Journal* and a reviewer for multiple journals and conferences including the *IEEE Trans. on Microwave Theory and Techniques, IEEE Trans. Antennas and Propagation, IEEE Antennas and Wireless Propagation Letters, Applied Computational Electromagnetics Society (ACES) Journal*, and other primary electromagnetics and microwave related journals.

Optimization of Multilayer Microwave Absorbers using Multi-strategy Improved Gold Rush Optimizer

Yi Ming Zong[1], Wei Bin Kong[1], Jia Pan Li[2], Lei Wang[1], Hao Nan Zhang[1], Feng Zhou[1], and Zi Yao Cheng[1]

[1]College of Information Engineering
Yancheng Optical Fiber Sensing and Application Engineering Technology Research Center,
Yancheng Institute of Technology, Jiangsu Yancheng 224051, China
949650915@qq.com, kongweibin@ycit.cn, wanglei0324@ycit.edu.cn,
zhanghn0628@163.com, zfycit@163.com, chengziyao041017@163.com

[2]School of Information Science and Engineering
Southeast University, Jiangsu Nanjing 211189s, China
2106815946@qq.com

Abstract – In this study, a multi-strategy improved gold rush optimizer (MIGRO) is proposed for the design of multilayer broadband microwave absorbers (for normal incidence). The purpose of this optimization process is to minimize the maximum reflection coefficient of the absorber by selecting appropriate material layers from existing literature databases within the desired frequency range. To enhance the performance of a gold rush optimizer (GRO), three improvement strategies are proposed. This paper demonstrates the effectiveness of the improved strategy and the superior reflection coefficient of the MIGRO compared to other heuristic algorithms used for the design of microwave absorbers through two different simulation examples.

Index Terms – Absorbing material, gold rush optimizer, multilayer microwave absorber, reflection coefficient.

I. INTRODUCTION

Microwave absorbing materials are widely applied in fields such as aerospace, construction, and healthcare [1–4]. These materials interact with electromagnetic waves through various mechanisms, including reflection, absorption, transmission, and secondary reflection. By converting electromagnetic energy into thermal energy or other forms of energy, these materials attenuate and absorb electromagnetic waves, thereby reducing their reflection and transmission [5]. With the increasingly complex electromagnetic environment, there is a growing demand for lightweight, high-performance microwave absorbing materials. However, absorbers composed of a single absorbing material have limitations, including narrow absorption bandwidth, lower absorption efficiency, and larger size and weight. In contrast, multilayer structured absorbing materials offer design flexibility and the ability to compensate for these material defects [6].

In the case of normal incidence, the reflection coefficient of multilayer microwave absorbers depends on various factors such as the frequency of the electromagnetic waves, the electromagnetic parameters, and thickness of each layer of materials. Determining the type of material and adjusting its thickness to reduce the reflection coefficient within the desired frequency range can be considered as an optimization challenge.

Michielssen et al. proposed a physical model for multilayer microwave absorber structures. They provided a set of predefined materials with frequency-dependent electrical permittivity and magnetic permeability, and utilized a genetic algorithm (GA) to determine the optimal material selection and thickness for each layer [7]. Subsequently, various heuristic algorithms have been introduced and successfully applied in designing multilayer microwave absorbers, such as particle swarm optimization (PSO) and its derivatives [8, 9], differential evolution (DE) [10, 11], central force optimization (CFO) [12], a hybrid algorithm of binary lightning search algorithm and simulated annealing (BLSA-SA) [13], and bald eagle search optimization algorithm (BESOA) [14]. A comparative analysis of particle swarm optimization (PSO), bat algorithm (BAT), and cuckoo search algorithm (CSA) was conducted in [15]. With the emergence of new heuristic algorithms, there is still room for further optimization of multilayer microwave absorbers.

In this study, a multi-strategy improved gold rush optimizer (MIGRO) which determines the optimal layer sequence and corresponding thicknesses for the

Submitted On: April 29, 2024
Accepted On: October 2, 2024

https://doi.org/10.13052/2024.ACES.J.390806

multilayer microwave absorbers design is proposed. To enhance the convergence speed and global search capability of MIGRO, three improvement strategies were introduced, including quasi-reverse learning, sigmoid convergence weight, and golden sine algorithm. Through two design examples, it was demonstrated that, compared to other heuristic algorithms, MIGRO generated superior reflection coefficients when designing multilayer microwave absorbers.

II. PHYSICAL MODEL OF MULTILAYER ABSORBER

The physical model of a multilayer microwave absorber is shown in Fig. 1, where a uniform plane wave is incident normally on the surface of the absorber. The absorber consists of N planar layers and is supported by a perfect electric conductor (PEC). Each layer in the absorber varies in thickness and possesses magnetic/electrical properties that are dependent on frequency. The thickness of each layer is represented by d_i, while the dielectric constant and magnetic permeability are denoted as ε_i and μ_i, respectively. By applying the equivalent transmission line theory of electromagnetic waves, the structure can be represented as a circuit model consisting of cascaded N segment uniform transmission lines [16], as shown in Fig. 2.

The electromagnetic wave absorption performance of multilayer absorbers is evaluated by calculating the return loss value, expressed as equation (1), and used as the objective function for optimization:

$$F_{obj} = 20\log_{10}(\max|R|). \tag{1}$$

The reflection coefficient at the interface between free space and the medium is denoted as R, and can be formulated as:

$$R = \frac{Z_1 - \eta_0}{Z_1 + \eta_0}, \tag{2}$$

where η_0 is the intrinsic impedance of free space. The total impedance of the absorber is denoted as Z_1. In the case of normal incidence, the input impedance Z_i of the $i-th$ layer is described as follows:

$$Z_{\mathrm{i}} = \eta_{\mathrm{i}} \frac{Z_{\mathrm{i+1}} + j\eta_{\mathrm{i}}\tan(\beta_i d_i)}{\eta_{\mathrm{i}} + jZ_{\mathrm{i+1}}\tan(\beta_i d_i)}, i < N. \tag{3}$$

The input impedance of the $N-th$ layer can be considered as the input impedance of the transmission line with a terminal short circuit, which is expressed as follows:

$$Z_{\mathrm{i}} = j\eta_{\mathrm{i}}\tan(\beta_i d_i), i = N, \tag{4}$$

where β_i, d_i, and η_i are the phase constant, thickness, and wave impedance of the $i-th$ layer, respectively. η_i and β_i are defined as follows:

$$\eta_i = \sqrt{\frac{\mu_i}{\varepsilon_i}}, \tag{5}$$

$$\beta_i = \frac{2\pi f}{c}\sqrt{\mu_{r,i}\varepsilon_{r,i}}, \tag{6}$$

where μ_i and ε_i are the magnetic permeability and dielectric constant of the material, $\mu_{r,i}$ and $\varepsilon_{r,i}$ are the relative magnetic permeability and relative dielectric constant of the material, f is the frequency, and c is the speed of light.

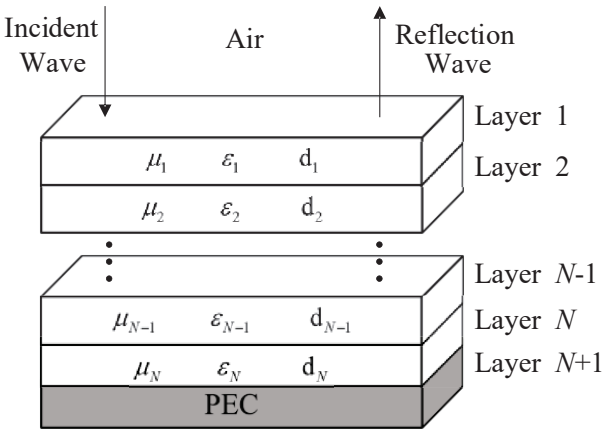

Fig. 1. Physical model of multilayer microwave absorber.

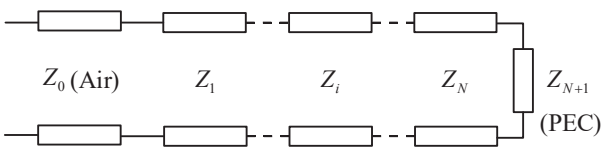

Fig. 2. Equivalent circuit of multilayer microwave absorber.

III. GOLD RUSH OPTIMZER

A. Basic gold rush optimizer

A gold rush optimizer (GRO) is a metaheuristic algorithm based on population that incorporates three fundamental principles of gold exploration: migration, panning, and collaboration [17]. It has been successfully applied to engineering optimization problems [18, 19].

(1) Migration of prospectors

The mathematical expressions for simulating the process of gold prospectors approaching the gold mine are as follows:

$$D_1 = C_1 \cdot X^{best}(t) - X_i(t), \tag{7}$$

$$X_{new,i}(t+1) = X_i(t) + A_1 \cdot D_1, \tag{8}$$

where X^{best}, X_i, and t represent the values of the optimal solution, the current solution i, and the number of iterations, respectively. $X_{new,i}$ denotes the new position of feasible solutions, and the expressions for A_1 and C_1 are as follows:

$$A_1 = 1 + l_1\left(k_1 - \frac{1}{2}\right), \tag{9}$$

$$C_1 = 2k_2, \tag{10}$$

where k_1 and k_2 are uniformly distributed random numbers in the range [0, 1]. l_1 is the convergence factor, defined as follows:

$$l_1 = 2 + \left(\frac{1-t}{t_{\max}-1}\right)\left(2 - \frac{1}{t_{\max}}\right). \tag{11}$$

(2) Gold mining

In pursuit of the golden dream, gold prospectors continuously adjust their positions to obtain more gold, and the expression of the gold mining process is as follows:

$$D_2 = X_i(t) - X_r(t), \tag{12}$$

$$X_{new,i}(t+1) = X_r(t) + A_2 \cdot D_2, \tag{13}$$

where X_r represents the position of the gold prospector r randomly selected from the feasible solution space, and A_2 is the vector coefficient, as shown in the following equation:

$$A_2 = l_2(2k_1 - 1), \tag{14}$$

where l_2 is defined as follows:

$$l_2 = \left(\frac{t_{\max}-t}{t_{\max}-1}\right)^2 \left(2 - \frac{1}{t_{\max}}\right) + \frac{1}{t_{\max}}. \tag{15}$$

(3) Collaboration

At times, gold prospectors may collaborate with each other to increase the probability of discovering gold, and this collaborative behavior can be represented by the following equation:

$$D_3 = X_{g2}(t) - X_{g1}(t), \tag{16}$$

$$X_{new,i}(t+1) = X_i(t) + k_1 \cdot D_3, \tag{17}$$

where X_{g1} and X_{g2} are two prospectors randomly selected from the expected gold-seeking region, and D_3 is the collaboration vector.

B. Improved gold rush optimizer

A high-quality initial population can improve the solution accuracy and convergence speed of the algorithm. However, the basic GRO employs a random initialization method, which does not guarantee diversity within the initial population. Therefore, the quasi-reverse learning is utilized for the population initialization of GRO. Previous studies have already demonstrated that the utilization of quasi-reverse numbers has been found to be more effective in locating the global optimal solution compared to the use of opposite numbers [20].

Assuming that the value of the $i-th$ gold prospector is represented as X_i, where ub_i is the upper bound of the independent variable X_i and lb_i is the lower bound of the independent variable X_i. The corresponding opposite point X_i^o and quasi-reverse point X_i^{qo} are shown as follows:

$$X_i^o = lb_i + ub_i - X_i, \tag{18}$$

$$X_i^{qo} = \frac{lb_i + ub_i}{2} + \left|X_i^o - \frac{lb_i + ub_i}{2}\right| \cdot rand(0,1). \tag{19}$$

The GRO employs linear inertia weights, with the value of l_1 decreasing linearly from 2 to 0 as the number of iterations increases. Although this linear inertia weight can partially balance global and local search efforts, the actual search process is highly complex and nonlinear. Consequently, linear weights may diminish the optimization performance of the algorithm.

In this study, MIGRO utilizes the sigmoid function as the nonlinear convergence factor S, replacing the original convergence factor l_1. The value of S nonlinearly decreases from approximately 2 to nearly 0, as illustrated in Fig. 3, with its corresponding expression defined as follows:

$$S = \frac{2}{\left(1 + \exp\left(\frac{10t}{t_{\max}} - 5\right)\right)}. \tag{20}$$

The sigmoid function is a nonlinear convergence factor that effectively balances global and local search. It improves the accuracy of population optimization and accelerates optimization speed [21].

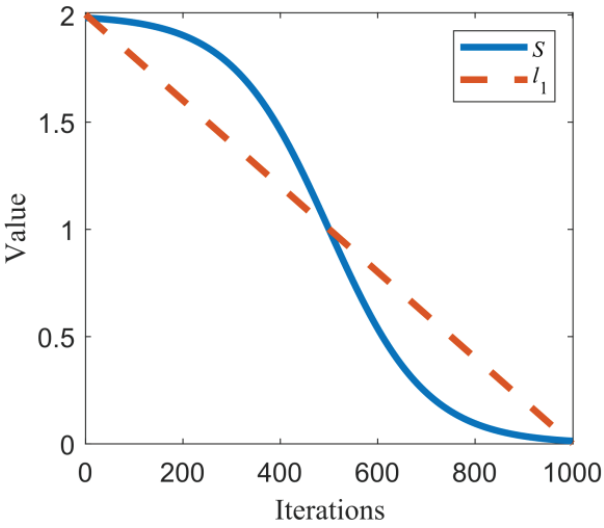

Fig. 3. Graph for values of S during algorithm iteration.

The golden sine algorithm is inspired by the sine function and the golden ratio, where individuals explore the search space based on the golden ratio for approximate optimal solutions. By combining the sine function and the golden ratio, the algorithm can quickly locate the region where the optimal value lies and escape local optima. As a result, the algorithm's performance is improved [22].

Building upon the gold mining and cooperation stages of the GRO, this paper enhances the migration stage of prospectors by incorporating the golden sine algorithm. The position update formula for this process, after integrating the golden sine algorithm, can be

expressed as follows:

$$X_{new,i}(t+1) = X_i(t) \cdot |\sin(R_1)| + R_2 \cdot \sin(R_1) \cdot D^*, \quad (21)$$

$$D^* = d_1 \cdot X^*(t) - d_2 \cdot X_i(t), \quad (22)$$

where R_1 is a random number in the range $[0, 2\pi]$, R_2 is a random number between $[0, \pi]$. d_1 and d_2 are coefficient factors, which can be obtained from the following equation:

$$d_1 = a \cdot \tau + b \cdot (1 - \tau), \quad (23)$$

$$d_2 = a \cdot (1 - \tau) + b \cdot \tau, \quad (24)$$

where a and b are the search interval, which are $-\pi$ and π. τ denotes the golden ratio, which is $(\sqrt{5}-1)/2$.

The flow chart of MIGRO is shown in Fig. 4.

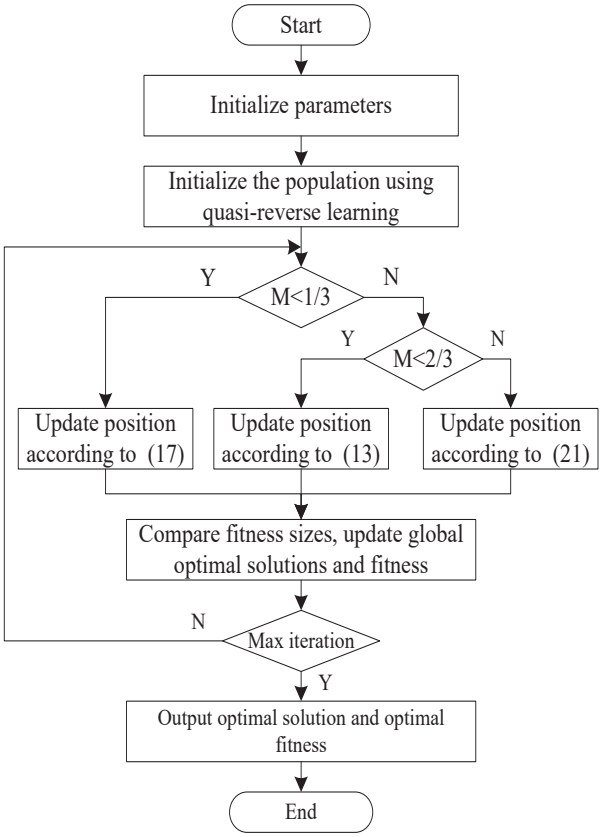

Fig. 4. Flow chart of MIGRO.

IV. SIMULATION EXPERIMENT AND RESULT ANALYSIS

A. Simulation process

In this simulation experiment, the reflection coefficient of the multilayer absorber physical model is determined by the electromagnetic parameters of each layer material, layer thickness, layer arrangement order, and the incident frequency of electromagnetic waves. During the initialization phase, the thickness and material of each layer are randomly assigned, with constraints on the number of layers, maximum thickness, and bandwidth. As a result, the number of variables is twice the number of layers. The purpose of optimization is to determine the thickness and type of materials for each layer in order to reduce the maximum reflection coefficient.

This database consists of 16 materials, which are categorized into four groups: lossless dielectric materials, lossy magnetic materials, lossy dielectric materials, and relaxation magnetic materials. The relative dielectric constant and magnetic permeability of these materials are summarized in Table 1. These materials are

Table 1: Database of absorbing materials

Lossless dielectric materials ($\mu'=1, \mu''=0$)				
#	ε'			
1	10			
2	50			
Lossy magnetic materials ($\varepsilon'=15, \varepsilon''=0$)				
$\mu = \mu' - j\mu''$ $\quad \mu' = \frac{\mu'(1GHz)}{f^a}$ $\quad \mu'' = \frac{\mu''(1GHz)}{f^b}$				
#	$\mu'(1GHz)$	a	$\mu''(1GHz)$	b
3	5	0.974	10	0.961
4	3	1.000	15	0.957
5	7	1.000	12	1.000
Lossy dielectric materials ($\mu'=1, \mu''=0$)				
$\varepsilon = \varepsilon' - j\varepsilon''$ $\quad \varepsilon' = \frac{\varepsilon'(1GHz)}{f^a}$ $\quad \varepsilon'' = \frac{\varepsilon''(1GHz)}{f^b}$				
#	$\varepsilon'(1GHz)$	a	$\varepsilon''(1GHz)$	b
6	5	0.861	8	0.569
7	8	0.778	10	0.682
8	10	0.778	16	0.861
Relaxation-type magnetic materials ($\varepsilon'=15, \varepsilon''=0$)				
$\mu = \mu' - j\mu''$ $\quad \mu'(f) = \frac{\mu_m f_m^2}{f^2 + f_m^2}$ $\quad \mu''(f) = \frac{\mu_m f_m f}{f^2 + f_m^2}$				
f and f_m in GHz				
#	μ_m	f_m		
9	35	0.8		
10	35	0.5		
11	30	1.0		
12	18	0.5		
13	20	1.5		
14	30	2.5		
15	30	2.0		
16	25	3.5		

pre-defined and also used in [7–15]. The selection of these materials is made in order to maintain consistency in the comparison.

The mathematical modeling and optimization process of multilayer microwave absorbers was implemented using MATLAB R2022A software. CST Studio Suite is a powerful 3D electromagnetic field simulation software. The optimal material types and layer thickness obtained through numerical calculations will be imported into CST for electromagnetic simulation, ensuring the accuracy of the optimization results.

B. Results and analysis

This section introduces two design examples to demonstrate the advantages of MIGRO in designing multilayer microwave absorbers. The results obtained from the MIGRO and the basic GRO are compared with those of other heuristic algorithms published in the literature.

(1) First example: 5-layer absorber

This 5-layer absorber is designed to operate within the frequency range 2-8 GHz, with a frequency step of 0.1 GHz and a total thickness constraint of 5 mm. For this experiment, the population size for both MIGRO and GRO is set to 50, with a maximum iteration limit of 1000 iterations. Each algorithm is independently run 20 times. The optimization results obtained from the BESOA [14], BLSA-SA [13], and CFO [12] methods are compared with the results of the present experiment, as shown in Table 2.

MIGRO achieves the best maximum reflection coefficient within the frequency range 2-8 GHz, while also maintaining the lowest average reflection coefficient. The corresponding reflection coefficients are shown in Fig. 5, with MIGRO reaching a peak of −33.2748 dB at 2.4 GHz. Figure 6 displays the convergence curves of MIGRO and GRO.

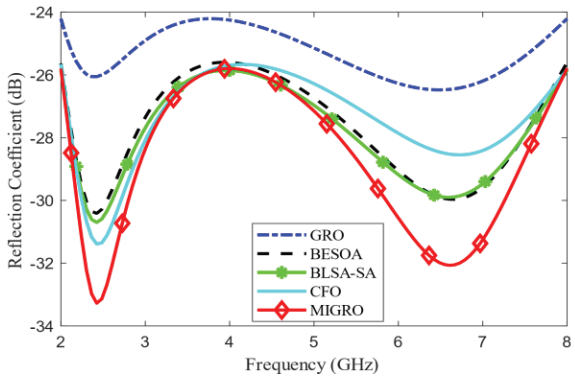

Fig. 5. Comparison of reflection coefficients for 5-layer designs in the 2-8 GHz.

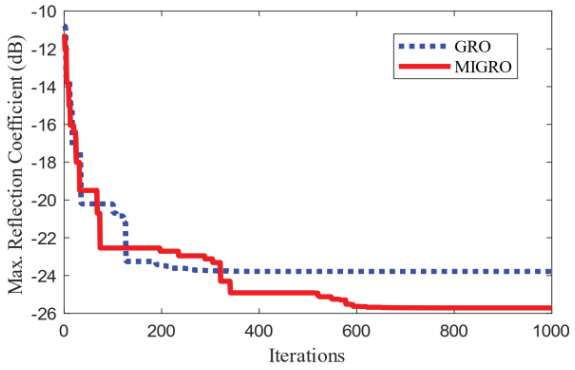

Fig. 6. Comparison of convergence curves for 5-layer designs over 1000 iterations.

MIGRO demonstrates higher convergence accuracy in the later stages than GRO, indicating that the improved strategies of the algorithm effectively prevent MIGRO from getting trapped in local optima.

Table 2: The best optimization results of 5-layer microwave absorber

Algorithm	**MIGRO**		**GRO**		**BESOA** [14]		**BLSA-SA** [13]		**CFO** [12]	
Layers	**Type and Thickness**									
1	16	0.3771	16	0.4097	16	0.41701	16	0.3682	16	0.377
2	6	0.8308	6	1.0306	6	1.10903	6	1.9580	6	1.572
3	6	1.3524	6	1.2394	6	1.78825	6	1.1016	6	0.991
4	6	1.0659	11	0.8852	3	0.21456	14	0.4834	6	0.377
5	14	1.3550	13	1.0732	15	1.27113	15	0.9424	15	1.425
Total thickness (mm)	4.9812		4.6381		4.79998		4.8536		4.744	
Max. reflection coefficient (dB)	−25.8852		−24.2055		−25.765		−25.8528		−25.698	
Avg. reflection coefficient (dB)	−28.7024		−25.3212		−27.7014		−27.8752		−27.4246	

(2) Second example: 7-layer absorber

In this instance, the 7-layer absorber was optimized with a maximum total thickness constraint of 10 mm. To investigate the optimization results across a broader frequency range, the absorption bandwidth was extended to 0.1-20 GHz. The remaining experimental parameters remain consistent with the initial example.

The design results of MIGRO were compared with the results of BLSA-SA [14], CAS [15], and DE [11]. As shown in Table 3, the maximum reflection coefficients of MIGRO, GRO, [14], [15], and [11] are −18.3183, −18.0175, −18.0406, −18.0879, and −17.9 dB, respectively. MIGRO exhibits the lowest maximum reflection coefficient. Additionally, MIGRO also has the lowest average reflection coefficient of −19.6811 dB. In Fig. 7, the reflection coefficients in the frequency range 0.1-20 GHz are calculated using five intelligent algorithms. From Fig. 8, it can be seen that, compared to GRO, MIGRO exhibits higher convergence accuracy in iterations.

C. Verify simulation results with CST

Computer Simulation Technology (CST) Microwave Studio Suite (MWS) is a commonly utilized electromagnetic simulation software that has been employed to validate the efficacy of numerous multilayer microwave absorbers designs [23, 24]. For this research, all simulations were carried out using the Finite Element Method (FEM) and Frequency Domain Solver (FDS) modules within CST.

Materials 3 to 16 from Table 1 were imported into the CST material library. To incorporate the material property parameters provided externally, CST Studio utilized fitting techniques internally to store the provided data. The fitting error between the original provided data and the fitted data will result in deviations between

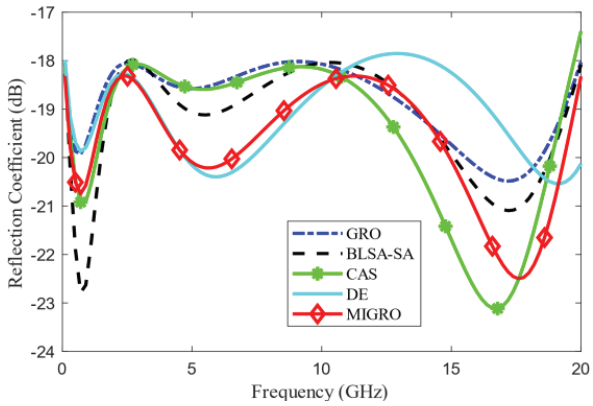

Fig. 7. Comparison of reflection coefficients for 7-layer designs in the 0.1-20 GHz range.

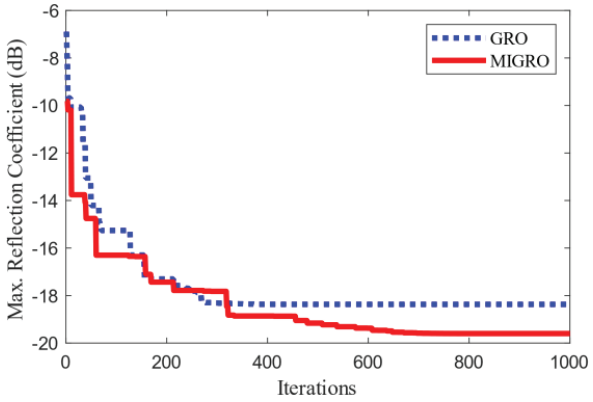

Fig. 8. Comparison of convergence curves for 7-layer designs over 1000 iterations.

Table 3: The best optimization results of 7-layer microwave absorber

Algorithm	**MIGRO**		**GRO**		**BLSA-SA** [14]		**CAS** [15]		**DE** [11]	
Layers	**Type and Thickness**									
1	16	0.2131	16	0.2114	16	0.2080	16	0.2107	14	0.2064
2	6	2.0127	6	1.7644	6	1.7490	6	1.1066	6	1.8762
3	14	0.5994	14	0.5457	16	0.0850	6	0.7916	16	0.5391
4	6	0.9139	3	1.9669	6	0.0820	14	0.5482	6	0.9499
5	5	1.6448	6	2.2745	14	0.4922	5	1.3785	5	1.9596
6	4	0.6706	4	1.6528	5	1.5020	6	0.5570	4	0.7817
7	5	0.9627	6	0.2784	4	1.6602	4	1.7450	5	0.4864
Total thickness (mm)	7.0172		8.6941		5.7784		6.3376		6.7993	
Max. reflection coefficient (dB)	−18.3183		−18.0175		−18.0406		−18.0879		−17.9	
Avg. reflection coefficient (dB)	−19.6811		−18.8682		−19.2074		−19.5157		−19.1169	

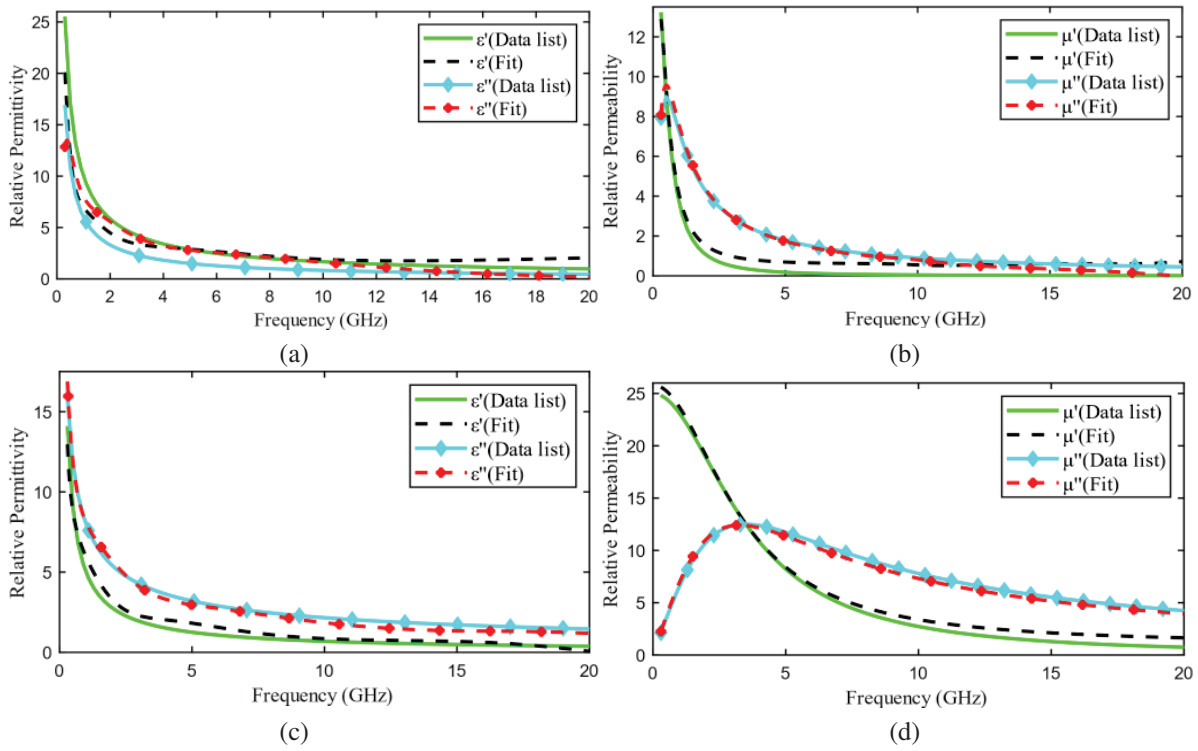

Fig. 9. Comparison of supplied and fitted material dispersion curves in CST: (a) Material 8, (b) Material 12, (c) Material 6, and (d) Material 16.

the simulated results in CST and the calculated results [25]. Among all these materials, Materials 8 and 12 exhibit relatively large fitting errors. For comparison, Figs. 9 (a)-(d) illustrate the fitting data for Materials 8, 12, 6, and 16, respectively.

Using the 5-layer optimal design as an example, a multilayer microwave absorber model is constructed in CST where the material type and thickness of each layer align with the MIGRO data presented in Table 2. The absorber structure is simulated as an infinite periodic repetition (unit cell) along the x and y axes. Two Floquet ports are defined at both the maximum (Z_{max}) and minimum (Z_{min}) of the $z-axis$, with a plane wave incidence angle set to 0 degrees and a frequency range 2-8 GHz, feasibly generating the plane wave model, as illustrated in Fig. 10.

In the CST simulation results, the reflection coefficient curves for the 5-layer and 7-layer optimized designs are shown in Figs. 11 (a)-(b). The numerical calculation results and the electromagnetic simulation results exhibit no significant discrepancies, thereby

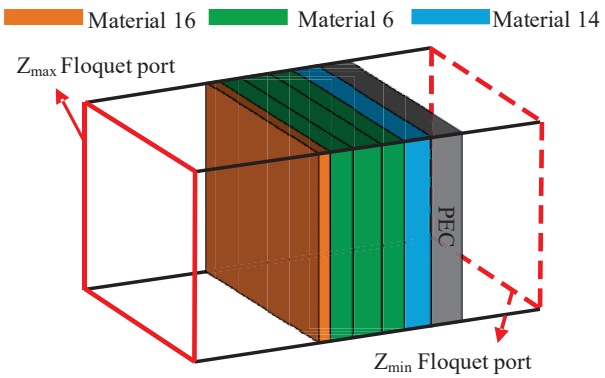

Fig. 10. Model of the 5-layer absorber and the two Floquet ports used to excite the plane waves.

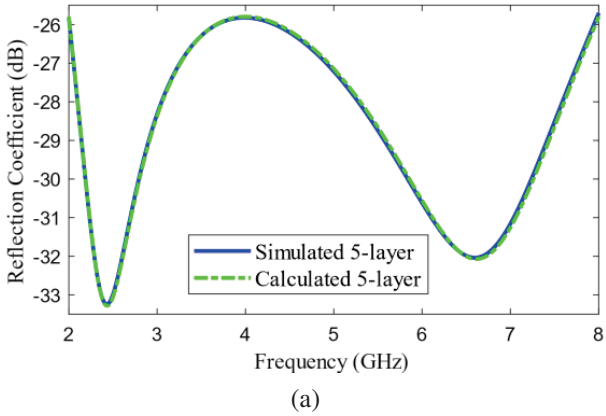

Fig. 11. *Continued*

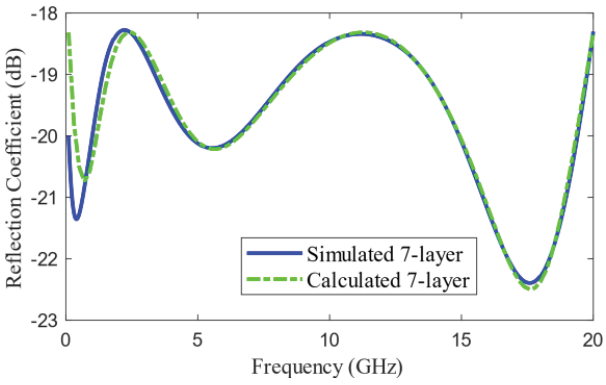

(b)

Fig. 11. Comparison of reflectance coefficients calculated by MIGRO and simulated by CST: (a) 5-layer at 2-8 GHz and (b) 7-layer at 0.1-20 GHz.

validating the accuracy of the mathematical modeling and algorithm optimization process for the multilayer microwave absorber.

V. CONCLUSION

This paper presents MIGRO that combines three strategies for the optimization design of the multilayer microwave absorbers under normal incident conditions. This method can be used to obtain a set of coatings with the minimum reflection coefficients within a specific frequency and thickness range. Two multilayer absorbers were designed for 2-8 GHz, 5-layer, and 0.1-20 GHz, 7-layer scenarios, and their design results were compared with those of other algorithms published in the literature. In both cases, MIGRO exhibits lower maximum and average reflection coefficients compared to other algorithms. Therefore, the effectiveness of the improvement strategy has been validated, indicating that MIGRO have stronger optimization capabilities.

ACKNOWLEDGMENT

This work was supported by Postgraduate Research & Practice Innovation Program of Jiangsu Province (Grant No. SJCX23-1871, No. SJCX23-XY069 and No. SJCX23-XY071), College Students Innovation and Entrepreneurship Training Program (Grant No. 2023591 and No. 2023576), Yancheng Institute of Technology Teaching Reform Research Project under Grant No. YKT2022A028.

REFERENCES

[1] R. Panwar, S. Puthucheri, D. Singh, and V Agarwala, "Design of ferrite-graphene-based thin broadband radar wave absorber for stealth application," *IEEE Transactions on Magnetics*, vol. 51, no. 11, pp. 1-4, Nov. 2015.

[2] A. Delfini, M. Albano, A. Vricella, F. Santoni, G. Rubini, R. Pastore, and M. Marchetti, "Advanced radar absorbing ceramic-based materials for multifunctional applications in space environment," *Materials*, vol. 11, no. 9, p. 1730, Sep. 2018.

[3] S. Xie, Z. Ji, L. Zhu, J. Zhang, Y. Cao, J. Chen, R. Liu, and J. Wang, "Recent progress in electromagnetic wave absorption building materials," *Journal of Building Engineering*, vol. 27, p. 100963, Jan. 2022.

[4] S. Ren, H. Yu, L. Wang, Z. Huang, T. Lin, Y. Huang, J. Yang, Y. Hong, and J. Liu, "State of the art and prospects in metal-organic framework-derived microwave absorption materials," *Nano-Micro Letters*, vol. 14, no. 1, p. 68, Feb. 2022.

[5] H. Pang, Y. Duan, L. Huang, L. Song, J. Liu, T. Zhang, X. Yang, J Liu, X. Ma, J Di, and X. Liu, "Research advances in composition, structure and mechanisms of microwave absorbing materials," *Composites Part B: Engineering*, vol. 224, p. 109173, Nov. 2021.

[6] R. Panwar and J. R. Lee, "Recent advances in thin and broadband layered microwave absorbing and shielding structures for commercial and defense applications," *Functional Composites and Structures*, vol. 1, no. 3, p. 032022, July 2019.

[7] E. Michielssen, J. M. Sajer, S. Ranjithan, and R. Mittra, "Design of lightweight, broad-band microwave absorbers using genetic algorithms," *IEEE Transactions on Microwave Theory and Techniques*, vol. 41, no. 6, pp. 1024-1032, June/July 1993.

[8] S. Chamaani, S. A. Mirtaheri, and M. A. Shooredeli, "Design of very thin wide band absorbers using modified local best particle swarm optimization," *AEU-International Journal of Electronics and Communications*, vol. 62, no. 7, pp. 549-556, Aug. 2008.

[9] S. Roy, S. D. Roy, J. Tewary, A. Mahanti, and G. Mahanti, "Particle swarm optimization for optimal design of broadband multilayer microwave absorber for wide angle of incidence," *Progress in Electromagnetics Research B*, vol. 62, pp. 121-135, Feb. 2015.

[10] S. K. Goudos, "Design of microwave broadband absorbers using a self-adaptive differential evolution algorithm," *International Journal of RF and Microwave Computer-Aided Engineering*, vol. 19, no. 3, pp. 364-372, Apr. 2009.

[11] N. I. Dib, M. Asi, and A. Sabbah, "On the optimal design of multilayer microwave absorbers," *Progress in Electromagnetics Research C*, vol. 13, pp. 171-185, 2010.

[12] M. Asi and N. I. Dib, "Design of multilayer microwave broadband absorbers using central force optimization," *Progress in Electromagnetics Research B*, vol. 26, pp. 101-113, 2010.
[13] Y. Lu and Y. Zhou, "Design of multilayer microwave absorbers using hybrid binary lightning search algorithm and simulated annealing," *Progress in Electromagnetics Research B*, vol. 78, pp. 75-90, 2017.
[14] S. Kankılıç and E. Karpat, "Optimization of multilayer absorbers using the bald eagle optimization algorithm," *Applied Sciences*, vol. 13, no. 18, p. 10301, Sep. 2023.
[15] S. Roy, A. Mahanti, S. D. Roy and G. K. Mahanti, "Comparison of evolutionary algorithms for optimal design of broadband multilayer microwave absorber for normal and oblique incidence," *Applied Computational Electromagnetics Society (ACES) Journal*, vol. 31, no. 1, pp. 79-84, Jan. 2016.
[16] T. Wang, G. Chen, J. H. Zhu, H. Gong, L. M. Zhang, and H. J. Wu, "Deep understanding of impedance matching and quarter wavelength theory in electromagnetic wave absorption," *Journal of Colloid and Interface Science*, vol. 595, pp. 1-5, Aug. 2021.
[17] K. Zolf, "Gold rush optimizer: A new population-based metaheuristic algorithm," *Operations Research and Decisions*, vol. 33, no. 1, pp. 113-150, 2023.
[18] M. Saglam, Y. Bektas, and O. A. Karaman, "Dandelion optimizer and gold rush optimizer algorithm-based optimization of multilevel inverters," *Arabian Journal for Science and Engineering*, vol. 49, pp. 7029-7052, Jan. 2024.
[19] H. Abdelfattah, M Esmail, S. A. kotb, M. M. Mahmoud, H. S. Hussein, D. E. M. Wapet, A. I. Omar, and A. M. Ewais, "Optimal controller design for reactor core power stabilization in a pressurized water reactor: Applications of gold rush algorithm," *Plos One*, vol. 19, no. 1, p. e0287772, Jan. 2024.
[20] Z. Wang, L. Huang, S. Yang, D. Li, D. He, and S. Chan, "A quasi-oppositional learning of updating quantum state and Q-learning based on the dung beetle algorithm for global optimization," *Alexandria Engineering Journal*, vol. 81, pp. 468-488, Oct. 2023.
[21] W. Liu, Z. Wang, Y. Yuan, N. Zeng, K. Hone, and X. Liu, "A novel sigmoid-function-based adaptive weighted particle swarm optimizer," *IEEE Transactions on Cybernetics*, vol. 51, no. 2, pp. 1085-1093, July 2019.
[22] Q. Liu, N. Li, H. Jia, Q. Qi, L. Abualigah, and Y. Liu, "A hybrid arithmetic optimization and golden sine algorithm for solving industrial engineering design problems," *Mathematics*, vol. 10, no. 9, p. 1567, May 2022.
[23] E. Yigit and H. Duysak, "Determination of optimal layer sequence and thickness for broadband multilayer absorber design using double-stage artificial bee colony algorithm," *IEEE Transactions on Microwave Theory and Techniques*, vol. 67, no. 8, pp. 3306-3317, Aug. 2019.
[24] H. Yao, J. Yang, H. Li, J. Xu, and K. Bi, "Optimal design of multilayer radar absorbing materials: A simulation-optimization approach," *Advanced Composites and Hybrid Materials*, vol. 6, no. 1, p. 43, Jan. 2023.
[25] P. Warhekar, A. Bhattacharya, and S. Neogi, "Designing thinner broadband multilayer radar absorbing material through novel formulation of cost function," *IEEE Access*, vol. 11, pp. 91016-91027, Oct. 2023.

Yi Ming Zong received the B.S. degree in electronic information engineering from Yancheng Institute of Technology in 2022. He is currently pursuing the M.Eng. degree in electronic information at Yancheng Institute of Technology. His main research interests focus on computational electromagnetics and artificial intelligence.

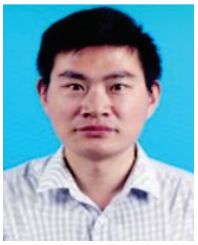

Wei Bin Kong received the B.S. degree in mathematics from Qufu Normal University, China, 2007, the M.S. degree in mathematics from Southeast University, Nanjing, China, in 2010, and the Ph.D. degree in radio engineering from Southeast University, Nanjing, China, in 2015. Since 2020, he has been an associate professor with the College of Information Engineering, Yancheng Institute of Technology, Yancheng. His current research interests include computational electromagnetism, artificial intelligence, and wireless communication.

Jia Pan Li received the B.S. degree in college of information and communication engineering from Harbin Engineering University. He is currently working toward the master's degree in electronic and information engineering at Southeast University. His current research interests include signal processing and optimum algorithms.

Lei Wang received the B.S. degree in integrated circuit design and integrated systems and the Ph.D. degree in information and communication engineering from Nantong University, Nantong, Jiangsu, China, in 2017 and 2023, respectively. Since 2023, he has been a Lecturer with the College of Information Engineering, Yancheng Institute of Technology, Yancheng. His current research interests include artificial intelligence and antenna, millimeter-wave antennas and arrays, and characteristic mode analysis.

Hao Nan Zhang received the B.S. degree from the Southeast University Chengxian College, Nanjing, China, in 2021, and he is currently pursuing the M.Eng. degree at Yancheng Institute of Technology. His current research interests include computational electromagnetics and wireless communications.

Feng Zhou received the B.S. degrees and M.S. degrees from Southeast University, Nanjing, China, in 2004 and 2012, respectively. Since 2023, he is a professor with the College of Information Engineering, Yancheng Institute of Technology, Yancheng, China. His research interests include cooperative communication, satellite communication, cognitive radio, physical layer security, and UAV communication.

Zi Yao Cheng is currently pursuing the bachelor's degree in opto-electronic information engineering with Yancheng Institute of Technology. During the bachelor's degree, he actively participated in multiple research projects on object detection and made outstanding contributions to optimizing object detection models. His research interests include computer vision and intelligent algorithms.

A Nulling Widen and Deepening Algorithm using a Modified Correlation Subtraction Algorithm Multistage Wiener Filtering

Xiao Li and Xinhuai Wang

Department of Electrical Engineering
Xidian University, Xian 710071, China
hxazgsja075@gmail.com

***Abstract* –** The calculation of beamforming weights takes time due to the constantly changing direction of interference in highly dynamic environments. The traditional anti-jamming means under static or low dynamic are almost all invalid, so the nulling widen algorithm is studied. However, the commonly used cavitation widening and deepening algorithms are often accompanied by a large amount of computational complexity, which may lead to computational inefficiency and slow processing speed in practical applications. In order to solve this problem, a nulling widen and deepening algorithm using a modified correlation subtraction algorithm multistage Wiener filtering is proposed. The algorithm achieves the deepening after nulling widening by constructing a new covariance matrix, and then reduces the rank by truncating the multilevel Wiener filter at the r-level. It finds the blocking matrix with the normalized reference vectors instead of calculating the blocking matrix directly so that the normalized reference vectors are orthogonal to each other, and finally completes the interference suppression by using the power inversion algorithm to improve the performance and reduce the amount of computation. The computational complexity of the algorithm based on the modified correlation subtraction algorithm multistage Wiener filtering (MCSA-MWF) is $O\left(rM^2\right)$, which is greatly reduced compared to the computational complexity of the traditional null-spread class algorithm with direct inversion $O\left(M^3\right)$.

***Index Terms* –** Adaptive anti-jamming, modified correlation subtraction algorithm multistage Wiener filtering (MCSA-MWF), nulling widen and deepening.

I. INTRODUCTION

Satellite navigation technology provides users with coordinates in time and space, which is of great strategic military importance in aviation, space and guided weapons, as well as being of great economic interest, and is nowadays indispensable in the transport industry. Satellite navigation technology is in great demand both in the military and civilian sectors.

Since the satellite is very far away from the receiver and the transmit power of the satellite is very weak, the navigation signal is very likely to receive interference [1, 2]. However, under high dynamic conditions, traditional anti-jamming means under static or low dynamic are almost all invalid, so the nulling widen algorithm is studied.

The nulling technique forms a stable beam nulling in the direction of the interference to provide cancellation with the interfering signal. The nulling widen algorithms are generally divided into interference-plus-noise covariance (INC) and the nulling widen algorithms based on covariance matrix taper (CMT) [4]. INC algorithms are generally more computationally intensive and often require some a priori information such as the direction of the interference and the direction of the desired signal [5]. In cases where the incoming information of the desired signal is known, the nulling is widened by removing the expected signal from the covariance matrix. In contrast, the CMT algorithm is much less computationally intensive. The CMT algorithm was proposed by Mailloux [4], which rewrites the covariance matrix by setting up a virtual interference to widen the nulling with a taper matrix.

Other scholars have proposed different methods for nulling widen. Zatman [7] converts the narrowband interference signal into a virtual broadband interference signal to widen the nulling. Li et al. [8] established a Gaussian distribution model based on the interference. Based on the Gaussian distribution, Cong et al. [9] designed an algorithm to deepen the nulling by perspective drawing. Zeng et al. [10] theoretically deduced that the sufficient condition for the FIR filter not to change the zero value is the symmetry of coefficients or conjugate symmetry. On this basis, a nulling widen algorithm based on virtual interference is proposed [11]. A new method of space-time joint adaptive processing (STAP) null-widen is deduced based on the Laplace distribution model of the changing interference direction of arrival (DOA) in a high-dynamic environment [12, 13] by taking the moving interferences as discrete interference sources

Submitted On: April 28, 2024
Accepted On: September 29, 2024

https://doi.org/10.13052/2024.ACES.J.390807

that obey the Laplace distribution. Thus, the average covariance matrix can be calculated to broaden the width of nulls. In [22], a procedure for the null widen algorithm design with respect to the nonstationary interference is proposed.

In addition, many more studies have focused on covariance matrices. For nulling widen, [14] is implemented by a simple modification of the measured covariance matrix. Reference [15] explores the theory and application of covariance matrix tapers for robust adaptive beamforming. In [16], CMTs and derivative constraints in the directions of jammers have been proposed to widen the nulling in adaptive processing, thereby improving the algorithms' robustness. Reference [17] develops a computationally efficient online implementation of the CMT technique based on a low-rank approximation of the taper matrix and the recursive least squares (RLS) algorithm. In reference [18], by means of the covariance matrix of the auxiliary elements, a nulling widen method was realized based on the sidelobe canceller. This approach demonstrated good performance in practical applications, but has increased hardware complexity. Reference [23] proposed a computationally efficient nulling widen method for sidelobe canceller, which is a CMT based method and puts fictitious interference into snapshots to broaden the sharp null. Based on Mailloux's methodology, the covariance matrix and cross-correlation vector were tapered via random disturbance. Compared with the existing methods, the method required much less computation, but its performance is similar.

Meanwhile, some studies have reconstructed the algorithmic correlation matrix (such as INC matrix and covariance matrix) to achieve nulling widen. In [19, 20], an adaptive null widen technique based on reconstruction of the covariance matrix was proposed. Reference [21] proposes an algorithm based on INC matrix reconstruction by setting up several virtual interference sources, which can simultaneously broaden the nulls. Null depth and width can be controlled by setting the parameters of the virtual interference sources.

The multistage Wiener filter (MWF) [24] is a multilevel equivalent realization of the Wiener filter, which uses a sequence of orthogonal projections to decompose the array signal vectors at multiple levels, and then performs multistage scalar Wiener filtering to synthesize the error signals of the Wiener filter. Depending on the blocking matrix, the multilevel Wiener filter can be implemented with different algorithms. The MWF was first proposed by Goldstein, Reed, and Scharf in [24], whose Appendix A gives a method for calculating the blocking matrix, and calls the algorithm GRS-MWF, with GRS being an abbreviation of the authors' names. References [25–28] proposed a MWF implementation method that effectively reduces the computational effort called the correlation subtraction algorithm, denoted CSA-MWF. Reference [29] proposed a modified correlation subtraction algorithm multistage Wiener filtering (MCSA-MWF) based on CSA algorithm, which improves the blocking matrix of CSA-MWF so as to have the advantages of GRS-MWF. The improved blocking matrix can be realized with the CSA structure. This results in good numerical stability, i.e., reduced-rank performance, and a further reduction in computational effort.

In order to reduce the amount of computation and make it more robust even in small snapshot environments, we combined the MCSA-MWF with the CMT algorithm to propose a nulling widen and deepening algorithm using a modified correlation subtraction algorithm MWF.

The main contributions of this paper are as follows:

A new MCAS-MWF based nulling widen and deepening algorithm is proposed, which can improve the stability of the algorithm for small snapshot data in highly dynamic environments.

The normalized reference vectors are used to solve for the blocking matrix instead of computing (constructing) the blocking matrix, thus making the normalized reference vectors orthogonal to each other and effectively reducing the arithmetic.

We compare the performance of the MCAS-MWF based nulling widen and deepening algorithm through typical experiments. The simulation experiments show that the proposed algorithm has good performance under both ideal circular array conditions and real measured BeiDou data.

The rest of the paper is organized as follows: section II introduces the signal model, section III describes the nulling spread-and-deepen algorithm based on MCAS-MWF, section IV demonstrates the simulation of the algorithm under the ideal uniform circular array and the real measured BeiDou data, and section V concludes the work of this paper.

II. SIGNAL MODELLING

A. Arbitrary plane array system model

As is shown in [32], for a two-dimensional M-element arbitrary array planar array, in the setting of L signal, Q interference, the received data model of the signal in an environment with four interferences is:

$$\begin{aligned} X(t) &= X_S(t) + X_I(t) + n \\ &= \sum_{I=1}^{L} a(\theta_1, \varphi_1)\, s_1(t) + \sum_{q=1}^{Q} a(\theta_q, \varphi_q)\, s_q(t) + n, \end{aligned} \tag{1}$$

where $X_S(t)$ is the received desired signal source, $X_1(t)$ is the interference signal received and n is the noise. (θ_1, φ_1) and (θ_q, φ_q) are the incoming direction of the

$1th$ signal and the qth interference, respectively. θ and φ are the pitch and azimuth angles. $s_1(t)$ and $s_q(t)$ are the $1th$ signal and the qth interference, respectively. a is the airspace guidance vector. For any 2D planar array, the airspace guidance vector is:

$$a(\theta,\varphi)=\left[e^{ju^T(\theta,\varphi)P_1},e^{ju^T(\theta,\varphi)P_2},e^{ju^T(\theta,\varphi)P_m}\right], \quad (2)$$

where P_m is the position vector of the mth array element and u is the beam vector with the expression:

$$P_m=d_m[\cos r_m,\sin r_m]^T, \quad (3)$$

$$u(\theta,\varphi)=\frac{2\pi}{\lambda}\begin{bmatrix}\sin(\theta)\ \cos(\varphi)\\ \sin(\theta)\ \sin(\varphi)\end{bmatrix}. \quad (4)$$

$\pi=3.14$, $\lambda\in(380\sim760)nm$, d_m expressed as $d_m=\sqrt{x_m^2+y_m^2}$, i.e., the Euclidean distance of each array element from the reference array element. r_m is the angle of each array element.

The power inversion algorithm (PI) is used for the anti-interference process and its weights are calculated as follows:

$$w_{opt}=\left(s^HR^{-1}s\right)^{-1}R^{-1}s, \quad (5)$$

where s is the constraint vectors and, at the same time, $s=[1,0,...,0]^T$. R is the covariance matrix of the received signal. The superscript$\{\cdot\}^H$ denotes the Emmett transpose. The sampled data is used in practical engineering to approximate R:

$$\tilde{R}=\frac{1}{K}\sum_{k=1}^{K}X(k)X^H(k), \quad (6)$$

where K is the number of sampling beats and $\tilde{R}\to R$ when $K\to\infty$.

B. BeiDou signal model

The BeiDou Navigation Satellite System (BDS) launched the construction of the BeiDou Satellite Navigation Pilot System in 1994, completed the BeiDou II regional service system in 2012, and completed the full-scale construction of the BeiDou III system in 2020, achieving the goal of global navigation and positioning.

According to the B3I interface control document [30], the expression for the B3I signal is:

$$S_{B3I}^j(t)=A_{B3I}C_{B3I}^j(t)D_{B3I}^j(t)\cos\left(2\pi f_3t+\varphi_{B3I}^j\right), \quad (7)$$

where A_{B3I} denotes the amplitude of the B3I signal, C_{B3I}^j denotes the ranging code of satellite j, D_{B3I}^j denotes the data code of satellite j, f_3 denotes the carrier frequency of the B3I signal, and the nominal carrier frequency is 1268.52 MHz. φ_{B3I} denotes the signal carrier initial phase and the bandwidth of the B3I signal is 20.46 MHz.

The generation mechanism of the BeiDou signal is shown in Fig. 1. One pseudo-random code cycle is modulo two-added to one NH code bit, and one NH code cycle is modulo two-added to one navigation message bit, followed by BPSK modulation to produce the space RF signal. Each satellite has a unique ranging code, and

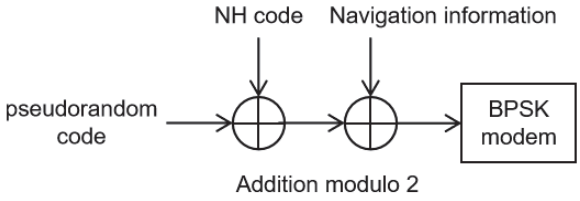

Fig. 1. Schematic diagram of BeiDou B3I signal coding process.

the ranging code CB3I for B3I has a code rate of 10.23 Mcps and a period of 10230.

III. MCAS-MWF BASED NULLING WIDENING AND DEEPENING ALGORITHM

A. Principle of nulling widening and deepening algorithm

Since the direction of interference in high-speed environments changes constantly, the calculation of beamforming weights takes time, and the calculated weights are strictly applicable to the moment before the calculation of the weights. Thus, the direction of interference will change rapidly. Moreover, the width of the conventional beamforming nulling is particularly narrow, so once the direction of interference changes slightly, it will be out of the generated nulling area, and the nulling will not allow the interference to come in and generate an offset. Thus, the effect of interference suppression will be rapidly degraded, which makes the anti-jamming algorithm ineffective. In order to keep the anti-jamming algorithm stable in the high-speed environment, the commonly used algorithm is the nulling widen algorithm.

Nulling widen is achieved using the CMT method. The effect of change in the direction of the interference is embodied in the covariance matrix R of the received signal, under the action of the taper matrix T.

For a nulling spread of a line matrix [8], the taper matrix T is:

$$T_{k,l}=e^{\left\{\frac{1}{2\sigma_{\max}^2[(k-1)\pi/180]^2}\right\}}, \quad (8)$$

where $\sigma_{\max}^2$ determines the width of the nulling. The new covariance matrix $\bar{R}$ is obtained from the Hadamard product of the taper matrix $T_{k,l}$ and the old covariance matrix R. The conical covariance matrix is:

$$\bar{R}_L=\tilde{R}^{\circ}\bar{T}_L. \quad (9)$$

Nulling widen can be produced by solving for the beamforming weights using the tapered covariance matrix. In order to achieve nulling widen and deepening on this basis, the sampled covariance matrix of equation (6) is eigen-decomposed:

$$\tilde{R}=\sum_{m=1}^{M}\lambda_me_me_m^H, \quad (10)$$

where λ_m is the eigenvalue of $\tilde{R}$, e_m is the corresponding eigenvector. λ_m in descending order, and its magnitude, reflects the power of the corresponding signal or interference:

$$\lambda_1 \geq \lambda_2 \cdots \geq \lambda_Q > \lambda_{Q+1} = \cdots = \lambda_M = \sigma_n^2. \quad (11)$$

In the navigation receiver the interference energy is much larger than the navigation signal, so the first Q large eigenvalues correspond to the subspace of the interference, so that the set is $U_I = [e_1, e_2, \cdots, e_Q]$. The equation is as follows:

$$\begin{aligned} &span\{a(\theta_1,\phi_1), a(\theta_2,\phi_2), \cdots, a(\theta_Q,\phi_Q)\} \\ &\quad = span\{e_1, e_2, \cdots, e_Q\} \end{aligned}. \quad (12)$$

Afterwards, a projection transformation is performed to extract the interference components and then weight the coefficients of the interference components to obtain the processed sampled data as:

$$\bar{X}(k) = X(k) + gTX(k) = (I_k + gT)X(t). \quad (13)$$

Based on the characteristic subspace property, the projection matrix of the interference subspace is found to be:

$$T = U_I \left(U_I^H U_I\right)^{-1} U_I^H, \quad (14)$$

where g is a weighting factor that serves to change the nulling depth in dB, U_I is signal subspace.

Finally, the new covariance matrix after preprocessing is:

$$\begin{aligned} \tilde{R}_T &= \frac{1}{K}\sum_{k=1}^{K} \bar{X}(k)\bar{X}^H(k) \\ &= (I_K + gT)\tilde{R}(I_K + gT)^H, \end{aligned} \quad (15)$$

where $\tilde{R}_T$ is the covariance matrix after taper, I_K is a unit matrix of length K. This covariance matrix is used to replace the previous sampling covariance matrix.

B. Correlated phase reduction MWF

MWF [31] is an equivalent algorithm to the Wiener filter, which avoids matrix inversion and thus reduces the volume of computation. Correlation subtraction algorithm multistage Wiener filtering (CSA-MWF) further reduces the forward recursion based on MWF and avoids blocking matrix computation compared to MWF. MCSA-MWF further reduces the number of dimensions, and its block diagram is shown in Fig. 2. In GRS-MWF, its blocking matrix uses the $(N-i-1)\times(N-i)$ rectangular matrix B_i, and the dimension of $X(k)$ decreases step by step, which is conducive to reducing the computation and storage. CSA-MWF is a Wiener multistage filter with subspace basis vectors orthogonal to each other, the blocking matrices B_i are all N-dimensional square matrices, and all levels of observation data $X_i(k)$ are also N-dimensional square matrices. From the principle of CSA-MWF, it can be seen that reduced-rank processing does not lead to the reduction of dimension, so the data redundancy is large. It can be envisioned that if the blocking matrix is adopted as a $(N-i-1)\times(N-i)$ rectangular matrix, it not only utilizes the CSA structure of CSA-MWF without solving the blocking matrix, but also exploits the advantages of GRS-MWF's dimension reduction, making the $X_i(k)$ dimension of the MWF reduce step by step. This structure is referred to as MCSA-MWF, and the structure is shown in Fig. 2 [31], which combines the advantages of GRS-MWF and CSA-MWF to obtain almost the same performance as CSA-MWF, but with less computational effort than both.

In Fig. 2, the forward recursive formula for MCSA-MWF level i is as follows:

$$h_i = \frac{r_{X_{i-1}d_{i-1}}}{\sqrt{r_{X_{i-1}d_{i-1}}^H r_{X_{i-1}d_{i-1}}}}, \quad (16)$$

$$d_i(k) = h_i^H X_{i-1}(k), \quad (17)$$

$$B_i = I_{N-i}^{(N-i-1)} - h_i^{(N-i-1)} h_i^H, \quad (18)$$

$$X_i(k) = B_i X_{i-1}(k) = X_{i-1}^{(N-i-1)}(k) - h_i^{(N-i-1)} d_i(k), \quad (19)$$

where h_i is N-dimensional, $X_i(k)$ is an $N-i-1$ dimensional vector, and $I_{N-i}^{(N-i-1)}$ denotes the upper $N-1$ rows of the N-dimensional unit array.

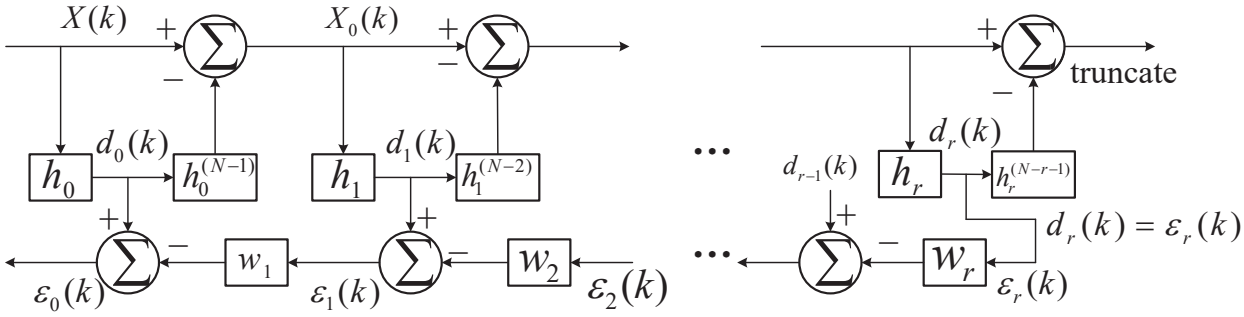

Fig. 2. MCSA-MWF structure block diagram.

C. An MCAS-MWF based nulling widen and deepening algorithm

According to [6], the MCSA-MWF weights are solved for:

$$W_{MCSA-MWF} = h_0 - B_0^H T_D W_d. \tag{20}$$

When using the power inversion algorithm:

$$h_0 = [1, 0, \cdots, 0]^T, \tag{21}$$

$$T_D = [t_1, t_2, \cdots, t_D], \tag{22}$$

$$t_i = \left(\prod_{j=1}^{i-1} B_j^H \right) h_i, \tag{23}$$

$$h_i = \frac{r_{X_{i-1}d_{i-1}}}{\left\| r_{X_{i-1}d_{i-1}} \right\|}, \tag{24}$$

included among these:

$$\begin{aligned} r_{X_{i-1}d_{i-1}} &= E\left[X_{i-1}d_{i-1}^*\right] \\ &= B_{i-1}\left(\prod_{r=i-2}^{0} B_r \right) R_{XX} \left(\prod_{r=i-2}^{0} B_r \right)^H h_{i-1}, \end{aligned} \tag{25}$$

$$B_i = I_{M-i}^{(M-i-1)} - h_i^{(M-i-1)} h_i^H, \tag{26}$$

$$W_d = \left(T_D^H B_0 R_{XX} B_0^H T_D \right)^{-1} T_D^H B_0 R_{XX} h_0, \tag{27}$$

where r is the order of the truncated reduced rank, and $h_i i = 1, 2, 3..., D)$ is the recursive weights in the MWF, B_i is the blocking matrix, W_d is the backward Wiener filter, R_{XX} is the received signal autocorrelation matrix, and t_i is the basis vector of the reduced-rank subspace. Equation (26) can be obtained from [3], the superscript n of it denotes the upper n rows of the fetch matrix. After derivation, the weights of MCSA-MWF-PI can be calculated as:

$$\begin{aligned} W_{MCSA-MWF-PI} &= h_0 \\ -B_0^H T_D \left(T_D^H B_0 R_{XX} B_0^H T_D \right)^{-1} T_D^H B_0 R_{XX} h_0 \end{aligned}. \tag{28}$$

By bringing equation (9) of $\overline{\mathrm{R_L}}$ into the above equation, then the Laplace nulling widen power inversion algorithm based on the MCSA-MWF-LNW-PI is:

$$\begin{aligned} W_{MCSA-MWF-LNW-PI} &= h_0 \\ -B_0^H T_D \left(T_D^H B_0 \bar{R}_L B_0^H T_D \right)^{-1} T_D^H B_0 \bar{R}_L h_0 \end{aligned}. \tag{29}$$

By bringing equation (15) of $\widetilde{\mathrm{R}}_{\mathrm{T}}$ into the above equation, then the Laplace nulling widen and deepening power inversion algorithm based on the MCSA-MWF-LNWD-PI is:

$$\begin{aligned} W_{MCSA-MWF-LNWD-PI} &= h_0 \\ -B_0^H T_D \left(T_D^H B_0 \tilde{R}_T B_0^H T_D \right)^{-1} T_D^H B_0 \tilde{R}_T h_0 \end{aligned}. \tag{30}$$

As shown in the Table 1, compared with the computational complexity of the conventional nulling widen algorithm for direct inverse $\mathrm{O}\left(\mathrm{M}^3\right)$, the computational complexity of the algorithm based on the MCSA-MWF-LNWD-PI is $\mathrm{O}\left(\mathrm{rM}^2\right)$. If it is a N-tap null-time joint algorithm, the computational complexity of the algorithm changes from $\mathrm{O}\left((\mathrm{MN})^3\right)$ to $\mathrm{O}\left(\mathrm{r}(\mathrm{MN})^2\right)$, which greatly reduces the computational complexity.

Table 1: Comparison of the computational complexity of the two nulling widen algorithms

Arithmetic	Complexity	N-tap Null-Time Joint Algorithm
Conventional algorithm	$\mathrm{O}\left(\mathrm{M}^3\right)$	$\mathrm{O}\left((\mathrm{MN})^3\right)$
Based on the MCSA-MWF-LNWD-PI	$\mathrm{O}\left(\mathrm{rM}^2\right)$	$\mathrm{O}\left(\mathrm{r}(\mathrm{MN})^2\right)$

IV. ALGORITHM SIMULATION

In this section, we use the ideal seven-element uniform circular array and seven-channel measured BeiDou data to carry out algorithm simulation separately and compare the anti-jamming performance of different algorithms.

A. MCSA-MWF performance analysis

There are several different algorithmic implementations of the multilevel Wiener filter, such as CSA-MWF, GRS-MWF, and MCSA-MWF. In CSA-MWF, the blocking matrices B_i are all N-dimensional square matrices, and the observation data $X_i(k)$ at each level are all N-dimensional vectors. The blocking matrices of MCSA-MWF adopt the rectangular matrices of size $(N-i-1)\times(N-i)$, which can take advantage of the CSA structure of CSA-MWF, which does not need to solve the blocking matrices and reduces computation. An advantage of the decreasing dimension of $X_i(k)$ in GRS-MWF is to further reduce computation while maintaining the reduced-rank performance.

In adaptive beamforming based on the GSC framework, in addition to the usual performance metrics (e.g., array orientation map, output signal-to-noise ratio), there is also a special metric called mean square error (MSE). Several implementations of MSE are defined [29]:

$$MSE = W_X^H R W_X, \tag{31}$$

$$SMSE = W_X^H R_X W_X, \tag{32}$$

$$MMSE = W_{opt}^H R W_{opt}. \tag{33}$$

MSE is the result obtained by applying the sampled adaptive weight vector print to the ideal array data statistics. SMSE (sample mean square error) is the result obtained by applying the sampled adaptive weight vector to the training data itself. MMSE (minimum mean square error) is the result obtained by applying the ideal adaptive weight vector to the ideal array data statistics.

Now let us compare the three MWFs mentioned above using these metrics. Figure 3 shows the curve of MMSE with the rank change of three different algorithms in a uniform linear array with N=16 elements. Since MMSE examines the performance of the algorithm from the overall statistical characteristics, it can reflect the performance of the algorithm under certain signal

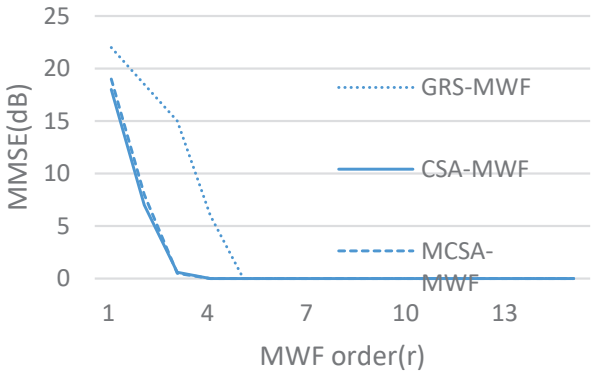

Fig. 3. The curve of MMSE with rank change of three different algorithms in a uniform linear array.

statistical characteristics. Thus, MMSE is an important indicator of the performance of the algorithm. In Fig. 3, the MMSE curve of MCSA-MWF and CSA-MWF are close to the minimum at r = 3.

Let the rank of the reduced-rank multilevel Wiener filter be r and the number of snapshots be K, then the computational amount (number of multiplications) of the three r-order multilevel Wiener filters GRS-MWF, CSA-MWF, MCSA-MWF can be compared as shown in Table 2, which refers to the computational amount of the forward recursion since the backward recursive synthesis is exactly the same. It can be seen that the computation amount of GRS-MWF is $O\left(N^2\right)$, while that of CSA-MWF and MCSA-MWF is only $O(N)$, and the number of multiplications of MCSA-MWF is lower than that of CSA-MWF by $Kr(r+1)$ times. It can be seen that MCSA-MWF is especially suitable for large arrays with more adaptive degrees of freedom, such as the spatial adaptive processing in complex interference environments. MCSA-MWF is finally used instead of CSA-MWF because the blocking matrix of MCSA-MWF is rectangular, which reduces the computational effort.

Table 2: Comparison of the computational complexity of the two nulling widen algorithms

Algorithm / Calculated amount	$X_i(k)=B_iX_{i-1}(k)$	$d_i(k)=h_i^HX_{i-1}(k)$
GRS-MWF	$K[N^2+(N-1)^2+...+(N-r+1)^2]$	$K[N+(N-1)+...+(N-r)]$
CSA-MWF	$KN(r)$	$KN(r+1)$
MCSA-MWF	$K[(N-1)+...+(N-r)]$	$K[N+(N-1)+...+(N-r)]$

Figures 4 and 5 show the relationship between the nulling angel/gain and the MWF order, demonstrating the orientation and gain at different ranks. The best results are obtained when r=6, the gain in this case did not disappear and is the minimum. Therefore, in later simulation experiments, we chose the rank of MCSA-MWF as 6.

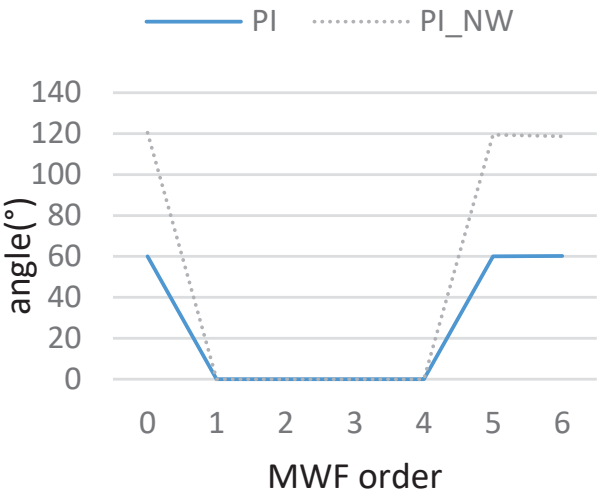

Fig. 4. Relationship between nulling angle and MWF order.

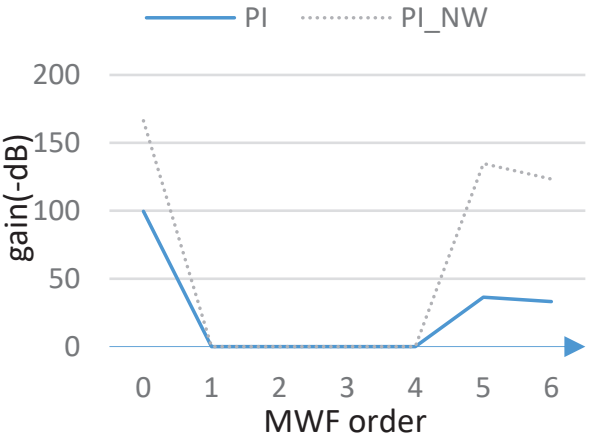

Fig. 5. Relationship between nulling gain and MWF order.

B. MCSA-MWF-LNW-PI algorithm ideal state simulation

The BeiDou data used in this paper consists of seven channels of data, with a total of seven rows, so we chose

to use a seven-element uniform circular array when performing the simulation in the ideal case.

Simulation of the LNWD algorithm and the MCSA-MWF-LNW-PI in a 2D uniform circular-center array. A seven-element circular-center array is set up with a signal-to-noise ratio of -20 dB, a dry-to-noise ratio of 60 dB, a snap count of 2046, a signal incoming direction (10°, 45°), and the incoming direction of the interference is (20°, 50°). The orientation diagram is shown in Fig. 6. The nulling after using the MCSA-MWF of order 6 is basically the same as the ideal case, which can be used in both nulling widen as well as nulling widen and deepening algorithms, which has a very low impact on the nulling but serves to reduce the dimension, which reduces the computational effort.

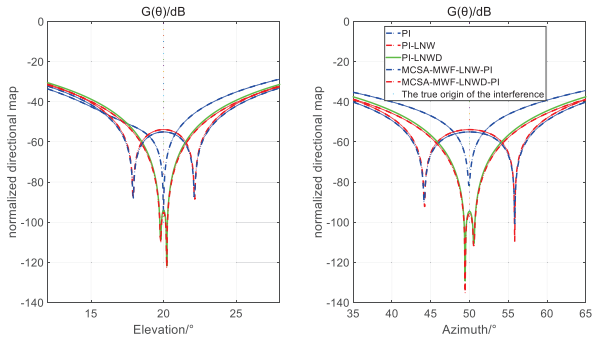

(a) (b)

Fig. 6. Comparison of direction map nulling for MCSA-MWF and ideal algorithm: (a) elevation orientation diagram and (b) azimuth orientation diagram.

C. MCSA-MWF-LNW-PI algorithm simulation of real data

The BeiDou data used in this paper consists of seven channels of data, with a total of seven rows, so we chose to use a seven-element uniform circular array when performing the simulation in the ideal case.

According to the official documents of the BeiDou satellite navigation system, the space constellation of BeiDou-3 consists of three geostationary orbit satellites (GEO), three inclined geosynchronous orbit satellites (IGSO), and 24 medium circular earth orbit satellites (MEO). The LNWD algorithm and the MCSA-MWF-LNWD algorithm simulated for the sampled B3I signal. The B3I signal is sampled with three interfering data of seven channels, with a total of seven rows, and each row represents the data of one channel, and the data time length is about 100 ms. The sampled data is the signal of the BD B3 frequency point, with a data sampling rate of 62 MHz, and an intermediate frequency of 80.52 MHz.

Figure 7 shows the comparison of the antenna gain direction plots after using the PI algorithm in two cases, where PI (blue line) is the ideal case. Its purpose is to see the effect of the nulling widen algorithm using the MCSA-MWF on the nulling. From the two graphs in Fig. 7, it can be seen that the nulling case (i.e., the lowest gain point) of the MCSA-MWF-LNW-PI algorithm is almost the same as the nulling of the ideal case, while the other two algorithms nulling cases are always different from the ideal case. So, it can be concluded that all the nulling cases after using MCSA-MWF with order 6 are basically the same as the ideal case, which can be used for the nulling widen and deepening algorithms, which have less effect on nulling but play the role of dimension reduction, thus reducing the amount of computation.

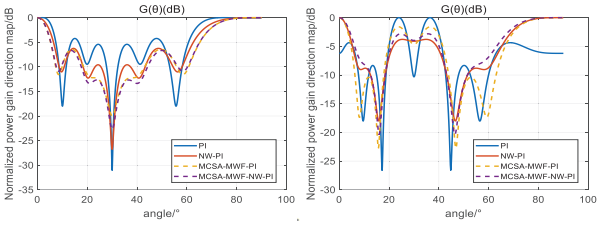

Fig. 7. Comparison of directional map nulling between MCSA-MWF and ideal algorithm under BeiDou data.

V. CONCLUSION

In this paper, we solve the problem of large inverse matrix operation of invalid broadening in adaptive anti-jamming algorithms under high dynamics. The performances of three commonly used MWF algorithms are compared, and the results show that MCSA-MWF greatly reduces the computational volume and dimension compared with CSA-MWF and GRS-MWF. Finally, we chose to combine the MCSA-MWF algorithm with the traditional zeroing and widening method and propose a new MCSA-MWF-LNWD algorithm, which improves the stability when using small snapshot data in real high dynamic environments.

In addition, several simulations including the ideal case of seven-element uniform circular array test and using seven-element real BeiDou data are conducted, and the results show that the nulling using MCSA-MWF is very close to the ideal case. This approach can be effectively applied to both cavitation widening and cavitation deepening algorithms. Although the cavitation effect may be degraded, it plays a key role in dimensionality reduction, which greatly reduces the computational effort. Compared with the computational complexity of the conventional nulling widen class algorithm for direct inverse $O(M^3)$. The computational complexity of the algorithm based on the MCSA-MWF is $O(rM^2)$, which greatly reduces the computational complexity.

REFERENCES

[1] J. R. Sklar, "Interference mitigation approaches for the global positioning system," *Lincoln Laboratory Journal*, vol. 14, no. 2, pp. 167-179, 2003.

[2] T. H. Kim, C. S. Sin, S. Lee, and J. H. Kim, "Analysis of performance of GPS L1 signal generator in GPS L1 signal," *IEEE 14th International Conference on Control, Automation and Systems,* pp. 1006-1009, Oct. 2014.

[3] D. C. Ricks, "Efficient architectures for implementing adaptive algorithms," in *Proc. 2000 Antenna Applications Symposium,* Allerton Park, Monticello, IL, pp. 29-41, Sep. 2000.

[4] R. J. Mailloux, "Covariance matrix augmentation to produce adaptive array pattern troughs," *IEEE Antennas and Propagation Society International Symposium. Dig.,* vol. 1, 1995.

[5] F. Shen, F. Chen, and J. Song, "Robust adaptive beamforming based on steering vector estimation and covariance matrix reconstruction," *IEEE Commun. Lett.*, vol. 19, no. 9, pp. 1636-1639, 2015.

[6] R. T. Compton, "The power-inversion adaptive array: Concept and performance," *IEEE Trans. Aerosp. Electron. Syst*, vol. 6, pp. 803-814, 1979.

[7] M. Zatman, "Production of adaptive array troughs by dispersion synthesis," *Electronics Lett.*, vol. 31, no. 25, pp. 2141-2142, 1995.

[8] R. Li, Y. Wang, and S. Wan, "Adaptive antenna direction map interference nulling widen method," *Modern Radar*, no. 2, pp. 42-45, 2003.

[9] Y. Cong, D. Feng, and H. Li, "A highly dynamic GNSS anti-jamming algorithm based on nulling widen and deepening," *J. Jilin Univ.: Information Sci. Ed.*, vol. 38, no. 1, pp. 1-8, 2020.

[10] X. Zeng, M. Li, and J. Nie, "Analysis of the effect of platform motion on antenna array performance in satellite navigation systems," *J. National Univ. Defence Technol.,* vol. 33, no. 1, pp. 5-8, 2011.

[11] X. Zeng, "Research on delay, quantisation and motion adaptation techniques in satellite navigation anti-jamming," M.S. thesis, National University of Defence Science and Technology, 2014.

[12] D. Lu, L. Ge, W. Wang, L. Wang, Q. Jia, and R. Wu, "A high-dynamic null-widen algorithm based on reduced-dimension space-time adaptive processing," *J. Electron. Inf. Technol.,* vol. 38, no. 1, pp. 216-221, 2016.

[13] Y. Ma, Y. Xu, and J. Li, "A high-dynamic null-widen GPS anti-jamming algorithm based on statistical model of the changing interference DOA," in *China Satellite Navigation Conference (CSNC) 2014 Proceedings,* Vol. 1, Springer, Berlin Heidelberg, 2014.

[14] R. J. Mailloux, "Covariance matrix augmentation to produce adaptive array pattern troughs," *IEEE Antennas and Propagation Society International Symposium. Dig.,* vol. 1, pp. 1-4, 1995.

[15] J. R. Guerci, "Theory and application of covariance matrix tapers for robust adaptive beamforming," *IEEE Trans. Signal Process.,* vol. 47, no. 3, pp. 977-985, 1999.

[16] M. Zatman and J. R. Guerci, "Comment on theory and application of covariance matrix tapers for robust adaptive beamforming," *IEEE Trans. Signal Process.,* vol. 48, no. 6, pp. 1796-1800, 2000.

[17] M. Rubsamen, C. Gerlach, and A. B. Gershman, "Low-rank covariance matrix tapering for robust adaptive beamforming," in *Proc. 2008 IEEE Int. Conf. Acoustics, Speech and Signal Processing,* Las Vegas, NV, pp. 2333-2336, 2008.

[18] Z. Liu, Z. Su, and Q. Hu, "Robust sidelobes cancellation algorithm with null widen," *J. Electron. Inf. Technol.,* vol. 38, no. 5, pp. 565-570, 2016.

[19] X. Yang, S. Li, T. Long, and T. K. Sarkar, "Adaptive null widen method in wideband beamforming for rapidly moving interference suppression," *Electron. Lett.,* vol. 54, no. 11, pp. 1003-1005, 2018.

[20] W. Li and B. Yang, "An improved null widen beamforming method based on covariance matrix reconstruction," in *2017 International Applied Computational Electromagnetics Society Symposium-Italy (ACES). IEEE,* Firenze, Italy, pp. 1-2, 2017.

[21] J. Yang, J. Lu, X. Liu, and G. Liao, "Robust null widen beamforming based on covariance matrix reconstruction via virtual interference sources," *Sensors,* vol. 20, no. 1865, 2020.

[22] J. Qian, Z. He, and J. Xie, "Null widen adaptive beamforming based on covariance matrix reconstruction and similarity constraint," *EURASIP J. Adv. Signal Process.,* vol. 2017, 2017.

[23] Z. Liu, S. Zhao, and G. Zhang, "Robust adaptive beamforming for sidelobe canceller with null widening," *IEEE Sensors Journal,* vol. 19, no. 23, pp. 11213-11220, 2019.

[24] J. S. Goldstein, I. S. Reed, and L. L. Scharf, "A multistage representation of the Wiener filter based on orthogonal projections," *IEEE Trans. Inf. Theory*, vol. 44, no. 7, pp. 2943-2959, Nov. 1998.

[25] D. C. Ricks and J. S. Goldstein, "Efficient architectures for implementing adaptive algorithms," in *Proc. 2000 Antenna Applications Symposium,* Allerton Park, Monticello, IL, pp. 29-41, Sep. 2000.

[26] D. C. Ricks, P. G. Cifuentes, and J. S. Goldstein, "Adaptive beamforming using multistage Wiener filter with a soft stop," *Conference Record of the Thirty-Fifth Asilomar Conference on Signals,*

Systems and Computers, Pacific Grove, CA, pp. 1401-1406, Nov. 2001.

[27] L. Huang, J. Zhang, X. Xu, and Z. Ye, "Robust adaptive beamforming with a novel interference-plus-noise covariance matrix reconstruction method," *IEEE Trans. Signal Process.,* vol. 63, no. 7, pp. 1643-1650, Apr. 2015.

[28] J. R. Guerci, "Theory and application of covariance matrix tapers for robust adaptive beamforming," *IEEE Trans. Signal Process.,* vol. 47, no. 4, pp. 977-985, Apr. 1999.

[29] Q. Ding, Y. Wang, and Y. Zhang, "An efficient implementation algorithm for multilevel Wiener filter in adaptive arrays," *Journal of Electronics and Information,* vol. 28, no. 5, pp. 936-940, 2006.

[30] BeiDou satellite navigation system space signal interface specification part 4: open service signal B3I, 2020.

[31] Q. Ding, Y. Wang, and Y. Zhang, "An efficient implementation algorithm for multilevel Wiener filter in adaptive arrays," *Journal of Electronics and Information,* vol. 28, no. 5, pp. 936-940, 2006.

[32] X. Wang and T. Li, "A zero-sag spreading and deepening algorithm for arbitrary planar arrays," *Journal of Terahertz Science and Electronic Information,* vol. 20, no. 8, pp. 830-835, 2022.

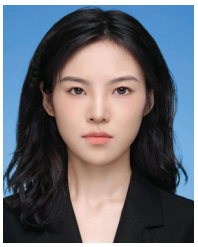

Xiao Li received the B.S. degree in Remote Sensing Science and Technology from the School of Electrical Engineering, Xidian University in 2023. She is now pursuing her master's degree in the Department of Electromagnetic Field and Microwave Technology at the same university. Her current research interests include smart antenna immunity.

Xinhuai Wang received the B.E. degree in electronic science and technology and Ph.D. degree in radio physics from Xidian University, Xi'an, China, in 2004 and 2010, respectively. Since 2010, he has been with the National Key Laboratory of Antennas and Microwave Technology, Xidian University, as a Lecturer. He has been an Associate Professor with Xidian University since 2014. He has been a Professor and Doctoral Supervisor since 2020. His recent research interests are mainly in microwave circuits and smart antenna system design.

Design of a High-frequency Antenna Along a Conducting Surface

Marius H. Vogel[1] and Mark H. Smith[2]

[1]Georgia Tech Research Institute
Williamsburg, VA 23185, USA
marius.vogel@gtri.gatech.edu

[2]Georgia Tech Research Institute
Smyrna, GA 30080, USA
mark.smith@gtri.gatech.edu

Abstract – Antennas in the high-frequency (HF) band (3-30 MHz) tend to be large and almost always protrude from the structure on which they are mounted. This paper will present a design in which the antenna is installed parallel to and close to a conducting surface. To achieve a small mismatch loss, a thin high-impedance metamaterial surface was designed. The bandwidth is enlarged by applying non-Foster impedances between the ends of the antenna arms and the conducting surface.

Index Terms – Artificial magnetic conductor, broad band, HF antenna, impedance matching, low profile.

I. INTRODUCTION

The high-frequency (HF) band is attractive for over-the-horizon communication and sensing, due to the reflective properties of the ionosphere at those frequencies. This is especially the case for frequencies in the lower half of the band. Due to the wavelengths involved, e.g., 30 m at 10 MHz, HF antennas tend to be large, and almost always protrude from the structure on which they are mounted. It can be advantageous to integrate the HF antenna with a structure, e.g. for reasons of aerodynamics, detectability or esthetics. For instance, a large unmanned aerial system may require an HF antenna that does not deteriorate its aerodynamics and does not increase its radar signature. However, when an HF antenna is mounted both parallel and close to a conducting surface, the mismatch loss will be large.

The solution presented in this paper makes use of a high-impedance surface. A regular conducting surface has a low impedance, enabling electrons in the surface to react quickly to fields produced by the antenna. This reduces the radiation by orders of magnitude. A high-impedance surface prevents electrons from reacting this way. It can be designed without changing the underlying conducting surface.

The concept of high-impedance surfaces was pioneered by Sievenpiper et al. [1–4] in the late 1990s. The authors explain how the metamaterial surface, which is a conducting surface, does not conduct AC currents or surface waves within a forbidden band, and reflects normal-incidence electromagnetic waves with no phase reversal. The authors show how antennas can be mounted parallel to and close to such a surface without suffering a large mismatch loss. More examples are presented by Best and Hanna [5].

Subsequent researchers have designed many high-impedance surfaces with improved properties, such as compact or broadband designs [6–8]. All these designs exhibit their special properties at microwave frequencies. To the authors' knowledge, no high-impedance surfaces have yet been designed to operate at MHz frequencies, in the HF band.

The design presented here was inspired by [7], but modified significantly to work in the HF band while being thin. With this high-impedance surface, the HF antenna has a small mismatch loss in a 2% bandwidth.

The next challenge is to increase the bandwidth. Visser [9] presents a folded dipole antenna above a high-impedance surface and exploits the fact that a folded dipole offers more degrees of freedom for optimization than an ordinary dipole antenna. The HF antenna presented in this article also takes advantage of additional degrees of freedom offered by a folded dipole, albeit in a different way. In this case, the ground takes the place of the long wire of the folded dipole. The ends of the dipole arms connect to the ground plane. We use the additional design freedom offered by the connections to load the ends of the antenna with an imaginary-valued non-Foster impedance. Sussman-Fort and Rudish [10] explore ways to realize such impedances. With proper loads, the bandwidth can be increased from 2% to 30%.

II. HIGH-IMPEDANCE SURFACE DESIGN AND RESULTS

As mentioned, the design presented here was inspired by [7]. However, it was not accomplished by

Submitted On: July 20, 2024
Accepted On: October 7, 2024

https://doi.org/10.13052/2024.ACES.J.390808

taking an existing microwave design and multiplying the dimensions by two orders of magnitude. The value of a high-impedance surface lies in the fact that it is thin. As will be specified below, our antenna is only 3 cm above the surface, which itself has a thickness of 1 cm. The total thickness of 4 cm is only one thousandth of a wavelength at 7.5 MHz. By comparison, the HF antenna "with extremely low profile" reported in [11] has a rather high profile: it is one meter above its ground plane.

The design process starts by the selection of a suitable geometry concept. Metamaterial surfaces exist in many forms, e.g. coupled patches on one dielectric layer, overlapping patches on multiple layers, with or without vias to the underlying conducting plane. In this case, we have chosen a periodic structure of spirals on one layer, without vias. For a unit cell, geometry and material variables are adjusted to optimize the reflection phase of an incident plane wave at the desired operating frequency. A low-impedance surface imposes the boundary condition that the total tangential electric field be close to zero, which causes the reflection phase to be close to 180 degrees. The surface will be a high-impedance surface to incoming plane waves when the reflection phase is close to zero degrees.

The design shown in Fig. 1 accomplishes this by using a ferrite material with $\mu_r = 400$; $\varepsilon_r = 1$. The thickness is only 10 mm. The unit-cell size is 0.3×0.3 m. The metal trace width is 24 mm and the gap width equals 6 mm. The reflection phase as a function of frequency is shown in Fig. 2. Note that the phase equals zero at 10 MHz, and the $\pm 90^\circ$ bandwidth ranges from 6.77 to 14.95 MHz, which is a bandwidth of about 65%.

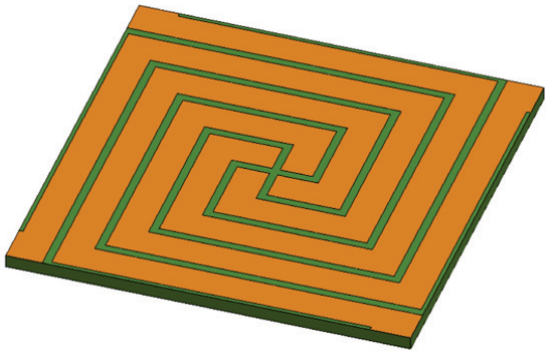

Fig. 1. High-impedance surface unit cell.

The actual high-impedance surface was constructed as a 53×5 array of unit cells, a small part of which is shown in Fig. 3.

With this high-impedance surface, the HF antenna has a small mismatch loss in a 2% bandwidth. This is much less than the bandwidth suggested in Fig. 2, but that was for an incoming plane wave. With an antenna close to the surface, the fields are quite different from a plane wave, to the extent that our design approach was not guaranteed to work. The antenna is mounted 30 mm above the structure; this is one-thousandth of a wavelength at 10 MHz. The antenna arms are metal traces with a width of 4 mm. The ends of the arms are connected to the ground plane by metal strips that pass through a gap between spirals without touching the spirals. The return loss is shown in Fig. 4 for a source impedance of 50 Ω.

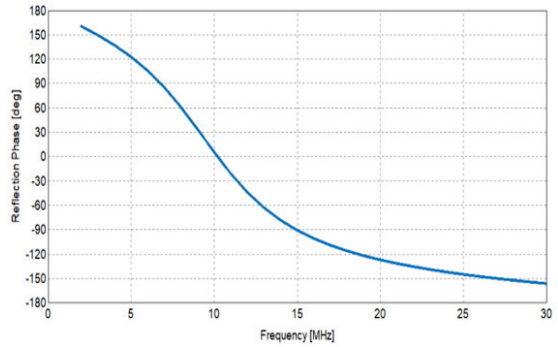

Fig. 2. Reflection phase of a normally-incident plane wave on the high-impedance surface.

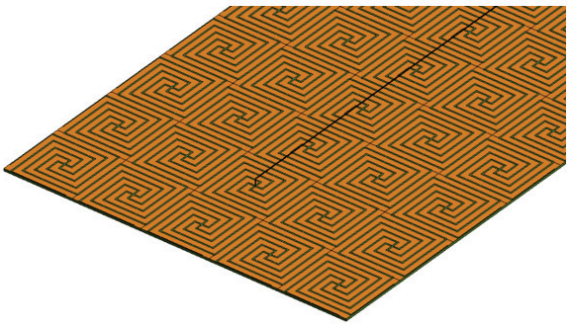

Fig. 3. Part of the high-impedance surface with the antenna.

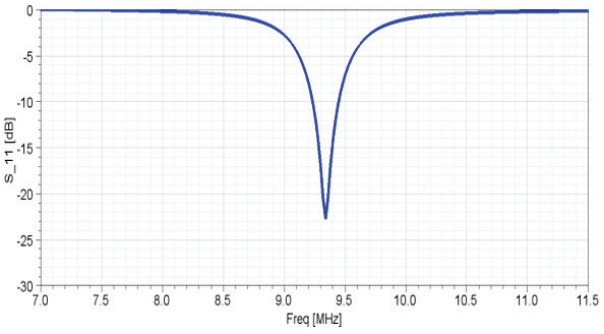

Fig. 4. Reflection coefficient of the dipole with electrically shorted arms over the high-impedance surface.

III. COMPUTATIONAL METHODS

For the 3D simulations of the antenna and the high-impedance surface, the Finite Element Method was used, as implemented in Ansys HFSS, part of Ansys Electronics Desktop [12]. Two advantages of this Finite-Element implementation stand out: automatic adaptive mesh refinement and hierarchical basis functions. Thanks to these, it was possible to run the simulation on one computer with a memory capacity of 128 GB. The automatic adaptive mesh refinement ensures that the final mesh is fine enough where needed, while it remains coarser where this is possible. The hierarchical basis functions enable an iterative solution in which a solution with zero-order basis functions serves as an initial guess for an iterative solution with first-order basis functions.

The computational domain was a cylindrical air volume around the structure, with the antenna close to the cylinder axis, and a radius of 10 m, which corresponds to a quarter wavelength at 7.5 MHz. The air volume was terminated by an Absorbing Boundary Condition. Although more-advanced techniques such as Perfectly Matched Layers and the Finite-Element Boundary-Integral method could be used to reduce the size of the air volume, this was not necessary in this case because the volume in terms of cubic wavelengths was modest. The motivation for a cylindrical volume was that radiated fields would meet the boundary at angles almost normal to their propagation direction. Absorbing boundary conditions are most effective at those angles.

The peak memory requirement was 109 GB for a Finite-Element matrix equation with 33 million unknowns. The maximum CPU time for one frequency sample was 2 hours 13 minutes. Thanks to parallel processing on 16 cores, the maximum elapsed wall-clock time for one frequency sample was 24 minutes and 14 seconds. A discrete frequency sweep, e.g. from 5 to 12 MHz, typically consisted of 71 samples.

IV. NON-FOSTER LOAD DETERMINATION AND RESULTS

Figure 5 shows the input impedance Z_{11} of the design of the previous section. Note that the real part of Z_{11} is not far from 50 Ω over an appreciable bandwidth while the imaginary part of Z_{11} varies much more with frequency. Therefore, we will interrupt the short circuits at the ends of the antenna arms and insert imaginary-valued impedances, such that the imaginary part of the antenna input impedance be close to zero over a large band.

Long and Sievenpiper have explored the use of non-Foster circuits in relation with high-impedances surfaces [13], but they loaded the periodic surface features rather than the antenna. They have managed to bring the operating frequency of an antenna with a thin high-impedance surface down to the UHF band, and explain why achieving such a design is a challenge. This underscores that achieving the same in the HF band (an order of magnitude lower) is exceptional.

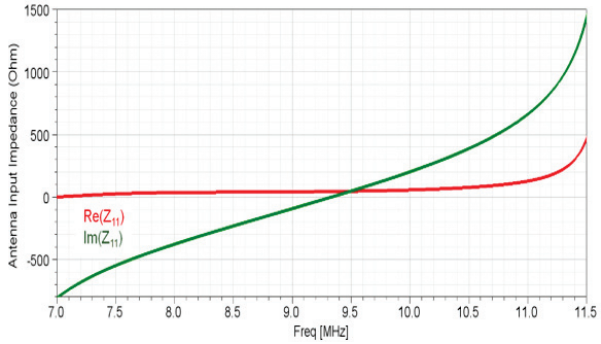

Fig. 5. Real and imaginary parts of antenna input impedance as a function of frequency.

The most efficient workflow to determine the aforementioned impedances at the ends of the antenna arms involves rapid optimization in a circuit simulator. First, in the 3D electromagnetic simulation model, ports were placed in the locations where the impedances would be inserted later, between the ends of the antenna arms and the ground plane. Together with the feed port already present, this resulted in a three-port device. Frequency-dependent S-matrices were determined with a 3D full-wave simulation. Figure 6 shows how the S-parameter representation of the model was used in the circuit simulator in the Ansys Electronics Desktop, where a source and passive electric components were connected to the S-parameter block.

Figure 6 shows two equivalent implementations, both featuring the same three-port HFSS model. The top schematic has one pin per port; the bottom schematic has two pins per port. Behind the scenes, the S-parameter block contains all necessary information. In the schematic with one pin per port, the use of multiple ground symbols may seem non-intuitive, as this could enforce, in some circuit simulators, an unphysical zero-L, zero_R connection between two distance locations in the 3D structure. In the Ansys Electronics Desktop, the ground symbol merely indicates a connection to the second terminal on the same port. This has been verified with the bottom schematic, in which the connections to the second terminal on each port have been made explicit.

In the circuit simulator, simulations take only a fraction of a second. Thus, the desired impedance values could be determined rapidly.

These impedance values, which are imaginary-valued, are shown in Fig. 7. They are non-Foster impedances that follow a smooth curve with a nega-

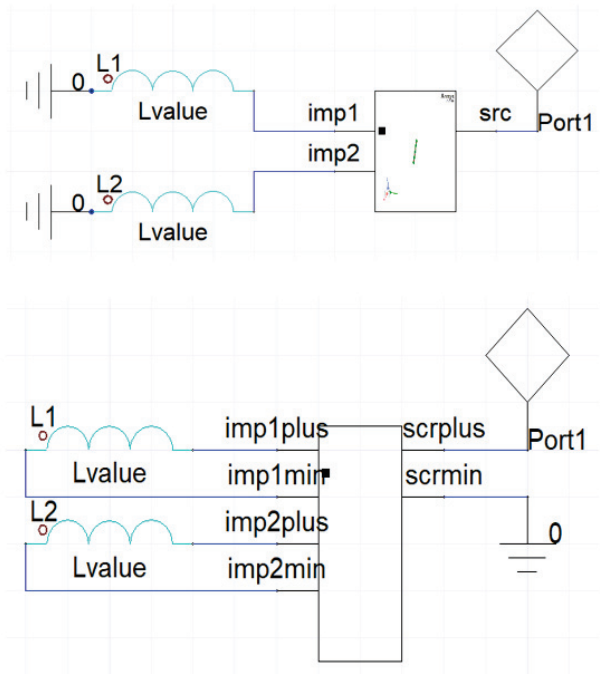

Fig. 6. Two equivalent implementations of the HFSS three-port device (rectangular symbol) as part of the circuit, with impedances to be optimized.

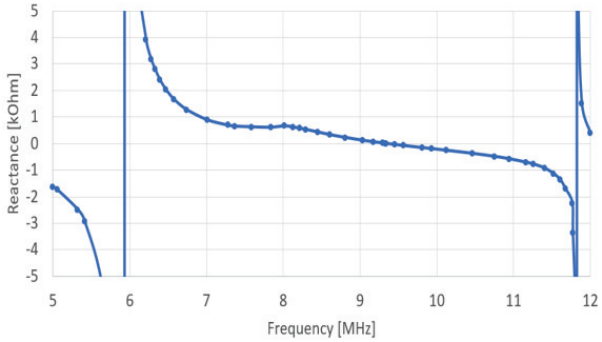

Fig. 7. Reactance values at the ends of the antenna arms required to negate the imaginary value of antenna input impedance.

tive slope between 5.9 and 11.8 MHz. The behavior near 8 MHz might be related to the effective electrical length of the spirals on the ferrite substrate. How to realize these impedances is still a topic of research, about which Sussman-Fort and Rudish [10] as well as Long and Sievenpiper [13] offer valuable information.

Figure 8 shows the resulting antenna input impedance Z_{11} when these non-Foster impedances are added. Note that the modification brought the imaginary part of Z_{11} to zero, as intended, but has affected the real part of Z_{11}.

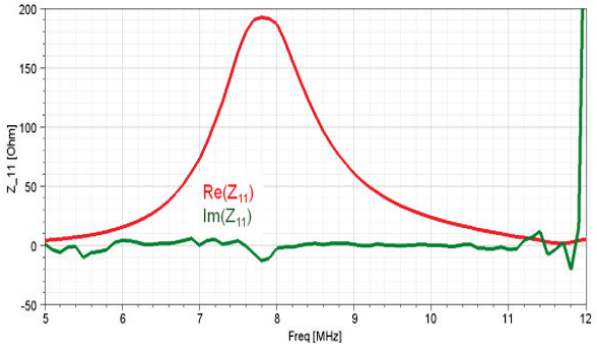

Fig. 8. Antenna input impedance after adding the impedances of Fig. 7 between the ends of the antenna arms and the ground plane.

The resulting return loss S_{11} depends on the source impedance. Figure 9 shows the return loss when the source impedance equals 100 Ω. Note that the -10 dB bandwidth is almost 30%.

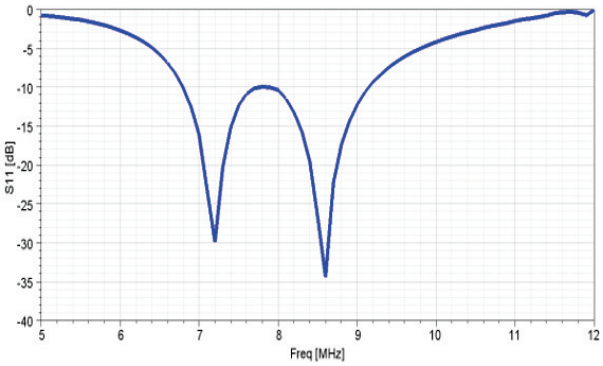

Fig. 9. Reflection coefficient when the source impedance equals 100 Ω.

Furthermore, operating frequencies outside this band are easily reached with different source impedances. With a 50 Ω source impedance, the minima move about 1 MHz farther apart, enabling operation at lower and higher frequencies, while S_{11} reaches a local maximum of -5 dB between those frequencies. With a 25 Ω source impedance, this trend continues. Figure 10 shows the return loss for the three source impedances. Note that the lower and upper operating bands offer generous -10 dB bandwidths of 13-14%.

Finally, Fig. 11 shows the antenna pattern at 9.3 MHz. Since the high-impedance surface is narrow relative to the wavelength, the antenna pattern is similar to that of the dipole antenna. However, due to the connections at the ends of the arms, the peak gain is slightly higher than that of a dipole antenna.

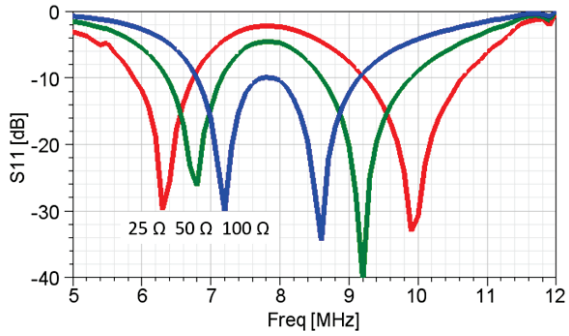

Fig. 10. Return loss with various source impedances, which makes lower and higher frequencies easily attainable.

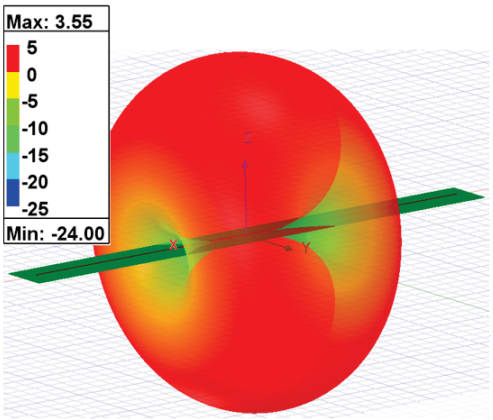

Fig. 11. Gain [dBi] of the antenna with high-impedance surface.

V. CONCLUSION

An HF antenna has been made to operate when mounted parallel and close to a conducting surface. This was achieved with a thin high-impedance metamaterial surface. To the authors' knowledge, such a structure had not yet been designed for HF antennas. The bandwidth was enhanced by adding imaginary-valued impedances between the ends of the antenna arms and the conducting surface. The design of these non-Foster impedances is still a topic of research.

REFERENCES

[1] D. Sievenpiper, L. Zhang, and E. Yablonovitch, "High-impedance electromagnetic ground planes," in *IEEE MTT-S Int. Microwave Symp. Dig*., Anaheim, CA, vol. 4, pp. 1529-1532, June 1999.

[2] D. Sievenpiper, Lijun Zhang, R. F. J. Broas, N. G. Alexopolous, and E. Yablonovitch, "High-impedance electromagnetic surfaces with a forbidden frequency band," *IEEE Trans. Microwave Theory Tech*., vol. 47, no. 11, pp. 2059-2074, Nov. 1999.

[3] D. Sievenpiper, R. Broas, and E. Yablonovitch, "Antennas on high-impedance ground planes," in *1999 IEEE MTT-S Int. Microwave Symp. Dig.,* Anaheim, CA, vol. 3, pp. 1245-1248, June 1999.

[4] R. F. J. Broas, D. F. Sievenpiper, and E. Yablonovitch, "A high-impedance ground plane applied to a cellphone handset geometry," *IEEE Trans. Microwave Theory Tech.*, vol. 49, no. 7, pp. 1262-1265, July 2001.

[5] S. R. Best and D. L. Hanna, "Design of a broadband dipole in close proximity to an EBG ground plane," *IEEE Antennas and Propagation Magazine*, vol. 50, no. 6, pp. 52-64, Dec. 2008.

[6] S. Raza, M. A. Antoniades, and G. V. Eleftheriades, "A compact low-profile high-impedance surface for use as an antenna ground plane," in *IEEE Int. Symp. Antennas and Propagation (APSURSI)*, Spokane, WA, pp. 1832-1835, July 2011.

[7] A. Bellion and M. Cable, "A new wideband and compact High Impedance Surface," in *15 Int. Symp. Antenna Tech. and Applied Electromagnetics (ANTEM)*, Toulouse, France, pp. 1-5, June 2012.

[8] H. Mirshahram and W. Qun, "Meander line-based high impedance surface with high angular stability of resonant frequency," in *3rd IEEE Int. Symp. Microwave, Antenna, Propagation and EMC Technologies for Wireless Communications*, Beijing, China, pp. 1246-1249, Oct. 2009.

[9] H. J. Visser, "Printed folded dipole antenna design for rectenna and RFID applications," in *7th European Conference on Antennas and Propagation (EuCAP)*, Gothenburg, Sweden, pp. 2852-2855, Apr. 2013.

[10] S.E. Sussman-Fort and R.M. Rudish, "Non-Foster impedance matching of electrically-small antennas," *IEEE Trans. on Antennas Propagat.,* vol. 57, no. 8, pp. 2230-2241, Aug. 2009.

[11] W. Lin and Z. Shen, "Broadband horizontally polarized HF antenna with extremely low profile above conducting ground," in *2013 IEEE Antennas and Propagation Society International Symposium (APSURSI),* Orlando, FL, pp. 688-689, July 2013.

[12] Ansys Electronics Desktop, version 2024 R1, ANSYS, Canonsburg, PA, 2024.

[13] J. Long and D. F. Sievenpiper, "Low-profile and low-dispersion artificial impedance surface in the UHF band based on non-Foster circuit loading," in *IEEE Trans. on Antennas Propagat.*, vol. 64, no. 7, pp. 3003-3010, July 2016.

Marius (Martin) H. Vogel obtained his M.Sc. in Physics at Leiden University in the Netherlands, and worked at TNO Defense and Security, a Dutch defense contractor. Due to the nature of the research, he obtained a Ph.D. in electromagnetics from Delft University of Technology at that time. A one-year assignment on directed-energy weapons at the US Air Force Lab in Albuquerque, NM brought him to the USA.

He has worked at Ansoft /ANSYS, and later at Altair Engineering, both in the USA, in various roles on a wide variety of applications in high-frequency electromagnetics, propagation and communication. Applications include antenna design, antenna placement, radar cross section, electromagnetic interference, bioelectromagnetics, signal integrity and more. Martin joined GTRI in April 2023 and is based in the Hampton Roads area in Virginia.

Mark H. Smith has over 40 years of experience in RF, microwave, and optical technology and applications, with over 30 years of experience at GTRI conducting and directing research, concept development, analysis, computer modeling, capability development, and testing, with a primary focus on technology and systems for RF sensing and Electronic Warfare. He has been Chief Scientist of GTRI's Sensors and Electromagnetic Applications Laboratory (SEAL) since 2012. Dr. Smith received his Ph.D. from Georgia Institute of Technology (GA Tech) in 2002, an M.S. from GA Tech in 1987, and a B.E.E. With Highest Honor from GA Tech in 1982.

Effect of Cotton and Wool Fabrics on the Accuracy of Electromagnetic Dosimetry Analysis Due to Millimeter Wave Exposures

Fatih Kaburcuk

Department of Electrical-Electronics Engineering
Sivas University of Science and Technology, Sivas 58100, Turkiye
fkaburcuk@sivas.edu.tr

Abstract – With the development of wireless communication, satellite, and radar technologies operated at millimeter wave (MMW) frequency range, it is essential to consider the adverse health effects of the radiated electromagnetic (EM) fields at MMW frequency. In most EM dosimetry analyses for the human body models, bare human models have been considered. However, the presence of fabrics such as cotton and wool on the human body can affect the accuracy of the EM dosimetry analysis. At the MMW frequency range, the effect of fabrics on EM dosimetry analysis in a human body model has not been extensively investigated using the finite-difference time-domain (FDTD) method. In this study, the effects of fabrics on the human body on the power transmission coefficient, specific absorption rate, absorbed power density, and heating factor due to EM MMW exposure are investigated using the FDTD method. Numerical results show that the thickness of the fabrics and air gap introduced between the fabrics and the skin surface significantly affects the accuracy of EM dosimetry analysis at the frequency range 1-100 GHz.

Index Terms – Absorbed power density, electromagnetic exposure, fabric effects, FDTD method, heating factor, millimeter wave, SAR.

I. INTRODUCTION

With the development of 5G and 6G wireless communication, satellite, and radar technologies, which require high data speeds and secure communication, the use of millimeter wave (MMW) frequencies [1–4] has increased significantly. Devices operated at MMW frequency range radiate electromagnetic (EM) fields that comply with EM field exposure limits for human safety determined by international guidelines. These guidelines are defined by the International Commission on Non-Ionizing Radiation Protection (ICNIRP) [5] and the IEEE International Committee on Electromagnetic Safety (IEEE-ICES) [6].

Below 6 GHz, IEEE and ICNIRP guidelines recommend basic restrictions which are specific absorption rate (SAR) over 1-gram and 10-gram tissues and incident power density (IPD) for EM field exposure limits. In the frequency range 6-300 GHz, the basic restrictions and limitations determined by the guidelines are absorbed power density (APD), IPD, and whole-body average SAR for a given IPD.

Interaction between the human body and EM field exposure generated by far-field and near-field sources has been extensively investigated in [7–23] at different frequency of interest. In most studies [7–18], human body models with bare skin have been used for EM dosimetry analysis at below and above 6 GHz. However, electromagnetic power absorption by biological tissues can be affected by the presence of fabrics on the human body [19–23]. Power transmission coefficients (PTC) [19] in the presence of a fabric on the skin surface with and without an air gap between the fabric and skin surface have been analytically calculated up to 300 GHz. Therefore, it is important to consider the impact of fabrics on the accuracy of EM dosimetry analysis, especially at MMW frequency range. In several studies [1, 2, 19–23], the effect of fabrics on the human body has been investigated due to EM field exposure at MMW frequencies, and it could be concluded that the presence of fabric on the human body acts as impedance matching layers affecting EM field absorption. The effects of most common fabrics, cotton and wool, on APD, PTC, and temperature rise of a one-dimensional (1D) four-layered model are investigated in [20] using the finite element method (FEM) due to EM far-fields exposure and in [20] using CST software employing the finite integration technique (FIT) at 26 GHz and 60 GHz. The effect of fabrics on the human body for body centric communication has been studied in terms of path gain at 60 GHz in [21]. Two-dimensional (2D) clothed skin models with cotton and wool fabrics experiencing EM field exposure with oblique incident angle at 60 GHz in [22] and over the frequency range from 20 GHz to 100 GHz in [23] have been investigated using Monte Carlo simulations. However, to the best of our knowledge, 1D clothed multilayered human body models exposed to an EM field at

Submitted On: April 22, 2024
Accepted On: October 17, 2024

https://doi.org/10.13052/2024.ACES.J.390809

MMW frequency range have not been investigated using the finite-difference time-domain (FDTD) method.

The FDTD method has been widely used in EM dosimetry analysis of three-dimensional (3D) human body voxel models without clothing. However, it is difficult to create 3D clothed human body voxel models for EM dosimetry analysis based on the FDTD method, especially at MMW frequency range. Therefore, a 1D multi-layered head model obtained from a realistic head voxel model as in [11] can be used in EM dosimetry analysis using the FDTD method based on the Debye model to show the effect of different fabric materials on the EM field exposure metrics at wide range of frequencies from 1 GHz to 100 GHz.

In this study, a 1D multi-layered head model clothed with cotton or wool fabrics is analyzed using the FDTD method based on the Debye model to show the effect of fabrics in the human body over the frequency range from 1 GHz to 100 GHz. Furthermore, the effect of fabric thickness and effect of an air gap between the fabrics and the skin surface in the 1D multi-layered model on the accuracy of EM dosimetry analysis are investigated using the FDTD method at frequencies up to 100 GHz. Numerical results obtained in this study show that PTC, APD, and heating factor based on the temperature rise and APD in the 1D multi-layered model are significantly affected by the presence and thickness of fabrics and air gap.

II. METHOD AND MODELS

A. 1D multi-layered model and fabrics

A 1D multi-layered model extracted from the forehead region of 3D realistic human head model [24] shown in Fig. 1 (a) is used in the EM dosimetry analysis. The tissue arrangement and thicknesses in the 1D multi-layered model, shown as dashed lines in Fig. 1 (b), are shown in Fig. 1 (c).

The 1D multi-layered forehead model in Fig. 1 (b) covered by cotton/wool fabrics, such as a hat, is used in this study to show the effect of clothing on EM dosimetry analysis. The complex relative permittivity $[\varepsilon_r^*(\omega)]$ of the cotton and wool, which are $2 - j0.04$ and $1.22 - j0.036$, respectively, are given in [20]. The thickness of fabrics (t_{fabric}) varies from 0.5 mm to 3 mm or more. The thickness of air gap (t_{air}) between the fabric and the skin surface varies from 0 mm to several mm.

B. FDTD method based on the Debye model

The FDTD method mostly used in the EM dosimetry analysis provides solutions at a wide range of frequencies when the Debye model [25, 26] is integrated into the FDTD method to analyze frequency-dependent biological tissues as in [10, 11]. The three-term Debye parameters (ε_∞ relative permittivity at infinite frequency, ε_k static relative permittivity, and τ_k relaxation time at

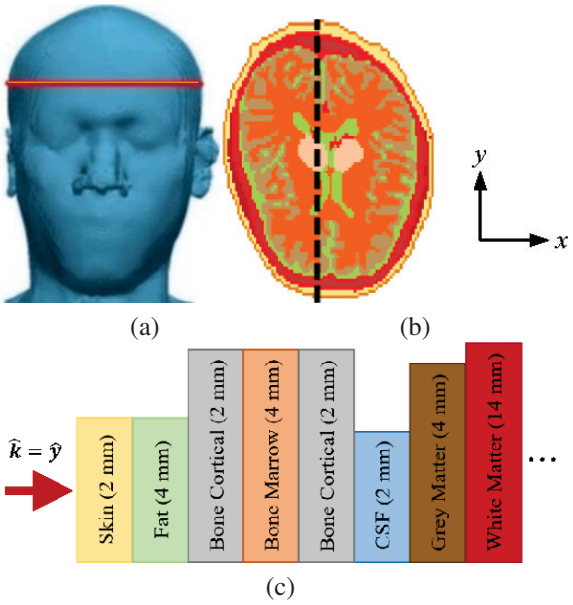

Fig. 1. (a) 3D human head model [24] (red band shows the 2D cross sectional of forehead region), (b) 1D multi-layered forehead model (black dashed line), and (c) types of tissues and their thickness in the 1D model.

k^{th} term) of head tissues provided in [27] are used in the Debye model to obtain solutions up to 100 GHz. These Debye parameters were obtained from a numerical procedure presented in [28] and provide EM solutions at frequencies up to 100 GHz in a single FDTD simulation:

$$\varepsilon_r^*(\omega) = \varepsilon_r' + j\varepsilon_r'' = \varepsilon_\infty + \sum_{k=1}^{3} \frac{\varepsilon_k - \varepsilon_\infty}{1 + j\omega\tau_k}. \quad (1)$$

In the FDTD method, cell size is set to 0.0625 mm which satisfies the Courant-Friedrichs-Lewy (CFL) condition [26]. The FDTD computational domain is terminated by 10-cell convolution perfect matched layers (CPML) with 15-cell air layers. A Gaussian waveform considered as an incident plane wave including all frequency of interest up to 100 GHz is generated on the total-field scattered-field (TF-SF) boundary [26] to excite the FDTD computational domain. The IPD of the incident plane wave based on the public exposure scenario in the ICNIRP guideline [5] is set to 5 W/m^2 at 1 GHz and 10 W/m^2 over the frequency range from 2 GHz to 100 GHz.

C. Calculations of power transmission coefficient, SAR, absorbed power density, and heating factor

In order to evaluate transmission from air to skin tissue, the power transmission coefficient (PTC) is calculated by dividing the total power deposition (TPD) by the IPD. The TPD of the 1D model is expressed in [29] as:

$$TPD = \frac{1}{2}\int_{i=0}^{i_{max}} \sigma_i |E_i|^2 \mathrm{d}i, \quad (2)$$

where i_{max} is larger than penetration depth in the 1D model, and E_i [V/m] and σ_i [S/m] are the electric field strength and the electric conductivity of the i^{th} indexed cell of the tissues, respectively. The APD [30] for 1D multi-layered models can be expressed as:

$$\mathrm{APD}_i = \frac{|E_i|^2}{|\eta|}, \tag{3a}$$

where:

$$|\eta| = \eta_o \sqrt{\frac{\mu_r}{\varepsilon_r'[1+(\varepsilon_r''/\varepsilon_r')]^{0.25}}}, \tag{3b}$$

where η_o is the characteristic impedance in free space and μ_r is the relative permeability of a material. The SAR defined in [5, 6] is calculated to determine how much EM power is absorbed per unit mass of tissues:

$$SAR(i) = \frac{\sigma_i}{2\rho}\left(|E_i|^2\right), \tag{4}$$

where ρ is the mass density of the tissues.

The temperature rise distribution in the 1D multi-layered model due to EM field exposure has been calculated by using the Pennes bioheat equation [31]. This equation can be solved using the finite-difference approximation as follows:

$$T^{n+1}(i) = T^n(i) + \frac{\Delta t}{C}\cdot\left[\mathrm{SAR}\,(i) - \frac{B}{\rho}\cdot[T^n\,(i) - T_b] + \frac{K}{\rho\cdot\Delta^2}\cdot[T^n(i+1)+T^n(i-1)-2\cdot T^n(i)]\right], \tag{5}$$

where C [J/(kg·°C)], K [W/(m·°C)], and B [W/(m^3·°C)] are the heat capacity, the thermal conductivity, and the blood perfusion rate, respectively, and Δ is the resolution of 1D multi-layered model. T^n (i) is the temperature [°C] at time n and at i^{th} indexed cell, and T_b is the blood temperature [°C] set to 37°C. The thermal increment (Δt) for the iterative calculation of equation (5) must satisfy the thermal stability numerically:

$$\Delta t \le \frac{2\cdot\rho\cdot C\cdot\Delta}{12\cdot K + B\cdot\Delta^2}. \tag{6}$$

The convection boundary condition for a clothed 1D model without an air gap can be solved using the finite difference approximation as implemented in [10, 11]. However, the boundary conditions in the presence of an air gap between the fabric and skin surface can be considered in [32, 33] as a closed enclosure. The convective boundary condition is expressed as:

$$T^{n+1}(i_{min}) = \frac{K\cdot T^{n+1}(i_{min}+1) + T_{air}\cdot H\cdot\Delta}{K + H\cdot\Delta}, \tag{7}$$

where T_{air} is the air temperature set to 20°C, n is the unit normal vector to the interfaces, and H is the convection heat transfer coefficient of 10.5 [W/(m^2·°C)]. The mass density and thermal parameters of the tissues used here are provided in [34]. The steady-state temperature distribution in the human body model is calculated when SAR = 0. Then, the final temperature rise distribution is computed by solving the bioheat equation again when SAR $\neq$ 0. Finally, the temperature rise distribution is difference of the steady-state and final temperature distributions.

The heating factor, defined as the steady-state temperature rise divided by APD, is calculated as a function of frequency up to 100 GHz. The heating factor is a useful assessment of thermal effect due to EM wave exposure at frequencies above 6 GHz. Above 6 GHz, the maximum heating factor should be at most 0.025 [°C·m^2/W] based on [13].

III. NUMERICAL RESULTS

To verify the validity of the FDTD method based on the Debye model, the 1D multi-layered forehead bare model is analyzed to obtain APD and local SAR values at 60, 77, and 100 GHz when IPD is 10 W/m^2. In Table 1, the maximum values of APD and local SAR of the 1D human forehead model are compared with the results presented in [1, 14, 19]. The results obtained in this study are in good agreement with the published results, despite analyzing different multi-layered models. The 1D multi-layered models clothed with cotton/wool fabrics of different thickness (t_{fabric}) in contact with the skin surface ($t_{air} = 0$) are analyzed in this study to calculate the PTC and APD values at 60 GHz for IPD of 10 W/m^2. For comparison, Table 2 shows the results obtained in this study and obtained using FEM in [20].

Table 1: Max. APD and local SAR values at different frequencies of interest for IPD of 10 W/m^2

Models	Freq. [GHz]	Max. APD [W/m^2]	Max. SAR [W/kg]
[1]	60	6.2	26.0
[19]		5.9	27.6
This study		6.2	20.6
[14]	77	N/A	27.2
This study		6.5	25.4
[14]	100	N/A	33.9
This study		6.9	29.3

Table 2: PTC and max. temperature rise at 60 GHz

Cotton (mm)	Models	TPC	APD
1	[20]	0.79	7.8
	This study	0.78	7.8
2	[20]	0.72	6.4
	This study	0.63	6.4
3	[20]	0.77	6.3
	This study	0.65	6.4

A. Effect of cotton/wool thickness on EM exposure metrics

The effects of cotton/wool thickness in contact with skin surface in the 1D multi-layered forehead models

are analyzed using the FDTD method over the frequency range up to 100 GHz. PTCs of the 1D bare and clothed models with cotton/wool fabrics of 1, 2, and 3 mm thickness are calculated and shown in Fig. 2 as a function of frequency. It can be realized that power transmission between the fabrics and skin surface is significantly affected by the fabric type and thickness, and the frequency of EM field exposure. As frequency changes, there may be an oscillation in power transfer to the skin surface. PTCs for clothed models in Fig. 2 have maxima and minima at certain frequencies because the fabric acts as impedance matching layers. In PTC values for the 3 mm thick cotton, the first highest occurs at a frequency of 17 GHz, where the thickness of cotton is equal to $t_{fabric} = \lambda_f/4$ [19] where λ_f is the wavelength in the fabrics. Similarly, other maxima of PTC occur at frequencies of 51 and 85 GHz when $t_{fabric} = 3\lambda_f/4$ and $t_{fabric} = 5\lambda_f/4$, respectively. It can be deduced that peak values of PTCs appear at frequencies where the thickness of fabrics is equal to odd multiples of $\lambda_f/4$ [19] and expressed as:

$$t_{fabric} = (2n+1)\frac{\lambda_f}{4} = (2n+1)\frac{\vartheta_p}{4f}, \qquad (8)$$

where ϑ_p is phase velocity in the fabrics, f is the frequency of the EM field, and n is an integer number. In Table 3, frequencies calculated from equation (8) and obtained from Fig. 2 are the frequencies at which peak power absorption occurs for different thicknesses of the cotton and wool fabrics. The frequencies obtained from Fig. 2 are in good agreement with those obtained from exact calculation in equation (8). Additionally, it can be seen from Fig. 2 that PTC values below 10 GHz are not affected by the presence of fabrics because the thickness of fabrics is smaller than the wavelengths of the EM waves at frequencies below 10 GHz.

Figure 3 shows the PTCs of 1D models clothed with cotton fabric as a function of its thickness at frequencies of 30, 60, and 100 GHz. In Fig. 3, the maximum PTC values for each frequency of interest occurs when the cotton thickness is equal to odd multiples of $\lambda_f/4$ in equation (8). Table 4 shows the cotton thickness at which PTC values are maximum at 30, 60, and 100 GHz, calculated from equation (8) and obtained from Fig. 3. The cotton thickness calculated using equation (8) and obtained from Fig. 3 are in acceptable agreement.

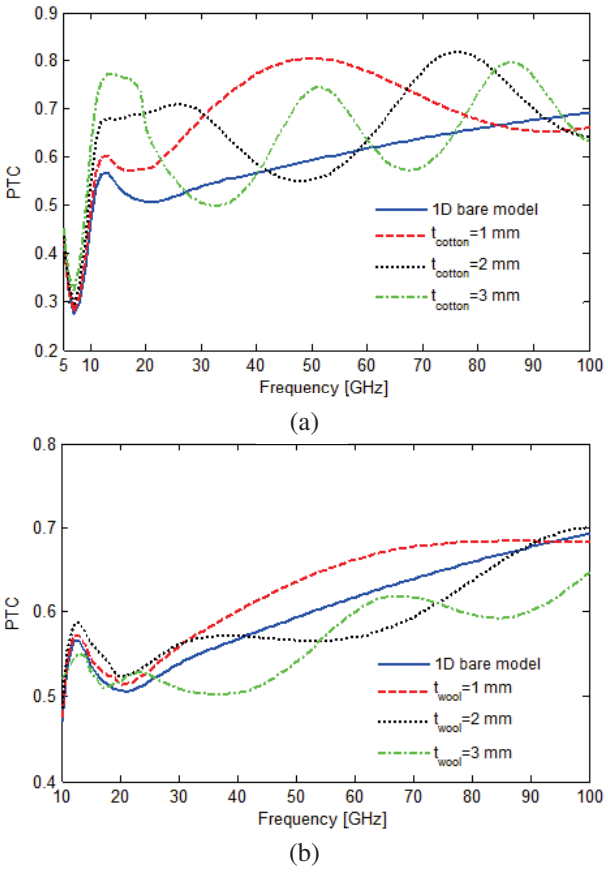

Fig. 2. PTCs of bare and clothed 1D multi-layered forehead models with different thickness of (a) cotton (t_{cotton}) and (b) wool (t_{wool}) fabrics when $t_{air} = 0$.

Table 3: Frequencies for peak PTCs in Fig. 2 and calculated from equation (8) for fabrics with different thickness

Models	Thickness [mm]	Exact Freq. in (8) [GHz]	Freq. in Fig. 2 [GHz]
Cotton	1	53.03	51
	2	26.51/79.55	26/77
	3	17.68/53.03/88.38	17/51/85
Wool	1	67.9	74
	2	33.95	34
	3	22.63/67.90	23/68

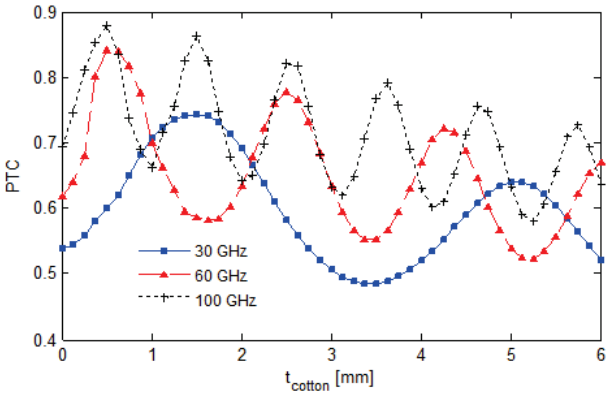

Fig. 3. PTCs at 30, 60, and 100 GHz as a function of t_{cotton} for the 1D multi-layered forehead models clothed with cotton fabric when $t_{air} = 0$.

Table 4: Cotton thickness for peak PTCs in Fig. 3 and calculated from equation (8) at 30, 60, and 100 GHz

Freq. [GHz]	Exact Thickness in (8) [mm]	Thickness in Fig. 3 [mm]
30	1.8/5.3	1.5/5.125
60	0.88/2.7/4.4	0.625/2.5/4.25
100	0.53/1.6/2.7/3.7 /4.8/5.8	0.5/1.5/2.5/3.625 /4.625/5.75

Heating factors for cotton and wool fabrics with the thickness of 1, 2, and 3 mm are shown in Fig. 4 over the frequency range up to 100 GHz. The calculated heating factors are compared to those obtained for a 1D multi-layered bare model presented here and a simple 1D bare model presented in [12]. The heating factors are frequency-dependent below 30 GHz, whereas they are little affected by frequency changes above 30 GHz. They are significantly affected by the thickness of the fabric and not so much by the type of fabric.

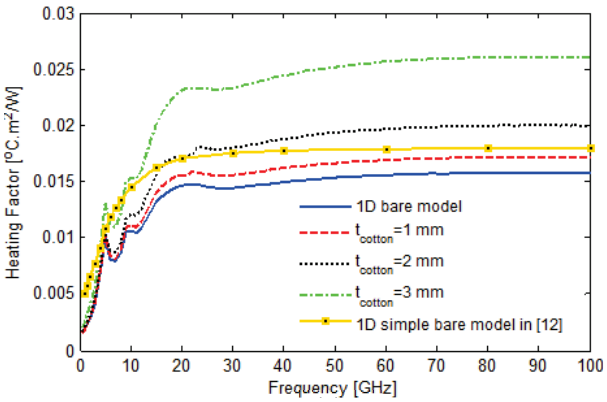

(a)

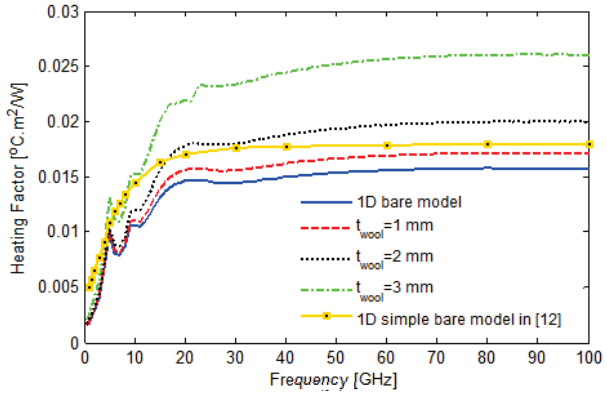

(b)

Fig. 4. Heating factors of the bare and clothed 1D models with different thickness for (a) cotton (t_{cotton}) and (b) wool (t_{wool}) fabrics when $t_{air} = 0$.

The frequency-dependent local SAR values are calculated for the 1D multi-layered forehead model clothed with cotton/wool fabrics having different thicknesses when $t_{air} = 0$. Peak local SAR values for clothed with different thickness and bare 1D multi-layered models are shown in Fig. 5 as a function of frequency. From Fig. 5, peak SAR values of 1D models, especially at frequencies above 20 GHz, are affected by the presence of fabrics and their thickness on the 1D model. It can be realized from Figs. 2 and 5 that the frequencies at which the maxima and minima values in the PTC curves occur are the same as the frequencies at which the maximum and minimum values occur in the SAR curves.

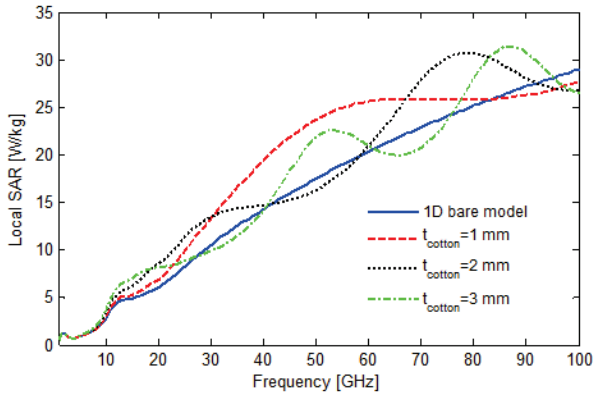

(a)

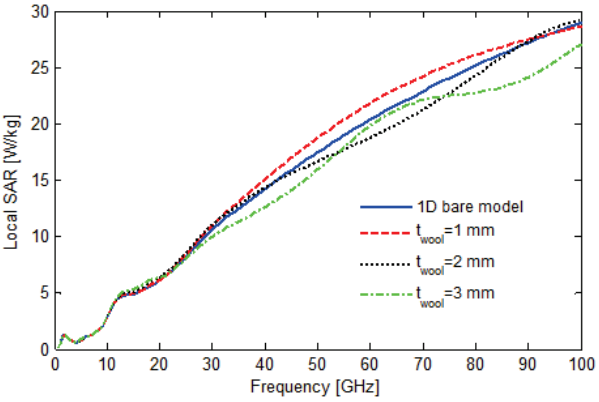

(b)

Fig. 5. Peak local SAR of bare and clothed 1D models for different thickness of (a) cotton and (b) wool fabrics when $t_{air} = 0$.

B. Effect of air gap thickness between fabrics and skin surface

To demonstrate the effects of different thickness for an air gap between fabric and skin surface on the EM field absorption, 1D multilayer forehead models clothed with 1 mm thick cotton/wool fabrics in the presence of an air gap with different thicknesses ($t_{air} = 0, 1, 2, 3$ mm)

are analyzed up to 100 GHz. PTCs for the different thickness of air gap in the 1D multi-layered model are shown in Fig. 6. It can be seen from Fig. 6 that PTCs of clothed 1D models are increasing and decreasing in the presence of the air gap over the frequency range. The air gap and fabrics act as impedance matching layers between the fabrics and the skin surface, and they create fluctuations over the frequency band. Cotton fabric causes larger fluctuations in the PTC values over the frequency band due to its higher relative permittivity compared to the permittivity of wool fabric. In Fig. 7, the PTCs of the 1D model clothed with 1 mm thick cotton at frequencies of 30, 60, and 100 GHz are shown as a function of air gap thickness. From Fig. 6, it can be noticed that PTC values are significantly affected by the change of thickness of the air gap between the fabric and the skin surface.

Heating factors of the 1D multi-layered models clothed with 1 mm thick cotton and an air gap of 1, 2, and 3 mm thickness are shown in Fig. 8. At the frequency band above 10 GHz, heating factors for cotton fabric are slightly higher than those for wool fabric due to having higher relative permittivity of the cotton fabric.

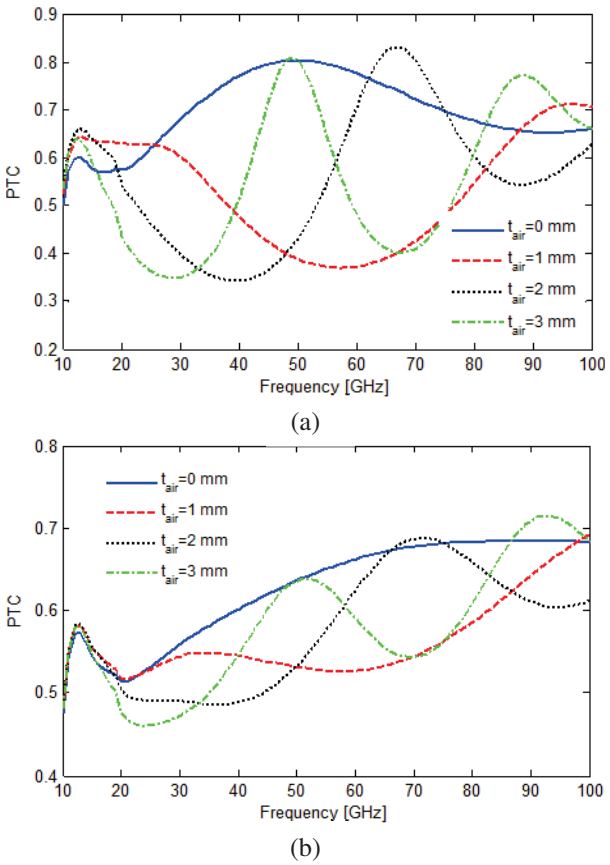

Fig. 6. PTCs of the 1D model clothed with 1 mm thick (a) cotton and (b) wool fabrics when $t_{air} = 0, 1, 2, 3$ mm.

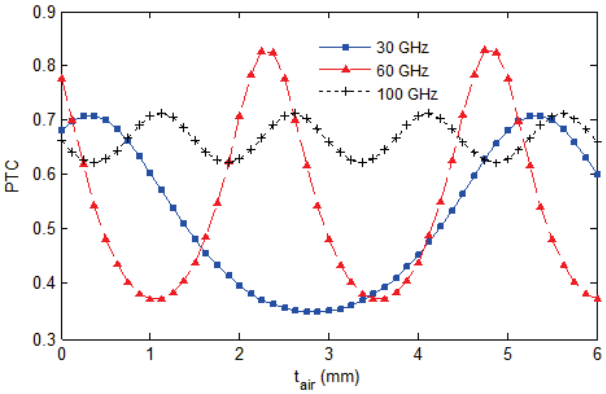

Fig. 7. PTCs at 30, 60, and 100 GHz as a function of t_{air} for 1 mm thick cotton.

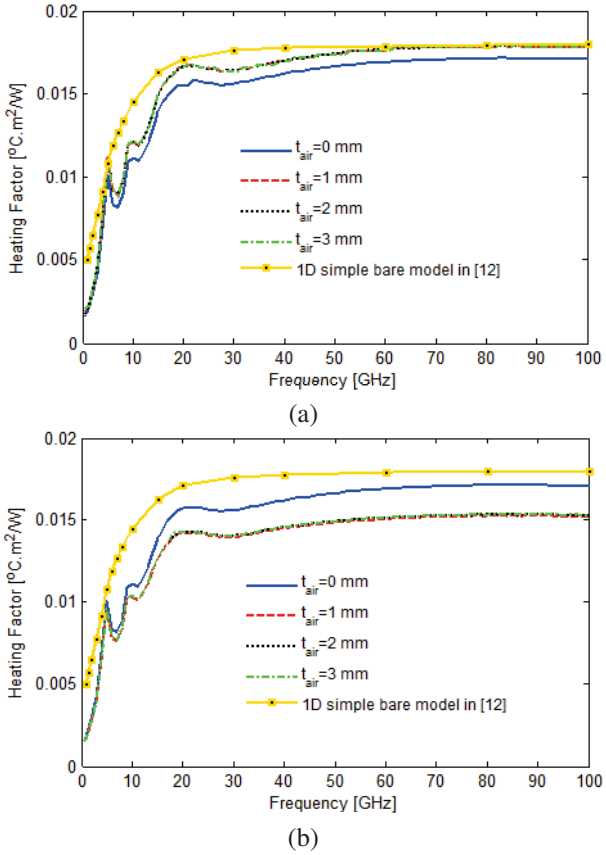

Fig. 8. Heating factors of 1D models with 1 mm thick (a) cotton and (b) wool fabrics when $t_{air} = 0, 1, 2, 3$ mm.

They are not affected by the presence of an air gap larger than 1 mm thick.

The peak values of local SAR over the frequency band are shown in Fig. 9 for clothed 1D multi-layered model with different thickness of air gap. The local SAR values in Fig. 9 are significantly affected by the type of fabric and the presence of an air gap and its thickness.

Above 20 GHz, the cotton fabric causes larger fluctuations for local SAR values than wool fabric. It can be realized from Fig. 9, the air gap between fabrics and skin tissue acts as an impedance matching layer.

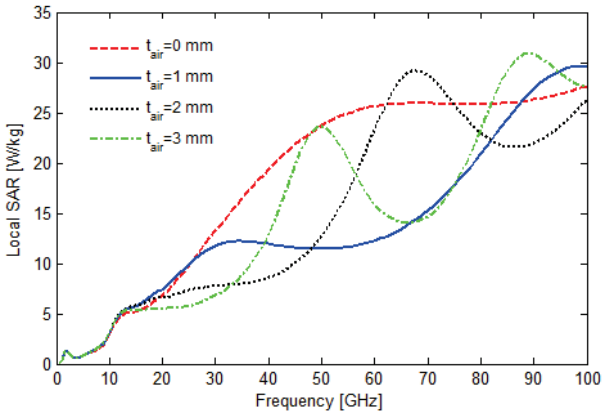

(a)

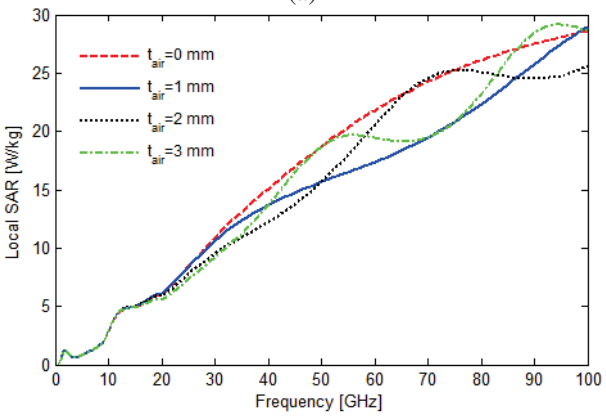

(b)

Fig. 9. Peak local SAR of 1D model clothed with 1 mm thick (a) cotton and (b) wool when $t_{air} = 0, 1, 2, 3$ mm.

IV. CONCLUSION

EM field exposure of 1D multi-layered head models clothed with cotton and wool fabrics is investigated using the FDTD method with Debye model in the frequency range from 1-100 GHz. The impact of the thickness of cotton and wool fabrics on EM field exposure metrics is analyzed up to 100 GHz. In addition, it is investigated how the presence of an air gap with different thickness between the fabric and the skin surface could affect power transmission to the skin surface, APD, and heating factor. Numerical results show that the presence of fabrics and air gap introduced between the fabric and the skin surface significantly affects power transmission to the skin surface, APD, and heating factor. Power transmission to the skin surface strictly depends on the thickness of the fabric and the air gap, resulting in decreased and increased EM power deposition in the tissues.

REFERENCES

[1] M. Zhadobov, N. Chahat, R. Sauleau, C. L. Quement, and Y. L. Drean, "Millimeter-wave interactions with the human body: State of knowledge and recent advances," *Int. J. Microw. Wireless Technol.*, vol. 3, no. 2, pp. 237-247, Mar. 2011.

[2] G. Sacco, D. Nikolayev, R. Sauleau, and M. Zhadobov, "Antenna/human body coupling in 5G millimeter-wave bands: Do age and clothing matter?" *IEEE Journal of Microwaves*, vol. 1, no. 2, pp. 593-600, Apr. 2021.

[3] T. S. Rappaport, S. Sun, R. Mayzus, H. Zhao, Y. Azar, K. Wang, G. N. Wong, J. K. Schulz, M. Samimi, and F. Gutierrez, "Millimeter wave mobile communications for 5G cellular: It will work!" *IEEE Access*, vol. 1, pp. 335-349, 2013.

[4] W. Hong, Z. H. Jiang, C. Yu, D. Hou, H. Wang, C. Guo, Y. Hu, L. Kuai, Y. Yu, Z. Jiang, Z. Chen, J. Chen, Z. Yu, J. Zhai, N. Zhang, L. Tian, F. Wu, G. Yang, Z.-C. Hao, and J. Y. Zhou, "The role of millimeter-wave technologies in 5G/6G wireless communications," *IEEE Journal of Microwaves*, vol. 1, no. 1, pp. 101-122, Jan. 2021.

[5] International Commission on Non-Ionizing Radiation Protection, "Guidelines for limiting exposure to electromagnetic fields (100 kHz to 300 GHz)," *Health Phys.*, vol. 118, no. 5, pp. 483-524, May 2020.

[6] IEEE Standard for Safety Levels with Respect to Human Exposure to Electric, Magnetic and Electromagnetic Fields, 0 Hz to 300 GHz, Standard C95.1-2019, 2019.

[7] A. Hirata and O. Fujiwara, "The correlation between mass averaged SAR and temperature elevation in the human head model exposed to RF near-fields from 1 to 6 GHz," *Phys. Med. Biol.*, vol. 54, no. 23, pp. 7227-7238, Dec. 2009.

[8] R. L. McIntosh and V. Anderson, "SAR versus VAR, and the size and shape that provide the most appropriate RF exposure metric in the range of 0.5-6 GHz," *Bioelectromagnetics*, vol. 32, no. 4, pp. 312-321, May 2011.

[9] A. Hirata, I. Laakso, T. Oizumi, R. Hanatani, K. H. Chan, and J. Wiart, "The relationship between specific absorption rate and temperature elevation in anatomically based human body models for plane wave exposure from 30 MHz to 6 GHz," *Phys. Med. Biol.*, vol. 58, no. 4, pp. 903-921, 2013.

[10] F. Kaburcuk and A. Z. Elsherbeni, "Temperature rise and SAR distribution at wide range of frequencies in a human head due to an antenna radiation,"

Applied Computational Electromagnetics Society (ACES) Journal, vol. 33, no. 4, pp. 367-372, Apr. 2018.

[11] F. Kaburcuk, A. Z. Elsherbeni, R. Lumnitzer, and A. Tanner, "Electromagnetic waves interaction with a human head model for frequencies up to 100 GHz", *Applied Computational Electromagnetics Society (ACES) Journal*, vol. 35, no. 6, pp. 613-621, June 2020.

[12] D. Funahashi, A. Hirata, S. Kodera, and K. R. Foster, "Area-averaged transmitted power density at skin surface as metric to estimate surface temperature elevation," in *IEEE Access*, vol. 6, pp. 77665-77674, 2018.

[13] K. Sasaki, M. Mizuno, K. Wake, and S. Watanabe, "Monte Carlo simulations of skin exposure to electromagnetic field from 10 GHz to 1 THz," *Phys. Med. Biol.*, vol. 62, no. 17, pp. 6993-7010, 2017.

[14] F. Gustrau and A. Bahr, "W-band investigation of material parameters, SAR distribution, and thermal response in human tissue," *IEEE Trans. Microwave Theory Tech.*, vol. 50, no. 10, pp. 2393-2400, Oct. 2002.

[15] I. Laakso, "Assessment of the computational uncertainty of temperature rise and SAR in the eyes and brain under far-field exposure from 1 to 10 GHz," *Physics in Medicine and Biology*, vol. 54, pp. 3393-3404, 2009.

[16] R. Morimoto, I. Laakso, V. De Santis, and A. Hirata, "Relationship between peak spatial averaged specific absorption rate and peak temperature elevation in human head in frequency range of 1-30 GHz," *Phys. Med. Biol.*, vol. 61, pp. 5406-5425, 2016.

[17] R. Morimoto, A. Hirata, I. Laakso, M. C. Ziskin, and K. R. Foster, "Time constants for temperature elevation in human models exposed to dipole antennas and beams in the frequency range from 1 to 30 GHz," *Phys. Med. Biol.*, vol. 62, pp. 1676-1699, 2017.

[18] Y. Hashimoto, A. Hirata, R. Morimoto, S. Aonuma, I. Laakso, K. Jokela, and K. R. Foster, "On the averaging area for incident power density for human exposure limits at frequencies over 6 GHz," *Phys. Med. Biol.*, vol. 62, no. 8, pp. 3124-3138, Mar. 2017.

[19] O. P. Gandhi and A. Riazi, "Absorption of millimeter waves by human beings and its biological implications," *IEEE Transactions on Microwave Theory and Techniques*, vol. 34, no. 2, pp. 228-235, Feb. 1986.

[20] G. Sacco, S. Pisa, and M. Zhadobov, "Impact of textile on electromagnetic power and heating in near-surface tissues at 26 GHz and 60 GHz," *IEEE Journal of Electromagnetics, RF and Microwaves in Medicine and Biology*, vol. 5, no. 3, pp. 262-268, Sep. 2021.

[21] A. R. Guraliuc, M. Zhadobov, G. Valerio, N. Chahat, and R. Sauleau, "Effect of textile on the propagation along the body at 60 GHz," *IEEE Transactions on Antennas and Propagation*, vol. 62, no. 3, pp. 1489-1494, Mar. 2014.

[22] K. Li and K. Sasaki, "Monte Carlo simulation of clothed skin exposure to electromagnetic field with oblique incidence angles at 60 GHz," *Front. Public Health*, vol. 10, no. 795414, 2022.

[23] K. Li, K. Sasaki, G. Sacco, and M. Zhadobov, "Clothing effect on multilayered skin model exposure from 20 GHz to 100 GHz," *IEEE Journal of Electromagnetics, RF and Microwaves in Medicine and Biology*, vol. 7, no. 4, pp. 408-415, Dec. 2023.

[24] T. Nagaoka, S. Watanabe, K. Sakurai, E. Kunieda, S. Watanabe, M. Taki, and Y. Yamanaka, "Development of realistic high-resolution whole-body voxel models of Japanese adult males and females of average height and weight, and application of models to radio-frequency electromagnetic-field dosimetry," *Phys. Med. Biol.*, vol. 49, no. 1, pp. 1-15, Jan. 2004.

[25] M. M. Okoniewski, M. P. Mrozowski, and M. A. Stuchly, "Simple treatment of multi-term dispersion in FDTD," *IEEE Microwave and Guided Wave Letters*, vol. 7, no. 5, pp. 121-123, 1997.

[26] A. Z. Elsherbeni and V. Demir, *The Finite-Difference Time-Domain Method for Electromagnetics with MATLAB Simulations*, 2nd ed. Edison, NJ: SciTech Publishing, 2016.

[27] R. S. Lumnitzer, "Energy harvesting near the human body using finite-difference time-domain simulations," dissertation, Colorado School of Mines, 2023.

[28] M. A. Eleiwa and A. Z. Elsherbeni, "Debye constants for biological tissues from 30 Hz to 20 GHz," *Applied Computational Electromagnetics Society (ACES) Journal*, vol. 18, no. 3, Nov. 2001.

[29] S. Kodera, K. Taguchi, Y. Diao, T. Kashiwa, and A. Hirata, "Computation of whole-body average SAR in realistic human models from 1 to 100 GHz," *IEEE Transactions on Microwave Theory and Techniques*, vol. 72, no. 1, pp. 91-100, Jan. 2024.

[30] N. O. Sadiku Matthew, *Elements of Electromagnetics*. Oxford: Oxford University Press, 2007.

[31] H. H. Pennes, "Analysis of tissue and arterial blood temperature in resting forearm," *J. Appl. Physiol.*, vol. 1, pp. 93-122, 1948.

[32] S. He, D. Huang, Z. Qi, H. Yang, Y. Hu, and H. Zhang, "The effect of air gap thickness on heat

transfer in firefighters' protective clothing under conditions of short exposure to heat," *Heat Transfer Research*, vol. 43, no. 8, pp. 749-765, 2012.

[33] G. Song, S. Mandal, and M. Rossi, *Thermal Protective Clothing for Firefighters*. Cambridge: Woodhead Publishing, 2016.

[34] A. Hirata, O. Fujiwara, and T. Shiozawa, "Correlation between peak spatial-average SAR and temperature increase due to antennas attached to human trunk," *IEEE Trans. Biomed. Eng.*, vol. 53, no. 8, pp. 1658-1664, 2006.

Fatih Kaburcuk received both the M.Sc. and Ph.D. degrees from Syracuse University, Syracuse, NY, USA, in 2011 and 2014, respectively, in electrical engineering. During his graduate studies, he worked as a Research Assistant with Syracuse University and PPC-Belden Inc. in Liverpool, NY, USA. He worked as a Visiting Research Scholar at the Department of Electrical Engineering, Colorado School of Mines, Golden, CO, USA, in 2014. He joined the Erzurum Technical University and Sivas Cumhuriyet University in 2015 and 2019, respectively. Dr. Kaburcuk is currently an Associate Professor in the Department of Electrical and Electronics Engineering at Sivas University of Science and Technology, Sivas, Turkiye. He is the Associated Editor for *Applied Computational Electromagnetics Society (ACES) Journal*. His research interests include numerical methods in electromagnetics, biological effect of electromagnetic radiation, and finite-difference time-domain analysis of antennas and RF devices.

Safety Assessment of Gender-specific Human Electromagnetic Exposure with Aortic Valve Stents for EV-WPT

Tianhong Tan[1], Tao Jiang[1], Yangyun Wu[2], Yu Zhu[2], and Yaodan Chi[3]

[1]College of Information and Communication Engineering
Harbin Engineering University, Harbin 150001, China
tthjob@163.com, jiangtao@hrbeu.edu.cn

[2]College of Instrumentation and Electrical Engineering
Jilin University, Changchun 130000, China
wuyangyun@jlu.edu.cn, zhuyu@jlu.edu.cn

[3]Jilin Provincial Key Laboratory of Architectural Electricity and Comprehensive Energy Saving Jilin Jianzhu University, Changchun 130118, China
147670107@qq.com

Abstract **–** Electric vehicle wireless power transfer brings additional electromagnetic exposure (EME) risks to the human body, especially those with metal implants. This paper focuses on the safety assessment of human EME with aortic valve stents (AVS), and establishes electromagnetic simulation models for different genders of humans, AVS, and electric vehicle-wireless power transfer (EV-WPT) systems. The transmission power of the EV-WPT system is 11 kW. Considering the uncertainty of the EV-WPT system and AVS in practical use, an efficient deep neural network method is proposed to evaluate the EME safety to different genders of humans. Using the standard limits of the International Committee on Non-Ionizing Radiation Protection (ICNIRP) as the judgment standard, comparing human EME under static conditions, it is demonstrated that AVS can change the distribution of induced electric fields in the human body and increase the risk of human EME. Moreover, the probability of male human EME exceeding the standard limits is 22.78% higher than that of female human.

Index Terms **–** Aortic valve stents (AVS), deep neural network, electric vehicle (EV), electromagnetic exposure safety, human model, wireless power transfer (WPT).

I. INTRODUCTION

Electric vehicles (EVs) are the core of future automotive technology development. Compared to plug-in charging, wireless power transfer (WPT) systems can save urban land space. Furthermore, the charging process is safe and reliable, enabling seamless charging [1]. More importantly, the electric vehicle-wireless power transfer (EV-WPT) system is a key link in improving intelligent driving. Therefore, the WPT system will be the development trend of future EV charging technology [2]. Due to the transmission of energy through open space [3], the EV-WPT system generates a large amount of leakage magnetic field, which inevitably exposes the nearby human body to the electromagnetic environment of the EV-WPT system. The safety of human electromagnetic exposure (EME) in the EV-WPT system has always been a focus of attention. In order to ensure the charging efficiency of EV and avoid range anxiety [4], the charging power of EV-WPT systems is usually as high as several thousand watts or even ten thousand watts, which significantly increases the risk of human EME. Therefore, evaluating the safety issues of human EME around EV-WPT systems is of great significance [5].

In order to ensure the safe use of high-power EV-WPT systems, many international organizations have developed relevant standards for the leakage magnetic field of WPT systems [6–8]. For example, the International Committee on Non-Ionizing Radiation Protection (ICNIRP) has developed different standards based on the different operating frequencies of WPT systems. When the operating frequency of WPT systems is below 100 kHz, the safety of human EME is mainly based on non-thermal effects, so the standard of concern is the induced electric field intensity (induced-E). When the working frequency of the WPT system is higher than 100 kHz, the EME safety of the human body is mainly based on thermal effects, and the specific absorption rate (SAR) of the human body is the standard of concern. With the current working frequency of EV-WPT systems typically being 85 kHz, this paper adopts induced-E as the analysis object of human EME in EV-WPT systems. The American Society of Automotive Engineers divides the

Submitted On: July 10, 2024
Accepted On: October 4, 2024

https://doi.org/10.13052/2024.ACES.J.390810

EV-WPT system into multiple levels based on transmission power [9], including WPT1 corresponding to 3.7 kw, WPT2 corresponding to 7.7 kw, and WPT3 corresponding to 11.1 kw. Considering the pursuit of charging speed for EVs, the 11.1 kw WPT system has most prominent research value.

For the human body exposed to the leakage magnetic field of the EV-WPT system, key organs in the human body are most worthy of attention. The heart is one of the most important organs in the human body, and there are a large number of cardiovascular disease patients in the world. Among them, aortic valve stenosis often leads to coronary artery disease, causing myocardial infarction and resulting in patient death. To treat this disease, a mechanical (metal made) aortic valve stent (AVS) is usually implanted into a narrowed valve in the patient's body to achieve normal blood delivery function of the heart [10, 11]. When the human body implanted with AVS is exposed to the leakage magnetic field of the EV-WPT system, the metal stent may change the distribution of electromagnetic energy, where the tip and edge of the stent are more likely to cause induced-E in the human body to exceed the recommended standard limit, leading to harm to the human body. In the practical application of the EV-WPT system, there is a lot of uncertainty in the positional relationship between the human body and the EV-WPT system, and there is usually misalignment between the transmitting and receiving coils of the WPT system. At the same time, there is also uncertainty in the relevant parameters of the WPT system during the production and manufacturing process. The above uncertainties will propagate to the leakage magnetic field of the EV-WPT system, ultimately affecting the EME safety of the human body. Therefore, it is of great significance to comprehensively evaluate the EME safety of human bodies with AVS in the leakage magnetic field of the EV-WPT system, taking into full consideration the uncertainties.

The main contributions of this paper are as follows:

1. Considering the human body of different genders, this paper evaluates the EME safety of males and females in the leakage magnetic field of the EV-WPT system;
2. This paper proposes a more efficient deep neural network method to analyze the uncertainty quantification (UQ) problem of human EME safety;
3. This paper analyzes the quantification of uncertainty in the safety of human EME with AVS, and takes into account the uncertainty of implants. It intuitively demonstrates the EME risk of the human body with metal medical implants in the leakage magnetic field of the EV-WPT system.

The main structure of this paper is as follows. Section II introduces the current research status of human EME safety assessment in the EV-WPT system. In section III, the human body model, AVS model, EV model, WPT system model, and human EME scenario are discussed. In section IV, the UQ method of our proposed deep neural network is introduced. Section V presents and analyzes the numerical experimental results of quantifying the safety uncertainty of human EME with AVS, and provides a detailed discussion. Section VI summarizes our research content and introduces our next research work.

II. RELATED WORK

EV-WPT technology is one of the most promising technologies, but it is accompanied by concerns about the electromagnetic safety of EV-WPT systems. Due to ethical issues in medicine and limitations in current technological levels [12], it is very difficult to measure the electromagnetic field inside the human body. Therefore, current research mainly focuses on numerical simulation, and analyzes the safety issues of human exposure to the electromagnetic environment of the EV-WPT system by establishing corresponding models in simulation software [13]. El-Shahat et al. [14] established an electromagnetic simulation model between the EV-WPT system and the human body, measured human EME at different distances, and analyzed the safe distance between the human body and the EV-WPT system. Chakarothai et al. [15] compared the numerical simulation results of human exposure in the electromagnetic environment of the EV-WPT system with experimental measurements, and derived the EME of the human body at different distances. Choi et al. [16] evaluated the electromagnetic safety issues of an EV-WPT system with a power of 20 kw, analyzed the EME values of the surrounding human body in the presence of offset between the transmitting and receiving coils, and compared them with the standard limits. The results showed that the basic limits of human fat and muscle were exceeded. Christ et al. [17] evaluated the exposure of the human body near the WPT system and analyzed it using four human models. They found that the intensity of human EME is closely related to the coil design and distance of the WPT system. Park [18] designed and established an electromagnetic simulation model for the EV-WPT system, and analyzed the human EME dose of the WPT system under different exposure scenarios, including shielded, unshielded, coil aligned, and coil misaligned conditions. By comparing with standard limits, the maximum transmission power and minimum safe distance of the EV-WPT system were proposed. Wang et al. [19] evaluated the human EME safety of an EV-WPT system with a power of 10 kw. They analyzed three human models and

three exposure fields and, based on the results, proposed recommendations for the maximum power of the EV-WPT system and three protective measures for human EME safety.

In addition to the aforementioned studies, researchers have also noticed the risks of metal implants in the human body exposed to electromagnetic fields and conducted research. Shah et al. [20] established EV-WPT system models with different power levels and analyzed the intensity of induced-*E* in human bodies with multiple metal implants. In the simulation results, it was observed that the induced-*E* at the tibial intramedullary nail exceeded the standard limit of ICNIRP. Meanwhile, Shah et al. [21] evaluated the safety of human EME around EV-WPT systems operating at radio frequencies. The analysis results showed that when the human body with implants is located near the EV-WPT system, the SAR in the human body will exceed the standard limit.

In the above studies, many researchers have focused on the impact of misalignment between the transmitting and receiving coils of the EV-WPT system on human EME safety. This is actually an undeniable uncertainty in the application process of the EV-WPT system, and metal implants also have uncertainty, which can significantly affect the distribution of electromagnetic fields in the human body. However, the existing main research only considers these situations as fixed exposure scenarios, especially in the EV-WPT system where there is more than one type of uncertainty, resulting in incomplete evaluation results of human EME safety. Currently, few studies have considered the impact of uncertainty on the safety of human EME. Wang et al. [22] considered the uncertainty of geometric parameters and human position in the EV-WPT system, and quantitatively analyzed the uncertainty of human EME safety based on spectral methods. However, they did not take into account the potential impact of metal implants on the evaluation results. In [23], the influence of metal implants was considered, but the research subjects were males only. The uncertainty quantification method used was probability driven, and the computational cost would increase with the increase of variable dimensionality, leading to the problem of ”curse of dimensionality”. Therefore, in response to the shortcomings in the above research, this article takes male and female models with heart AVSs around the EV-WPT system as the research objects, considers uncertain exposure scenarios in practical applications, proposes an efficient deep neural network method to quantify the uncertainty of human EME safety, analyzes the statistical probability of risks exceeding standard limits, and intuitively evaluates human EME safety.

III. MATH

A. EV and WPT system

Firstly, the EV-WPT device model established in this article consists of an EV and a magnetic coupled WPT device. The EV model in this paper is constructed based on a pure electric sports car model with excellent power performance. As shown in Fig. 1, its spatial geometric dimension is 4520×2050×1260 mm. Considering that real sports cars need to balance lightweight, high rigidity, and stability, the body and wheels of this article are made of aluminum alloy material, the front and rear windshields and windows are made of polycarbonate material, and the tires are made of rubber material. The size and material of the above EV model fully meet the requirements of this study.

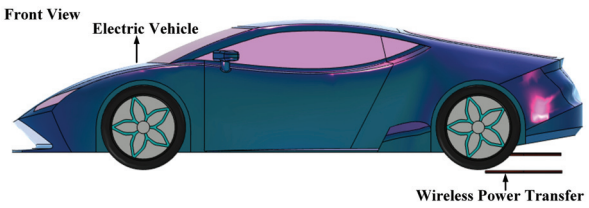

Fig. 1. EV model.

The working principle of the WPT system is shown in Fig. 2 . The power grid inputs AC power, which is converted into DC power through a rectifier circuit at the transmitting end. The DC power is then converted into higher frequency AC power through a high-frequency inverter circuit. The output power frequency of the inverter circuit is the resonant frequency of the transmitting resonant circuit. At this time, the transmitting circuit works in a resonant state under the action of the compensating circuit at the transmitting end, presenting pure resistance. According to Faraday’s law of electromagnetic induction, the transmitting coil excites a high-frequency electromagnetic field with a resonant frequency in space, which is induced and received by the receiving end coil. At this time, under the action of the receiving end compensation circuit, the receiving end circuit works in a resonant state and also presents pure resistance. The receiving end rectification circuit and DC-DC circuit convert the high-frequency power supply into the DC power required by the load, achieving wireless energy transmission. The magnetic coupling WPT device in this article equivalently converts the transmitting and receiving circuits. The transmitting and receiving devices are considered as shown in Fig. 3 . The transmitting device consists of a transmitting metal electromagnetic shielding layer and a transmitting coil (Tx), while the receiving device consists of a receiving metal

electromagnetic shielding layer and a receiving coil (Rx). The geometric dimensions of the transmitting and receiving electromagnetic shielding layers are the same, both 620×620×8 mm (A×A). The material selection is ferrite material, which is commonly used for electromagnetic shielding. The wire diameters of Tx and Rx are 2.5×10^{-6} and 1.8×10^{-6} mm^2, with 15 and 20 turns, respectively.

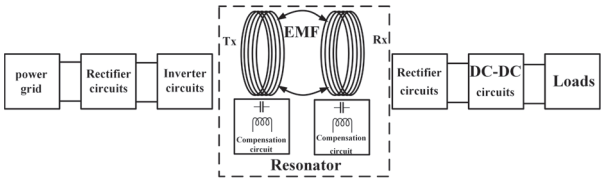

Fig. 2. Working principle of WPT system.

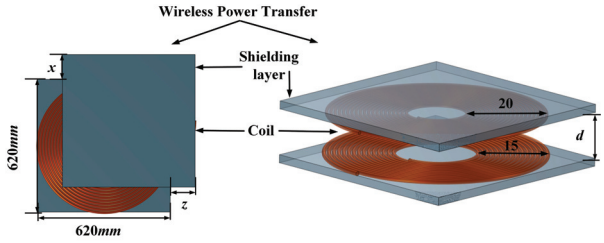

Fig. 3. WPT geometric model.

In order to improve the transmission performance of the magnetic coupled WPT device, an LCC-LCC topology compensation network structure is adopted in this article, as shown in Fig. 4 . Among them, I_0 is the equivalent current source at the transmitting end of the linear WPT circuit model, U_1 is the terminal voltage of the equivalent current source at the transmitting end, and L_{s1} and L_1 are the resonant inductance at the transmitting end and the self-inductance of Tx, respectively. The isolation capacitance and resonant capacitance at the corresponding transmitting end are C_{p1} and C_{s1}, respectively. R_{s1} and R_1 are the internal resistance of L_{s1} and Tx, respectively. M is the mutual inductance between the transmitter and receiver. Similarly, L_{s2} and L_2 are the resonant inductance at the receiving end and the self-inductance of Rx, respectively. The isolation capacitance and resonant capacitance at the receiving end are C_{p2} and C_{s2}, respectively. R_{s2} and R_2 are the internal resistances of L_{s2} and Tx, respectively. R_L is the resistance of the load carried by the WPT device, and U_2 is the terminal voltage of the load at the receiving end. When the LCC-LCC topology compensation circuit operates in a resonant state, the following resonant conditions apply.

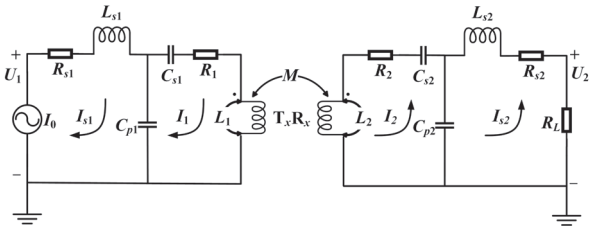

Fig. 4. LCC-LCC topology compensation circuit.

Resonance conditions at the transmitting end:

$$\omega L_1 - \frac{1}{\omega C_{s1}} = \frac{1}{\omega C_{p1}} = \omega L_{s1}. \tag{1}$$

Resonance conditions at the receiving end:

$$\omega L_2 - \frac{1}{\omega C_{s2}} = \frac{1}{\omega C_{p2}} = \omega L_{s2}. \tag{2}$$

When the magnetic coupled WPT device operates at a resonant frequency of 85 kHz and there are no dislocations at the transmitting and receiving ends, this paper considers its transmission power to be 11 kW.

B. Male and female human models

This paper considers the inconsistency of body fat and muscle content between males and females. In order to obtain the differences in EME between males and females, human models of males and females were established using Comsol finite element numerical simulation software, as shown in Fig. 5 . Among them, the male

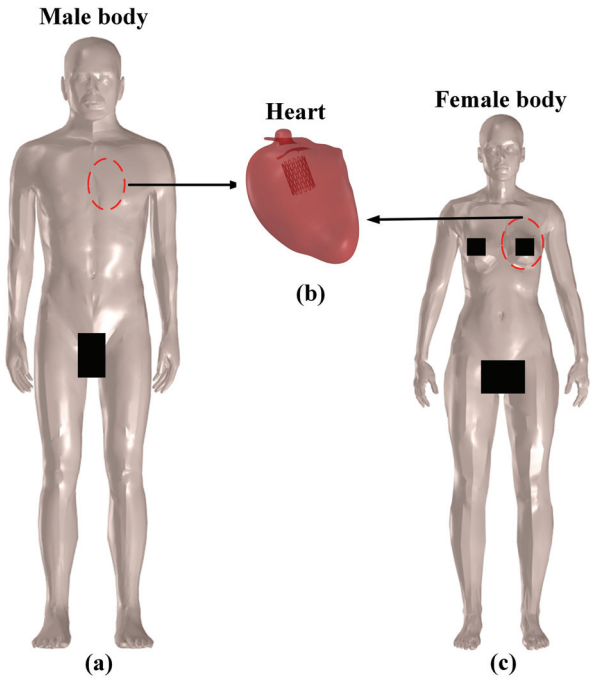

Fig. 5. (a) Male human model, (b) heart with AVS, and (c) female human model.

human model has a height of 1.80 m and a weight of 77 kg, while the female model has a height of 1.68 m and a weight of 55 kg.

The resonant transmission frequency of the EV-WPT device in this article is 85 kHz, the conductivity of male human tissue is considered to be 0.27 s/m, and the relative permittivity is 5500. The electrical conductivity of female human tissue is considered to be 0.23 s/m, with a relative permittivity of 5300. The conductivity of cardiac tissue is considered to be 0.21 s/m, with a relative permittivity of 11137 [20, 22]. According to ICNIRP 2010, when the electromagnetic field radiation frequency is less than 100 kHz, the induced-E inside the human body is the main measurement target. Therefore, this article uses induced-E as the indicator for calculating human EME. In addition, according to the recommendations of ICNIRP, when calculating the induced-E of the human body, the mesh division of the human body model should be within $2\times2\times2$ mm^3, the mesh division for male and female body models in this article adopts $0.9\times0.9\times0.9$ mm^3, which meets the recommendations of ICNIRP.

C. AVS

This paper evaluates the electromagnetic safety issues of the leakage electromagnetic field generated during the operation of the EV-WPT device on human bodies of different genders containing metal medical implants. The heart is the engine of the human body, which circulates blood to various parts of the body through contraction and relaxation. However, among cardiovascular diseases, the incidence rate and mortality rate of aortic valve disease is the second highest in the world [24]. Every year, nearly 30000 patients worldwide receive AVS replacement [25]. AVS is used to replace diseased valves to achieve the recovery of cardiac pumping function. Figures 6 (a-c) show the front and top views of the AVS customary in this paper. The length of the AVS is 26.7 mm and the diameter is 20 mm. The AVS is composed of 45 diamond shaped structures,

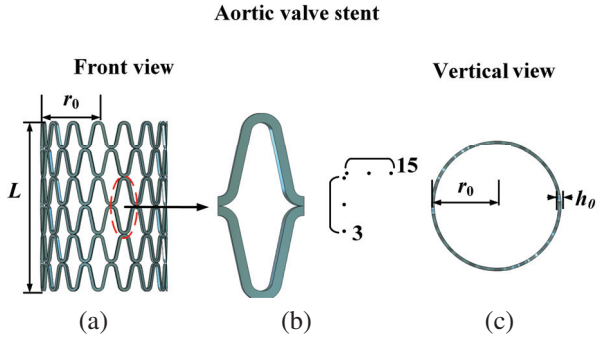

Fig. 6. Implant model.

each with a thickness of 0.45 mm and an edge width of 0.45 mm. Considering the biological safety, compatibility, and high strength of titanium alloy, nickel titanium alloy is chosen as the material for the AVS, with the following electromagnetic parameters: conductivity of 2.38×10^6 S/m, with a relative dielectric constant of 1. The sharp edge of metal implants can affect the distribution of electromagnetic fields and have the potential to absorb electromagnetic energy. Considering the high precision and multi tip of the AVS in this article, its mesh is divided into a finer resolution of $0.15\times0.15\times0.15$ mm^3.

D. Electromagnetic field analysis and calculation

To analyze the alternating electromagnetic field generated by magnetic coupled WPT using near-field theory, the electromagnetic field generated by resonators can be divided into radiated electromagnetic field and induced electromagnetic field by their properties. There is a 90° phase angle between the magnetic field and the electric field of the induced electromagnetic field. The electromagnetic energy of the induced electromagnetic field exchanges with each other during electromagnetic oscillations, flowing back and forth between the surrounding space and the resonator, without external radiation. In contrast, the radiated electromagnetic field is detached from the electromagnetic coupling resonator and radiated externally. According to the distance from the radiation source, the induced electromagnetic field and the radiated electromagnetic field are divided into near-field and far-field. The field intensity in the far-field decays with increasing distance. When the distance from the resonator is multiple wavelengths, only the electromagnetic radiation field needs to be considered. When the distance from the resonator is within the $\lambda/2\pi$ (λ is the wavelength), only the induced electromagnetic field needs to be considered. When working in the near-field, there is only electromagnetic field flow around and between the resonator, and there is no emission in the distance. Only by working in the near-field space can efficient energy transfer be achieved between the fields and circuits of the electromagnetic resonant WPT device.

When analyzing the numerical calculation of the electromagnetic field generated by magnetic coupled WPT, the magnetic quasi-static (MQS) method is used to solve the electromagnetic field value considering that the wavelength of the electromagnetic wave in space is larger than the geometric shape of the target to be solved. The criteria for using the MQS method are as follows [26]:

$$|\alpha^2| d^2 \ll 1, \tag{3}$$

$$\alpha^2 = \omega(\omega\varepsilon_r + j\sigma)\mu_0. \tag{4}$$

Among them, α is the wavenumber and d is the diameter of the calculation area. In the absence of

damage, the relationship between α and wavelength λ is $\alpha=2\pi/\lambda$, ω is the angular frequency of the electromagnetic field, the dielectric constant and conductivity of ε_r and σ human tissues, and μ_0 is the value of vacuum permeability $4\pi \times 10^{-7}$ (H/m).

In this paper, the transmission frequency of the magnetic coupled EV-WPT device is 85 kHz, and the electromagnetic wavelength generated in the near-field is about tens of meters [26]. When analyzing the electromagnetic field values at this frequency, the size of the target is much smaller than the wavelength of the electromagnetic wave, and the MQS method can be used to solve it.

E. Exposure scenario

The WPT system transmits energy through an open, loosely coupled structure, thus posing a higher risk when the human body is exposed without obstruction. Considering the practical situation of the EV-WPT system in daily use, the vehicle chassis is usually composed of metal, which has a certain shielding effect. Therefore, this paper mainly considers the situation where the human body is located outside the vehicle, and takes the exposure scene when the human body is located at the rear of the vehicle as the research object, as shown in Fig. 7.

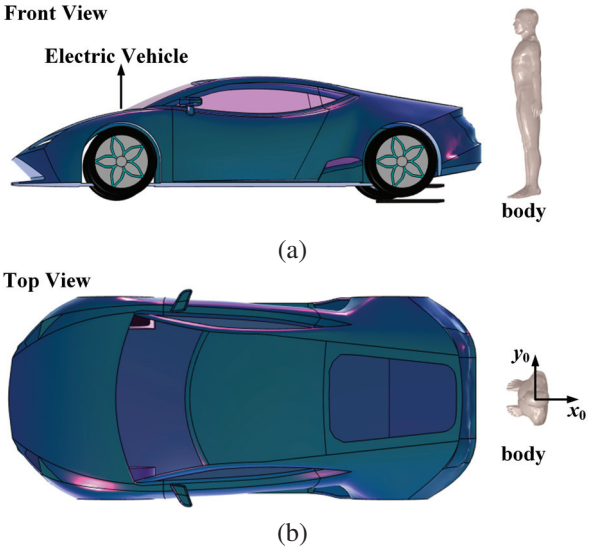

Fig. 7. Electromagnetic exposure scenarios.

IV. UNCERTAINTY QUANTIFICATION METHOD BASED ON DEEP NEURAL NETWORKS

In recent years, UQ based on machine learning theory has been vigorously promoted as an emerging technology, among which classic methods include Bayesian neural network prediction, Markov chain, Monte Carlo, approximate variational inference, etc. These methods have been successfully applied in multiple fields such as drone driving, moving object detection, and image processing, effectively achieving multiple functions such as probability statistical moment estimation and risk assessment. In the actual scenario of wireless energy transmission in EVs, considering the influence of uncertain factors such as misalignment of coupling coil groups caused by improper driver operation and errors in the manufacturing process of system components, the human EME indicators located around the wireless charging device also have strong uncertainties. Therefore, it is urgent to carry out human EME safety assessment and analysis.

This paper focuses on the induced-E of the heart with an AVS in the human body as the research objective. Deep neural networks are used to quantify the uncertainty of the induced-E of the human body under the exposure environment of the EV-WPT system, and the probability density distribution of the induced electric field strength value is obtained. The neural network itself consists of many hidden layers. Assuming that the input of a single node in the hidden layer is x and the output is y, the relationship between y and x can be expressed as:

$$y = \sigma(w \cdot x + b), \tag{5}$$

where $\sigma(\cdot)$ represents a nonlinear transfer function, w is a linear mapping, and b is the bias term. The RELU function is selected as the $\sigma(\cdot)$ function for the nodes in the hidden layer. Before starting to train the network model, the values of w and b are randomly assigned. During the model training process, the values of w and b are continuously updated until the error between the output result and the training label is approximately zero. The specific evaluation index function can be expressed as:

$$E^{w,b}(x,y) = \frac{1}{2N}\sum_{i=1}^{N} \|y_i - y^*\|^2, \tag{6}$$

where N represents the number of training samples, y_i represents the network output value, and y^* represents the training label. When $E^{w,b}(x,y)$ approaches infinity, it indicates that the current network training effect is relatively ideal. Based on the actual situation, random variables that may affect the induced-E of the human body are selected in the article, including the offset parameters of the transmitting and receiving coils, resonance compensation circuit parameters, metal implant parameters, and position parameters between the human body and the car. Trace data is collected from the distribution range of these variables as training set samples, and the induced-E corresponding to each group of samples are used as training labels, based on this, to train the deep neural network model.

The deep neural network constructed in the paper consists of multiple sub-models and adopts ensemble learning to effectively improve the computational accu-

racy and efficiency of the output end. Among them, each sub-model of the network is composed of three modules. The input of the first module is z_0, x_0, d_0, r_0, h_0. The input of the second module is th, c_1, c_2, cf_1, cf_2, lf_1 and the output of the first module. The input of the third module is lf_2, z_1, x_1 and the output of the second module. Finally, the predicted value of the human induced-E is obtained at the output end. The first part of the module consists of six fully connected layers and one batch normalization layer. The number of nodes in the first to last six fully connected layers is set to 5, 64, 32, 32, 16, and 1, respectively. The input feature number of the batch normalization layer is 32. Introducing a batch normalization layer can to some extent prevent overfitting in network training and strengthen the model's generalization ability. The specific normalization mathematical model can be expressed as:

$$y = \gamma \cdot \frac{x_i - E(x)}{\sqrt{var(x) + \varepsilon}} + \beta, \tag{7}$$

$$E(x) = \frac{1}{n}\sum_{i=1}^{n} x_i, \tag{8}$$

$$var(x) = \frac{1}{n}\sum_{i=1}^{n} (x_i - E(x))^2, \tag{9}$$

where γ and β are both parameter vectors, with default values of 0 and 1, respectively. ε is used to ensure numerical stability, with default values of 10^{-5}. The second part of the module consists of four fully connected layers, with the number of neuron nodes set to 7, 64, 32, and 1 in each layer from front to back. The third part of the module consists of five fully connected layers and a dropout layer. The number of nodes in the first to last five fully connected layers is 4, 64, 32, 16, and 1, respectively. The dropout function is similar to a batch normalization layer. By using the dropout module, some neural nodes can be randomly discarded, reducing the number of intermediate features and preventing the network model from being too close to the training set samples. Similarly, the overfitting effect can also be weakened to a certain extent. Figure 8 shows a comparison diagram of the dropout module applied before and after the network layer.

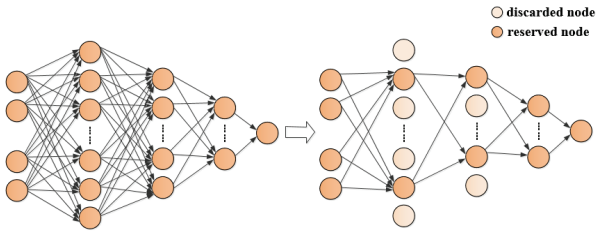

Fig. 8. Comparison of network layer structures before and after applying dropout.

After combining with the dropout module, the calculation formula for neuron nodes is updated to:

$$y_i^{l+1} = f(w_i^{l+1} \cdot r^l y^l + b_i^{l+1}), \tag{10}$$

$$r^l \sim Bernoulli(p), \tag{11}$$

where r^l represents a random number that follows a Bernoulli distribution and p represents the corresponding probability. Generally, the ideal value of p is 0.5. On the basis of the neural network model mentioned above, the paper adopts six model ensemble learning methods to merge the output of each sub-model to obtain more accurate prediction results.

Basic parameters such as the hidden layer structure and the number of training/testing samples for each sub-model are the same, with only differences in the number of training iterations and learning rate. Among them, the iteration numbers of the first three sub-models are set to 100, 200, and 400, respectively, and the learning rate is uniformly set to 10^{-3}. The iteration numbers of the last three sub-models are set to 600, 800, and 1000, respectively, and the learning rate is uniformly set to 2×10^{-3}. Figure 9 shows the basic structural framework of the integrated network model.

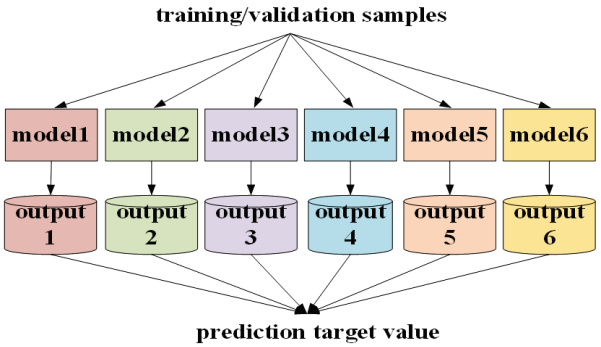

Fig. 9. Integrated prediction framework for multiple network models.

After the model training is completed, validation samples are collected from the distribution range of various related random variables as input, and the probability density distribution of human induced-E is finally obtained at the output end of the model, achieving quantitative safety assessment of human EME uncertainty in the wireless energy transmission environment of EVs. The pseudocode of the algorithm used in this paper is as follows:

V. SIMULATION RESULTS

A. Comparison of male and female body exposure under static conditions

The electromagnetic environment of the EV-WPT system under normal operation is shown in Fig. 10 . Based on the human EME scenario set in section III,

The uncertainty quantification based on deep neural network model

1.**While** the training iteration of model is below the maximum iterations
2. **For** the learning stage of first part of network module
3. update the weight threshold of first part of network module
4. **end for**
5. **For** the learning stage of second part of network module
6. update the weight threshold of second part of network module
7. **end for**
8. **For** the learning stage of third part of network module
9. update the weight threshold of third part of network module
10. **end for**
11. Get the output value
12. If the error of output value and training target meets the requirement, then complete the model training
13.**end while**
14.Obtain the probability density of heart's induced-*E* based on single neural network model
15.Calculate the probability density of heart's induced-*E* based on ensemble output of six models

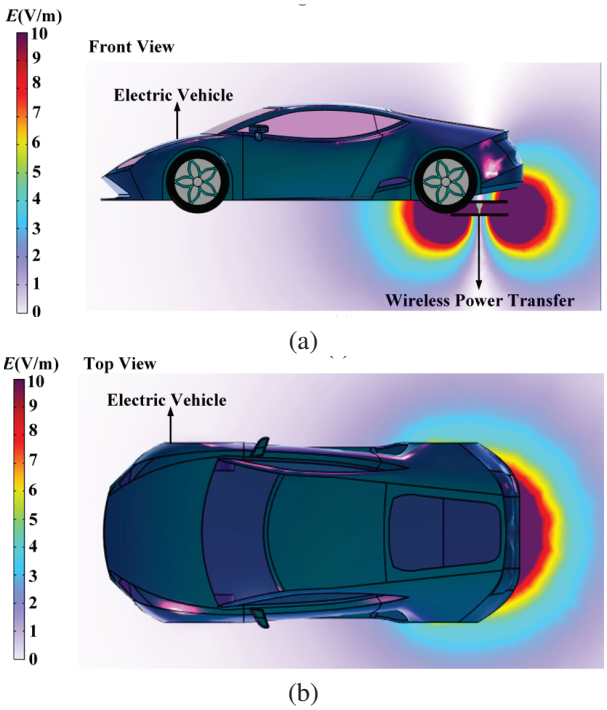

Fig. 10. EV-WPT system electromagnetic environment.

evaluate the safety issues of human EME using the EV-WPT system, male and female human body, and implant models established in this paper. Without considering uncertainty, that is, there is no offset between the transmitting and receiving coils of the WPT system, the resonance compensation circuit parameters are consistent with the design values, and the distance between the human body and the car is 0.2 m. Compare the EME of males and females without and with AVS, as shown in Figs. 11 and 12.

Observe the EME of the human body in Figs. 11 and 12, and compare the maximum value and location of the induced-*E* in different genders at this time, as shown in Table 1 . In the current exposure scenario, the induced-*E* in the male and female human bodies is basically the same and has not exceeded the standard limit of ICNIRP. Figures 11 and 12 illustrate the EME of male and female human bodies without considering the uncertainty variables listed in Table 2 . In this case, there is no significant difference in the leakage magnetic field distribution of the WPT system between males and females, indicating

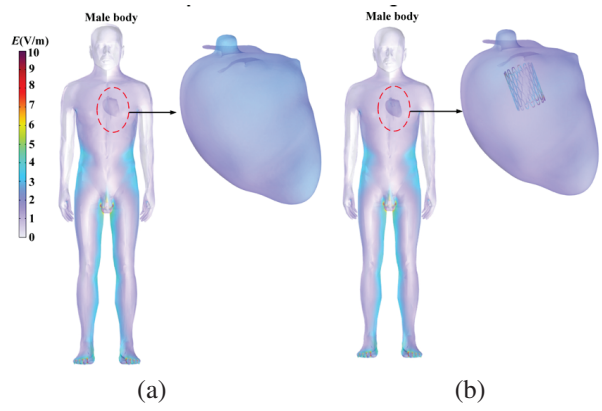

Fig. 11. Comparison of induced-*E* in male human body.

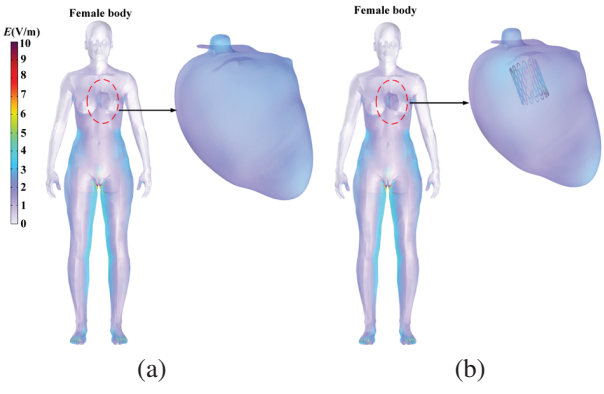

Fig. 12. Comparison of induced-*E* in female human body.

Table 1: The maximum value and location of induced-E in the human body

Gender	AVS	Induced-E_{max} (V/m)	Position
Male	Yes	4.765	Near AVS
	No	2.563	Human feet
Female	Yes	4.076	Near AVS
	No	2.324	Human feet

Table 2: The uncertainty of variables

Variables	Unit	Distribution Parameters
x	m	U [-0.075, 0.075]
z	m	U [-0.075, 0.075]
d	m	U [-0.05, 0.05]
r_0	mm	N [10, 3.33]
h_0	mm	N [0.45, 0.15]
th	mm	N [0.45, 0.15]
C_{s1}	f	N [7.98, 0.13] *10^{-9}
C_{s2}	f	N [11.94, 0.2] *10^{-9}
C_{p1}	f	N [32.64, 0.54] *10^{-9}
C_{p2}	f	N [21.52, 0.36] *10^{-9}
L_{s1}	h	N [10.74, 0.18] *10^{-6}
L_{s2}	h	N [16.26, 0.27] *10^{-6}
x_0	m	U [0, 0.2]
y_0	m	U [-0.2, 0.2]

that there are no substantial disparities. Further observation of the EME at the heart reveals that the induced-E of the heart with an AVS is significantly higher than that of the heart without implants, and this leads to the position of the maximum induced-E in the human body shifting from the feet to the heart. This proves that metal implants have a significant impact on the distribution of electromagnetic fields in the human body, and lead to a maximum increase of induced-E in the human body by more than 1.76 times, increasing the risk of human EME safety.

B. Comparison of male and female human exposure considering uncertainty

In the practical application of the EV-WPT system, there are usually many uncertain factors, such as the offset parameters of the transmitting and receiving coils, resonance compensation circuit parameters, metal implant parameters, and position parameters between the human body and the EV. In this paper, the above parameters are used as input variables for quantifying the safety uncertainty of human EME, and different distribution types and parameters are set according to the daily use of the EV-WPT system. These variables are also inputs to the deep neural network, as shown in Table 2 . Among them, N is a normal distribution, corresponding parameters are mean and standard deviation, U is a uniform distribution, and corresponding parameters are lower and upper boundaries. Due to the consideration of the situation with an AVS in this paper, the maximum value of induced-E in the central organ of the human body is used as the output for quantifying the safety uncertainty of human EME. The probability density distribution curves of induced-E for both male and female genders are compared, and the results of 2000 Monte Carlo simulations are compared to verify the effectiveness of the proposed deep learning method, as shown in Fig. 13 .

The standard limit for human induced-E in ICNIRP 2010 is 11.5 V/m. Using this value as the judgment standard, the probability of male induced-E exceeding the standard limit is calculated to be 66.67%, while the probability of female induced-E exceeding the standard limit is 43.89%. This intuitively demonstrates the risk of human exposure to the electromagnetic environment of the EV-WPT system, and the probability of male EME is higher than that of female. According to the

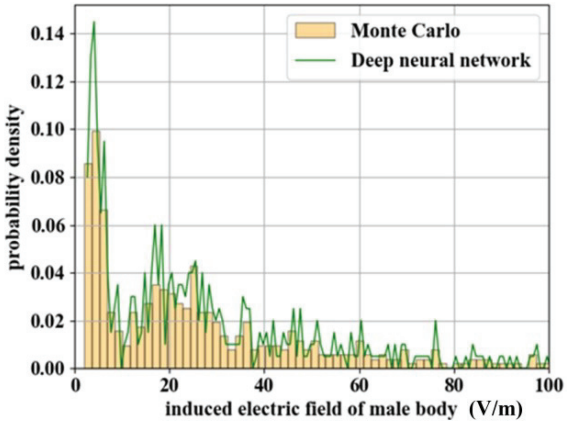

(a)

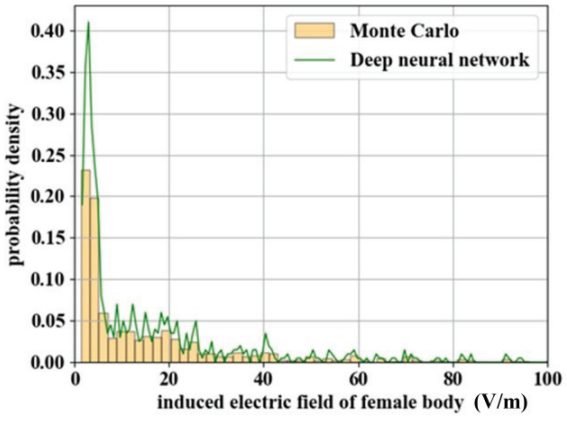

(b)

Fig. 13. (a) Probability density distribution of induced-E in male human EME and (b) probability density distribution of induced-E in female human EME.

analysis of EME in different genders under static conditions, the maximum value of induced-*E* in humans with AVS is usually located at the heart position, while the body thickness of female at the heart position is higher than that of male. Therefore, in the case of humans with AVS, the EME risk of female is lower than that of male due to the shielding effect of the female human body.

VI. CONCLUSION

The main purpose of this paper is to evaluate the safety issues of different genders of humans with AVS exposed to electromagnetic fields in the EV-WPT system. In the electromagnetic environment of the 11 kW transmission power EV-WPT system established in this paper, considering the uncertainty of the EV-WPT system, human EME position, and AVS parameters, the EME safety of different genders is evaluated for the scenario where the human body is located at the rear of the vehicle, which has a high risk of EME. The results indicate that, under static conditions, AVS can significantly alter the distribution of electromagnetic fields in the human body, leading to a maximum increase of induced-*E* in the human body by more than 1.76 times. Under the condition of considering uncertainty, due to the differences in human body between different genders, the risk probability of induced-*E* exceeding the standard limit in a male body is 66.67%, while the risk probability in a female body is 43.89%. In the following research, we will consider more human EME situations and, in order to protect the safety of human EME, we will conduct research on human electromagnetic safety protection devices.

ACKNOWLEDGMENT

This work is supported by the National Key Research and Development Program of China (2022YFE0123600). This paper is also supported by the Jilin Scientific and Technological Development Program under Grant 20240101117JC, Grant 20230201122GX, and Key Laboratory for Comprehensive Energy Saving of Cold Regions Architecture of Education, Jilin Jianzhu University under Grant JLJZHDKF202203.

REFERENCES

[1] P. Machura, V. De Santis, and Q. Li, "Driving range of electric vehicles charged by wireless power transfer," *IEEE Trans. Veh. Technol.*, vol. 69, no. 6, pp. 5968-5982, June 2020.

[2] W. Zhang and C. C. Mi, "Compensation topologies of high-power wireless power transfer systems," *IEEE Trans. Veh. Technol.*, vol. 65, no. 6, pp. 4768-4778, June 2016.

[3] H. Zhou, A. Zhu, Q. Deng, J. Chen, F. Yang, and W. Hu, "Protection strategy for wireless charging electrical vehicles," *IEEE Trans. Veh. Technol.*, vol. 69, no. 11, pp. 13510-13520, Nov. 2020.

[4] J. M. Miller, O. C. Onar, and M. Chinthavali, "Primary-side power flow control of wireless power transfer for electric vehicle charging," *IEEE Trans. Emerg. Sel. Topics Power Electron.*, vol. 3, no. 1, pp. 147-162, Mar. 2015.

[5] P. Moreno-Torres Concha, P. Velez, M. Lafoz, and J. R. Arribas, "Passenger exposure to magnetic fields due to the batteries of an electric vehicle," *IEEE Trans. Veh. Technol.*, vol. 65, no. 6, pp. 4564-4571, June 2016.

[6] International Commission on Non-Ionizing Radiation Protection, "Guidelines for limiting exposure to time-varying electric and magnetic fields (1 Hz to 100 kHz)," *Health Phys.*, vol. 99, pp. 818-836, 2010.

[7] International Commission on Non-Ionizing Radiation Protection, "Gaps in knowledge relevant to the 'Guidelines for limiting exposure to time-varying electric and magnetic fields (1 Hz-100 kHz)," *Health Phys.*, vol. 118, no. 5, pp. 533-542, 2020.

[8] "IEEE Standard for Safety Levels with Respect to Human Exposure to Electric, Magnetic, and Electromagnetic Fields, 0 Hz to 300 GHz," *IEEE Standard C95.1*, 2019.

[9] "Wireless Power Transfer for Light-Duty Plug-in/Electric Vehicles and Alignment Methodology," SAE Standard J2954_202010 [Online]. Available: https://www.sae.org/standards/content/j2954_202010/

[10] L. Perpétuo, A. S. Barros, J. Dalsuco, R. Nogueira-Ferreira, P. Resende-Gonçalves, I. Falcão-Pires, R. Ferreira, A. Leite-Moreira, F. Trindade, and R. Vitorino, "Coronary artery disease and aortic valve stenosis: A urine proteomics study," *Int. J. Mol. Sci.*, vol. 23, no. 21, pp. 13579, Nov. 2022.

[11] M. Kim, W. Lee, K. Kim, H. Lim, and Y. J. Kim, "A preclinical trial of periventricular pulmonary valve implantation: Pericardial versus aortic porcine valves mounted on self-expandable stent," *Artif. Organs.*, vol. 45, no. 5, pp. E89-E100, Oct. 2020.

[12] D. Poljak, M. Cvetković, O. Bottauscio, A. Hirata, I. Laakso, and E. Neufeld, "On the use of conformal models and methods in dosimetry for nonuniform field exposure," *IEEE Trans. Electromagn. Compat.*, vol. 60, no. 2, pp. 328-337, Apr. 2018.

[13] J. Xi, A. Christ, and N. Kuster, "Coverage factors for efficient demonstration of compliance of low-frequency magnetic near-field exposures with basic restrictions," *Phys. Med. Biol.*, vol. 68, no. 3, Feb. 2023.

[14] A. El-Shahat, J. Danjuma, A.Y. Abdelaziz, and S. H. E. Abdel Aleem, "Human exposure influence analysis for wireless electric vehicle battery charging," *Clean Technol.* vol. 4, no. 2, pp. 785-805, 2022.
[15] J. Chakarothai, K. Wake, T. Arima, S. Watanabe, and T. Uno, "Exposure evaluation of an actual wireless power transfer system for an electric vehicle with near-field measurement," *IEEE Trans. Microw. Theory Techn.*, vol. 66, no. 3, pp. 1543-1552, Mar. 2018.
[16] B. Choi, E. Kim, W. Shin, S. Park, and K. Kim. "Exposure assessment of a 20-kW wireless power transfer system for electric vehicles," *Int. J. Automot. Technol*., vol. 21, pp. 1349-1353, 2020.
[17] A. Christ, M. G. Douglas, J. M. Roman, E. B. Cooper, A. P. Sample, and B. H. Waters, "Evaluation of wireless resonant power transfer systems with human electromagnetic exposure limits," *IEEE Trans. Electromagn. Compat.*, vol. 55, no. 2, pp. 265-274, Apr. 2013.
[18] S. Park, "Evaluation of electromagnetic exposure during 85 kHz wireless power transfer for electric vehicles," *IEEE Trans. Magn.*, vol. 54, no. 1, pp. 1-8, Jan. 2018.
[19] Q. Wang, W. Li, J. Kang, and Y. Wang, "Electromagnetic safety evaluation and protection methods for a wireless charging system in an electric vehicle," *IEEE Trans. Electromagn. Compat.*, vol. 61, no. 6, pp. 1913-1925, Dec. 2019.
[20] I. A. Shah, Y. Cho, and H. Yoo, "Safety evaluation of medical implants in the human body for a wireless power transfer system in an electric vehicle," *IEEE Trans. Electromagn. Compat.*, vol. 63, no. 3, pp. 681-691, June 2021.
[21] I. A. Shah and H. Yoo, "Assessing human exposure with medical implants to electromagnetic fields from a wireless power transmission system in an electric vehicle," *IEEE Trans. Electromagn. Compat.*, vol. 62, no. 2, pp. 338-345, Apr. 2020.
[22] T. Wang, Q. Yu, B. Li, G. Lv, Y. Wu, and S. Guan, "Uncertainty quantification of human electromagnetic exposure from electric vehicle wireless power transfer system," *IEEE Trans. Intell. Transp. Syst.*, vol. 24, no. 8, pp. 8886-8896, Aug. 2023.
[23] T. Wang, B. Li, K. Zhao, Q. Yu, L. Xu, Y. Chi, and S. Guan, "Evaluation of electromagnetic exposure of the human with a coronary stent implant from an electric vehicle wireless power transfer device," *Electronics*, vol. 12, no. 20, p. 4231, 2023.
[24] M. Aenis, A. P. Stancampiano, A. K. Wakhloo, and B. B. Lieber, "Modeling of flow in a straight stented and nonstented side wall aneurysm model," *J. Biomech. Eng*., vol. 119, no. 2, pp. 206-212, May 1997.
[25] T. Ando and H. Takagi, "Percutaneous closure of paravalvular regurgitation after transcatheter aortic valve implantation: A systematic review," *Clin. Cardiol*., vol. 39, no. 10, pp. 608-614, 2016.
[26] A. Christ, M. Douglas, J. Nadakuduti, and N. Kuster, "Assessing human exposure to electromagnetic fields from wireless power transmission systems," *Proc. IEEE*, vol. 101, no. 6, pp. 1482-1493, June 2013.

Tianhong Tan received the B.S. degree in electrical engineering from Jilin University, Changchun, Jilin, China, in 2014. He is currently pursuing the Ph.D. degree in Information and Communication Engineering at Harbin Engineering University. His research interests include the electromagnetic compatibility, electromagnetic simulation and effectiveness evaluation

Tao Jiang received the Ph.D. degree from the Harbin Engineering University, Harbin, China, in 2002. Since 1994, he has been a Faculty Member of College of Information and Communication, Harbin Engineering University, where he is currently a Professor. He was a Postdoctoral Researcher with the Research Institute of Telecommunication, Harbin Institute of Technology, Harbin, China, from 2002 to 2003, and a Visiting Scholar with the Radar Signal Processing Laboratory, National University of Singapore, from 2003 to 2004. His current research interests include radio wave propagation, complex electromagnetic system evaluation, modeling, and simulation. IEEE Member 85027296.

Yangyun Wu received the B.S. degree in architectural electricity and intelligence from the College of Electrical and Informational Engineering, Jilin University of Architecture and Technology, Changchun, Jilin, China, in 2018, and the M.S. degree in electrical engineering from the College of Electrical and Computer Science, Jilin Jianzhu University, Changchun, in 2021. He is currently pursuing the Ph.D. degree in electrical engineering with the College

of Instrumentation and Electrical Engineering, Jilin University. His research interests include the uncertainty quantification and optimal design strategy of EV's wireless power transfer systems.

Yu Zhu received the M.S. degree and Ph.D. degree in measuring and testing technologies and instruments from Jilin University, Changchun, Jilin, China, in 2013 and 2021, respectively, where he is an associate professor with the College of Instrumentation and Electrical Engineering. His research interests include the analysis method in electromagnetic compatibility simulation and the uncertainty analysis methods in electromagnetic compatibility simulation.

Yaodan Chi received the B.S. degree in electronic information engineering from the Jilin University of Technology, Changchun, Jilin, China, in 1998, and the master's degree in testing and measuring technology and instruments and the Ph.D. degree in science and technology of instrument from Jilin University, Changchun, Jilin, China, in 2004 and 2018, respectively. She is currently the Vice Director of the Jilin Provincial Key Laboratory of Architectural Electricity and Comprehensive Energy Saving. Her research interests include the uncertainty analysis approaches in electromagnetic compatibility simulation and building equipment intelligent integration technology.